Energetic particle injection events in the Kronian magnetosphere: applications and properties

Inaugural-Dissertation
zur
Erlangung des Doktorgrades
der Mathematisch-Naturwissenschaftlichen Fakultät
der Universität zu Köln
vorgelegt von

Anna Liane Müller
aus Aßlar

Köln 2011

Bibliografische Information der Deutschen Bibliothek

Die Deutsche Nationalbibliothek verzeichnet diese Publikation in der Deutschen Nationalbibliografie; detaillierte bibliografische Daten sind im Internet über `http://dnb.ddb.de` abrufbar.

1. Referent: Prof. Dr. Joachim Saur
2. Referent: Prof. Dr. Bülent Tezkan
3. Referent: Dr. Norbert Krupp

eingereicht am: 10.12.2010

Tag der mündlichen Prüfung (Disputation): 31.01.2011

ISBN 978-3-942171-44-1

uni-edition GmbH 2011
http://www.uni-edition.de

Printed in Germany

At the touch of love everybody becomes a poet. - Plato

Abstract

The Kronian magnetosphere is highly dynamical. The inner part between 3 R_S and 13 R_S contains numerous injections of hot plasma with energies up to a few hundred keV. This thesis concentrates on electron measurements of the Magnetospheric Imaging Instrument (MIMI) onboard the Cassini spacecraft. The azimuthal plasma velocity as well as the injections of charged particles will be characterized. Due to the magnetic drifts, the injected particles at various energies begin to disperse and leave an imprint in the electron as well as in the ion energy spectrograms of the MIMI instrument. The shape of these profiles strongly depends on the azimuthal velocity distribution of the magnetospheric plasma, the age of the injection events as well as the trajectory of Cassini. Considering the known trajectory, the azimuthal velocity of the magnetosphere as well as the ages of individual injections can be characterized. With a least-mean-square fit of the theoretical and observed dispersion profiles, these unknown parameters are obtained. The observation of inverted injection profiles indicates that the magnetosphere subcorotates. This thesis confirms the subcorotation and explains the observations of inverted electron dispersion profiles with a differential velocity profile. The measured flow profile clearly shows that the plasma subcorotates with velocities as low as 80% of full corotation at radial distances between 8 R_S and 13 R_S. With the knowledge of the flow profile and the ages of each injection event, the location where the energetic particles were injected into the inner magnetosphere, are calculated. The night and the morning sector of the magnetosphere are the preferred regions for the generation of hot plasma injections. Furthermore, an analysis of properties of the injections such as the particle pitch angle distribution are performed. The dependencies of intensities and spectral indices of the injection events of spatial parameter are characterized. The intensity of injection events matches with background plasma densities which indicates that the intensity enhancements at $L = 4$ R_S and $L = 9$ R_S are not caused by the internal parameters of the injection events. The intensities show a clear dependency on local time. Injections originating in the noon to midnight sector are less intense than the ones injected on the midnight to noon sector. The low intensity injections are associated with the interchange instability while the high intensity injections might be generated through dipolarization due to magnetic reconnection in the magnetotail of Saturn. These large scale injections were observed with remote sensing. Large scale plasma injections could also be the cause of another subclass of injections, detect with in-situ measurements. Reconsidering the intensity of injections with respect to their age, we infer a lifetime of about 21 hours for injections in the analysed energy range.

Zusammenfassung

Die Magnetosphäre des Planeten Saturn ist hochdynamisch. Der innere Bereich zwischen 3 R_S und 13 R_S ist angefüllt mit Injektionen, bestehend aus hochenergetischem Plasma, mit Energien von bis zu einigen hundert keV. In dieser Arbeit werden dynamische Prozesse der Magnetosphäre sowie Eigenschaften der Teilcheninjektionen untersucht. Dazu werden Elektronendaten des sich auf der Raumsonde Cassini befindlichen Magnetospheric Imaging Instruments (MIMI) ausgewertet. Aufgrund magnetischer und elektrischer Felder beginnen die in die innere Magnetosphäre transportierten elektrischen Teilchen auseinander zu driften. Diese Signaturen sind dann mit Hilfe des Teilchendetektors MIMI als sogenannte "Dispersionsprofile" in Energie-Zeit-Spektrogrammen sichtbar. Im Wesentlichen wird die Form dieser Dispersionsprofile durch den azimutalen Plasmafluss in der Magnetosphäre, das Alter der Teilcheninjektionen sowie der Trajektorie von Cassini bestimmt. Unter Berücksichtigung der bekannten Trajektorie erhält man ein Modell der azimutalen Geschwindigkeit der Magnetosphäre sowie Werte für das Alter der einzelnen Teilcheninjektionen. Mit Hilfe der Methode der kleinsten quadratischen Fehler werden numerisch berechnete mit beobachteten Dipsersionsprofilen verglichen. Das so erhaltene Geschwindigkeitsprofil zeigt deutlich, dass die Magnetosphäre subkorotiert. In einem Abstand von 8 R_S bis 13 R_S rotiert das magnetosphärische Plasma mit gerade einmal 80 % der Korotationsgeschwindigkeit. Kennt man das Geschwindigkeitsprofil sowie das Alter einer individuellen Teilcheninjektion, so kann man dieses zurückverfolgen und somit den Ort bestimmen, an dem das Plasma in die innere Magnetosphäre injiziert wurde. Die Nacht- sowie Morgenseite sind bevorzugte Bereiche für Teilcheninjektionen. Weiterhin wurden Injektionseigenschaften wie die Intensitäten und die spektralen Indizes in Abhängigkeit der Position sowie vom Alter der Teilcheninjekionen untersucht. Die Intensitäten zeigen eine Korrelation mit der Dichte des Hintergrundplasmas. Dies läßt die Schlußfolgerung zu, dass die Intensitätsmaxima der Teilcheninjektionen bei $L = 4$ R_S und $L = 9$ R_S in Zusammenhang mit dem Hintergrundplasma stehen und weniger Eigenschaften der Injektionen selbst sind. Betrachtet man die Intensitäten in Abhängigkeit von der Lokalzeit, so zeigen sich klare Unterschiede in den verschiedenen Sektoren. Die Teilcheninjektionen, die ihren Ursprung im Mittags- bis Mitternachtssektor haben, sind weniger ausgeprägt in ihrer Intensität. Diese Injektionen können in Zusammenhang mit großskaligen Plasmainjektionen, die durch Fernerkundungsinstrumente beobachtet wurden, gebracht werden. Verursacht werden diese Art von Injektionen durch Dipolarisation aufgrund von Rekonnektionsprozessen in der magnetosphärischen Schweifregion. Unter Berücksichtigung der Intensitäten der Injektionen als Funktion ihres Alters folgern wir eine durchschnittliche Lebensdauer von 21 Stunden.

Contents

List of Figures

List of Tables

Preface

Since my childhood, I was fascinated by the Sun, the planets, and all the other objects in our solar system. I loved to see documentations on TV and couldn't even imagine to be a part of such a great project like the Cassini project. Already during my studys and while writing my Diploma thesis, I was provided the opportunity to analyse data of the Magnetospheric Imaging Instrument, a particle detector onboard the Cassini spacecraft. Since 2004, Cassini is orbiting one of the most beautiful objects in the solar system, the planet Saturn. Even though also other planets like Jupiter or Neptune exhibit a ring system, the one of Saturn is the most impressive and really makes Saturn the "Jewel of the Solar System" or "The Lord of the Rings".

The fact that the Earth itself is a magnet is of enormous importance for biological and cultural life. Life on Earth has developed under the protection of its magnetosphere. It protects the atmosphere from being eroded into space and the ground from life damaging radiation, emitted from the sun and other galactic sources.

Already 2000 years ago, the Chinese invented the compass and used it for navigation. Primary in the 11th century, the Arabs brought the compass to Europe. The magnetic and geographical north pole are not identical. But together with a solar compass, information of the time and knowledge that the sun is located in the south at noon, the deviation can be easily estimated. Seamen made these observations over centuries and collected huge data about the Earth's magnetic field.

William Gilbert published his work "De Magnete, Magneticisque Corporibus, et de Magno Magnete Tellure" (On the Magnet and Magnetic Bodies, and on That Great Magnet the Earth) in 1600. *De Magnete* consists of six books and contains, amongst others, description of his experiments with a model of the Earth, called the *terella*. He found out that the Earth itself is a giant magnet. Formerly it was believed that Polaris or a giant magnetic island close to the north pole attracted the compass. Nowadays, geophysical studies together with numerical simulations have supported that the geomagnetic field is generated by a dynamo process inside the Earth. The source of the magnetic field are convection currents in the liquid and conductive core of the Earth.

The Earth's magnetosphere is not just fundamental for life but can also generates beautiful phenomenon like aurorae. During high solar activity, solar wind particles can penetrate the magnetosphere, travel along the magnetic field lines and excite the neutral molecules that emit light when returning to ground state. Oxygen produces green or brownish-red light, nitrogen blue or red light.

The Terrestrial and Kronian magnetospheres show similarities but also differ in many ways. The general shape with its bowshock, magnetopause and stretched magnetotail is comparable. Also the equatorial magnetic field strengths of Earth and Saturn are almost the same (31,000 nT for Earth, 20,000 nT for Saturn). The magnetosphere of Saturn is

thought of also be generated by the dynamo effect, but as in the case for for Jupiter, the generation regions may be near to the surfaces of the planets.
Among the similarities, both magnetospheres show a huge variety of differences. Saturn is a fast rotator (rotation period of 10.4 hours), which makes the centrifugal force a dominant force in the system. Enceladus, with its water geysers in the south polar region, has turned out to be the main neutral and plasma source of the E-ring. Many interesting dynamics are ongoing in this highly variable magnetosphere. Some of these aspects will be adressed in this thesis.
We will use data of the Cassini spacecraft, which is orbiting Saturn since July 2004. The mission is one of the most successful space exploration missions. The nominal part of the mission ended in June 2008, and was continued with the extended mission, called Equinox mission. Saturn was in equinox in August 2009, when the ring plane was aligned with the ecliptic plane and the Sun shined on the rim of the rings. Now we are already in the extended-extended mission, called the Solstice mission. In spring 2010, NASA decided to extend the Cassini mission up to 2017.

1 Introduction

1.1 Saturn - jewel of the solar system

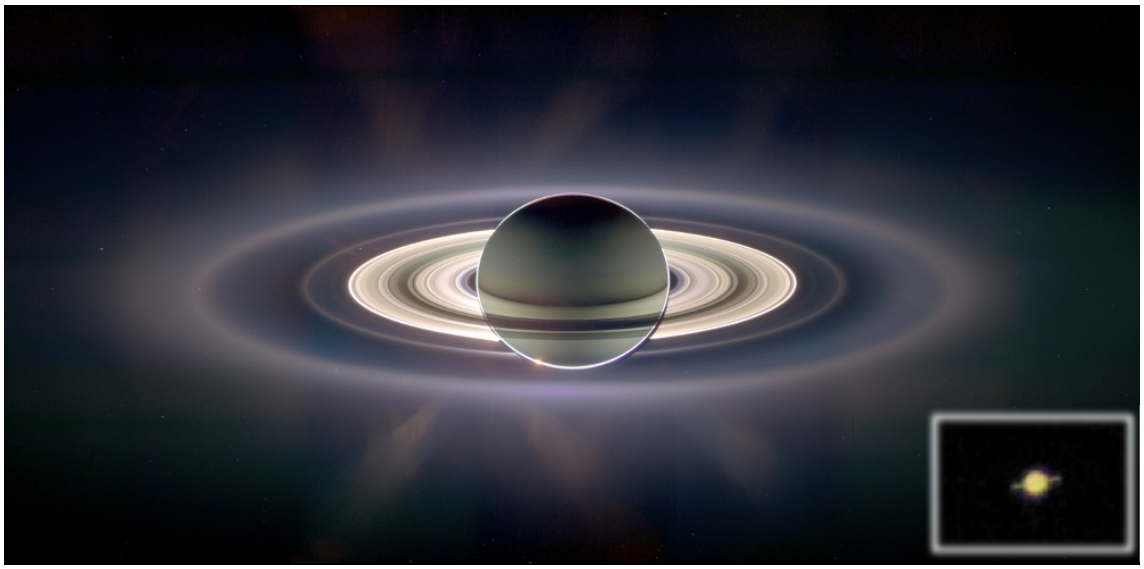

Figure 1.1: Saturn and rings in eclipse. Image was taken with the ISS (Imaging Science Subsystem) camera onboard the Cassini spacecraft on Sept. 15, 2006 and consists out of 165 single images. Image courtesy of NASA/JPL/SSI.
The small picture of Saturn was taken by me and some colleagues with my digital camera on the roof of our institute in Cologne on May 20th, 2010.

1.1.1 Mythology

Nearly all the planets in the solar system are named after Roman or Greek gods. Only the name of the Earth comes from the Indo-European base ‘er’, that became ‘Erde’ in German and ‘Earth’ the English name. The Roman goddess that personified the Earth was Tellus and corresponds to the Greek god Gaia.
In the Roman mythology, Saturn was a major god of agriculture and harvest. The Greek god Kronos is often equalized with Saturn and the mythologies of both gods are commonly mixed.
Kronos was the son of Uranus (Roman: Caelus, god of the sky) and Uranus’ mother Gaia

(Roman: Terra Mater or Tellus, a goddess personifying of the Earth). He was the leader of the Titans, a race of powerful deities, all descendants of Gaia and Uranus.
Other descendants of Uranus and Gaia, three Hecatonchires and three Cyclops, were hid by their own father in Tartaros (Greek: deep place), a place in the underworld that, as a place of punishment, can be considered a hell. Gaia was incensed by this and made a great flint sickle of grey flint (or adamantine). She gathered Kronos and his brothers and asked them to castrate Uranus. Just Kronos agreed and castrated his father. The blood that dropped on Gaia fertilized her so she had further descendants with Uranus.

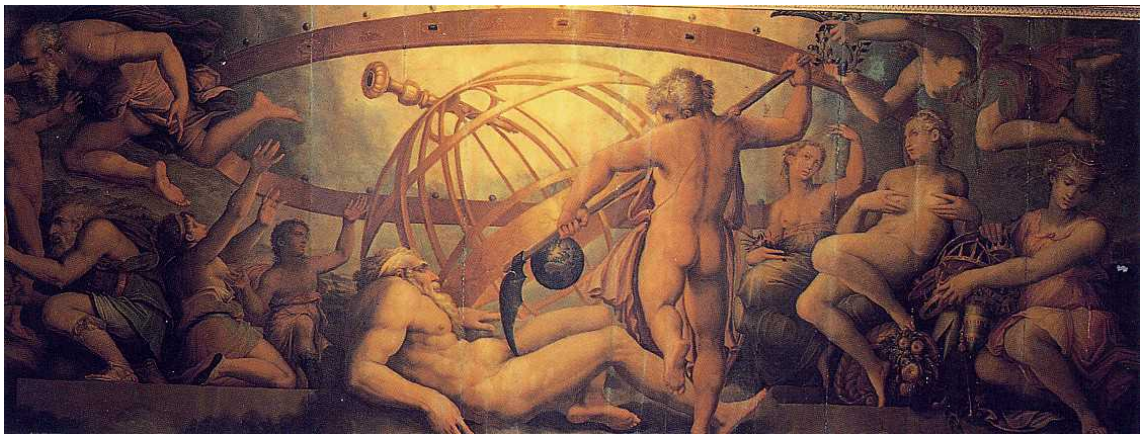

Figure 1.2: Painting by Giorgio Vasari (1511-1574) of the mutiliation of Uranus by Kronos.

Kronos re-imprisoned the Hecatonchires, the Gigantes, and the Cyclopes and together with his sister Rhea, he became the leader of the world and the founder of the Golden Age. Since he was afraid that he could be emasculated by his own progenies, he devoured the gods Demeter, Hera, Hades, Hestia, and Poseidon, to whom Rhea gave birth. Before their sixth child, Zeus, was born, she asked Gaia for advice and gave birth to Zeus secretly in Crete. Instead of his son Zeus, Kronos got a stone wrapped in swaddling clothes (Omphalos Stone). He did not note the swindle and gulped the stone. Therefore Zeus could grew up untroubled. Gaia gave Zeus a poison with which he forced Kronos to spit out the content of his stomach: first the stone and then Zeus' three sisters and two brothers.

1.1.2 History of Saturn's exploration

The history of Saturn's exploration began a long time before the space age. Already the ancients knew about the planet. With the invention of the telescope a totally new era of exploration could begin. In 1610 Galileo Galilei (Italian philosopher, astronomer, physicist and mathematician, 1564-1642) first pointed his telescope at the planet and therefore was the first one who saw the main ring system. He first thought about them as moons, before Christiaan Huygens (Dutch physicist and astronomer, 1629-1695) recognised them as a ring structure around the planet in 1656.

... two companions are no longer two small perfect round globes ... but are at present much larger and no longer round ... that is, two half eclipses with two little dark triangles in the middle of the figures and contiguous to the middle globe of Saturn, which is seen, as always, perfectly round.

(Galileo, 1616)

Already in 1655, Huygens discovered the largest moon of Saturn, Titan. It is the second largest moon in the solar system after Ganymede at Jupiter. Titan is today known as the only moon that pocesses a dense atmosphere. In the years 1671 and 1672 Giovanni Domenico Cassini (French astronomer and mathematician, 1625-1712) discovered the two moons Iapetus and Rhea, followed by Tethys and Dione in 1684. He also discovered the Cassini Division (which was named after him) and therefore gave the first hint that the ring consist of many structures rather than one ring.
With the space age, that begun in October 1957 with the launch of Sputnik, the first Russian artificial satellite, also the in-situ exploration of the planets in the solar system begun. The first spacecraft that visited Saturn was Pioneer 11 in 1979, followed by the two Voyager spacecrafts in 1980 and 1981. It would take more than 20 years before a man-made vehicle got to revisit Saturn. Launched in 1997 and after a seven year travel time, Cassini finally arrived at Saturn in July 2004. Since 6 years it now takes almost continuous measurements in the magnetosphere.

1.1.3 General properties of the planet

Saturn is the second largest planet in our solar system. With an equatorial radius of 60,268 km (= 1 R_S) it is almost ten times bigger than Earth (R_E = 6,378 km) and about 10,000 km smaller than Jupiter (R_J = 71,492 km), the largest planet in the solar system. It orbits the sun in a mean distance of 9.54 AU, with 1 AU being the mean distance between the Sun and the Earth (1 AU = $149.6 \cdot 10^6$ km). One Saturnian day lasts about 10 h 40 min which is almost the same day length as at Jupiter. Therefore Saturn is also called a fast rotator, which has interesting impacts on the magnetospheric dynamics.
With a mean density of 0.69 g cm^{-3}, Saturn is less dense than water (1.0 g cm^{-3}). It possesses a solid rocky (metallic-hydrogen) core, followed by a liquid metallic hydrogen layer, and a gaseous atmosphere (Hubbard et al. 2002) . Since the planet is a gas giant, it does not have a solid surface. The surface is defined as the position where the pressure reaches a value of one bar. The ionosphere affiliates above the atmosphere and connects the planet with the magnetosphere.
Like the other outer planets (Jupiter, Uranus, and Neptune), Saturn possesses a ring system, that is in its characteristics and appearance unique amongst the gas giants. The rings consist mainly of water ice particles. Differences in reflectivity and colours of the rings (Tiscareno et al. 2007) give evidence for further constituents like silicates (Hillier et al. 2007). As a result of sputtering processes, the main rings develop a tenuous neutral gas atmosphere that gets ionized by solar ultraviolet radiation (Waite et al. 2005). This ring ionosphere represents an important source of magnetospheric plasma (Tokar et al. 2005). The Kronian magnetosphere is the third largest magnetosphere (after the Sun's, also known as the Heliosphere, and the Jovian, the largest planetary one) in the solar system.

At the dayside the magnetosphere extends up to the magnetopause, which is approximately at a distance of about 22 R_S. A more detailed description of the global configuration and the dynamics of the magnetosphere will be given in section 1.2.

1.1.4 Moons

Until now, 62 moons were discovered and hence Saturn has almost as many moons as Jupiter. Already in 1655, Titan - the only moon with a dense atmosphere (Baines et al. 2005, Sittler et al. 2006) - was discovered. Until 1847, it was known as the "Huygenian satellite of Saturn". In 1847, John Herschel (English mathematician, astronomer, and chemist, 1792 - 1871) suggested to name the seven known moons after Greek Giants and Titans: Mimas, Enceladus, Titan, Iapetus, Tethys, Dione, and Rhea. Hyperion was discovered one year later, also by direct observation using optical telescopes. The first moon that was discovered by the use of long-exposure photographic plates was the moon Phoebe in 1899. Then, after another 67 years, Janus, the tenth satellite of Saturn was discovered. Janus shares its orbit with Epimetheus, a unique constellation in the solar system. In 1980, the Trojan moons of Dione and Tethys were discovered: Helene, Telesto and Calypso.

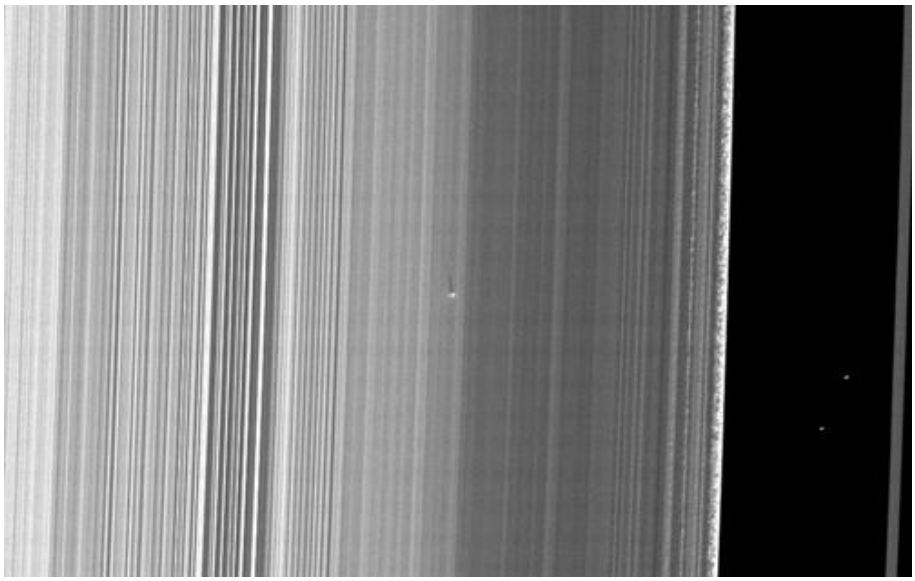

Figure 1.3: Image of the latest discovered moon of Saturn, August 7, 2009. The shadow indicates that it orbits Saturn 200 m above the ring plane.

With the two flybys of the Voyager spacecrafts the number of known moons increased first to 17, and later the 18th moon was discovered in archival images. In the years 2000 - 2007 altogether 37 irregular moons were reported with ground based telescopes.
The first moons that were seen with the Cassini spacecraft were Methone and Pallene at the arrival in year 2004. With ground based telescopes and the Voyager and Cassini spacecrafts alltogether 62 moons of Saturn were discovered, with the last discovery being a moonlet inside the B-Ring on August 7, 2009 (see Fig. 1.3).

1.2 Magnetosphere of Saturn

Saturn has, like the Earth, an intrinsic magnetic field. This magnetic field is more or less dipolar, at least near the planet. The solar wind impinges on and interacts with this field. The magnetic field gets deformed and solar wind driven dynamical processes can take place, see Fig. 1.4 for an artistic overview of the magnetosphere. Due to the relatively high rotation rate of Saturn, its unique ring system and numerous moons, a lot of interactions between plasma, neutrals, dust, ring particles, and moon surfaces can be observed. The ring system as well as the moons orbiting Saturn inside the magnetosphere can act as plasma sources as well as plasma sinks. Enceladus was identified as the main plasma source. It plays therefore the same role as Io does in the Jovian system. About 100 kg sec^{-1} of plasma are injected into the magnetosphere of Saturn (Pontius and Hill 2006), which is still one order of magnitude less than at Io (Saur et al. 2004, and references therein). The icy satellites absorb plasma that can be detected as absorption signatures in energetic plasma measurements (Roussos et al. 2007).
Since Enceladus represents an important neutral and plasma source, it is responsible for the global magnetodisk configuration. Newely created plasma is accelerated to corotation velocity. Due to the centrifugal force the plasma is driven radially outward and stretches the magnetic field lines, modifying the dipolar field at large distances to a magnetodisc configuration (Arridge et al. 2007).

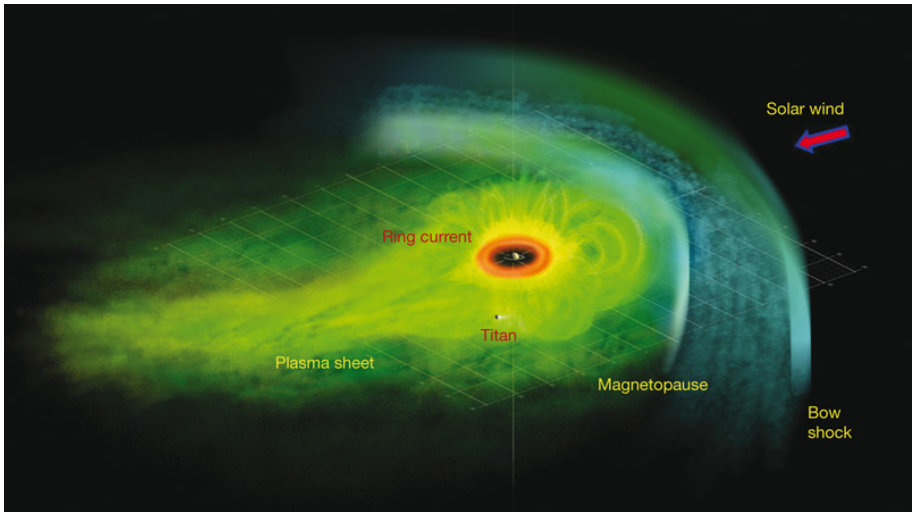

Figure 1.4: Artistic view of the Saturnian magnetosphere Krimigis et al. (2007). Saturn is in the center, surrounded by the red doughnut shaped neutral gas cloud, located outside of the main ring system. This population of neutrals is followed by a ring current than thins towards the night side. The solar wind impinges from the right hand side on the magnetosphere and is slowered to sub-sonic velocities at the bow shock. The magnetopause marks the region where the magnetic pressure of the solar wind is equal to the magnetic pressure of the Saturnian magnetosphere.

Unlike every other planet in the solar system, the magnetic axis and rotational axis of the planet differ by less than 0.5 degree (Gombosi et al. 2009). In addition, the higher order

terms of the internal field show a highly symmetric field. Cowling's theorem says that an asymmetric field can not be maintained by a purely dynamo process. Stanley (2010) have shown that the symmetry of the Saturnian magnetic field could be explained by a stably stratified layer. Thermal winds within this layer are able to shear out the non-axisymmetric components of the magnetic field. They have also demonstrated with their numerical model that the 'Saturn-like' boundary conditions (cold poles and hot equator) are the only ones that produce axisymmetric fields.

1.2.1 Plasma sources

Even though Enceladus is a relatively small satellite with a diameter of about 500 km (for comparison the moon of the Earth has a diameter of 3,476 km, and Titan has a diameter of 5,150 km), it obviously hides a big secret beneath it's surface. The moon exhibits, with a value of almost 1, the highest albedo in the solar system. Since the albedo of a body is related to its surface age, this value implies that the surface of Enceladus is remarkably young. Additionally, it was found out by Baum et al. (1981) with ground-based observations, that the E-Ring exhibits its highest density at the orbit of Enceladus. These two facts lead to the hypothesis that Enceladus is a geologically active body that continuously renews its surface. It is the main source of the micron-sized E-Ring particles, the gas of the neutral torus as well as the main plasma source in the magnetosphere. Cassini finally disclosed Enceladus' hidden secret. First hints of an atmosphere that modified the magnetic field of Saturn were given by Dougherty et al. (2006).

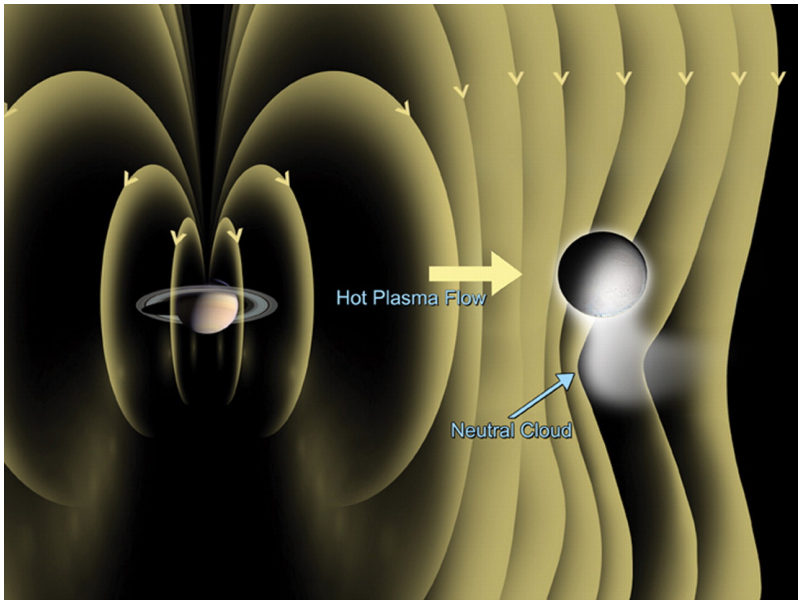

Figure 1.5: Sketch of the interaction of Enceladus' neutral environment with the magnetosphere of Saturn (Dougherty et al. 2006).

Fig. 1.5 shows the interaction principle between the neutral gas cloud and the magnetic field, which is able to explain the measured magnetometer data. The plume at the south pole of the moon acts as an additional barrier to the plasma flow. The magnetic field lines

are then deformed in the vicinity of the region south of Enceladus. Due to this finding, distances of the original Enceladus' flybys were lowered in order to investigate the south polar region in more detail.
Fig. 1.6 shows the first observations of south polar region of Enceladus (a) and the plumes (b) that emit neutral water group molecules into the magnetosphere (Spencer et al. 2006, Porco et al. 2006). Clear streams of water can be identified in the picture. Due to charge-exchange processes of the neutrals with the magnetospheric ions, momentum is loaded to the magnetosphere (Pontius and Hill 2009). Cassidy and Johnson (2010) investigated in more detail how the plumes of Enceladus can populate the large extent of the neutral torus. Neutral-neutral interaction and plasma-neutral interaction can produce the observed cloud morphology.

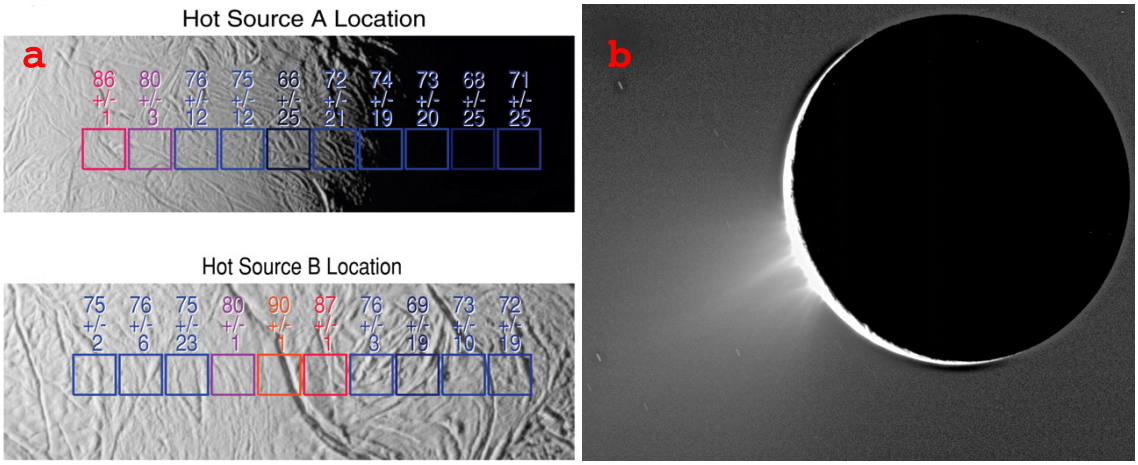

Figure 1.6: South polar region of Enceladus. Panel (a) shows the surface of the tiger stripes region with measured temperatures in Kelvin (Spencer et al. 2006). Panel (b) shows the near surface plumes (Porco et al. 2006).

The eruptions of water ice molecules seem to be periodically. Due to tidal shear stress the large rifts, called the 'tiger stripes' due to similarity in outlook, open and close periodically and so varies the eruptions (Hurford et al. 2007). Saur et al. (2008) have modelled the plasma interaction of Enceladus and compared their two-fluid model results with the observations of magnetometer data and neutral density measurements in the vicinity of the moon. To explain the data of the four Enceladus' flybys, that were available at that time, the plume activity has to be assumed to be time variable. The north-south asymmetry of the eruption geometry implies interesting interaction with respect to the magnetospheric current systems. The plume region produces surface currents that couple the northern with the southern hemisphere (Saur et al. 2007).

1.2.2 Dynamics of the magnetosphere

In the past, it was believed that there could exist two types of magnetospheres: solar wind dominated and internally controlled. The prime example of the former one is the Terrestrial magnetosphere. Earth is a slow rotator, the equatorial surface magnetic field is about 31,000 nT, and about 1 kg s^{-1} of ionospheric plasma is produced. In the resulting

Dungey cycle plasma is transported from the dayside via reconnection along the poles towards the nightside. In the magnetotail, another reconnection process can occur, so that an X-line is formed. At both sides of the X the plasma is accelerated. One part is released as a plasmoid through the magnetotail whereas the earth-directed part contracts back towards the planet. In the Dungey circle the plasma convection is controlled by magnetic reconnection of the planet's magnetosphere with the interplanetary magnetic field (IMF) (Dougherty et al. 2009).

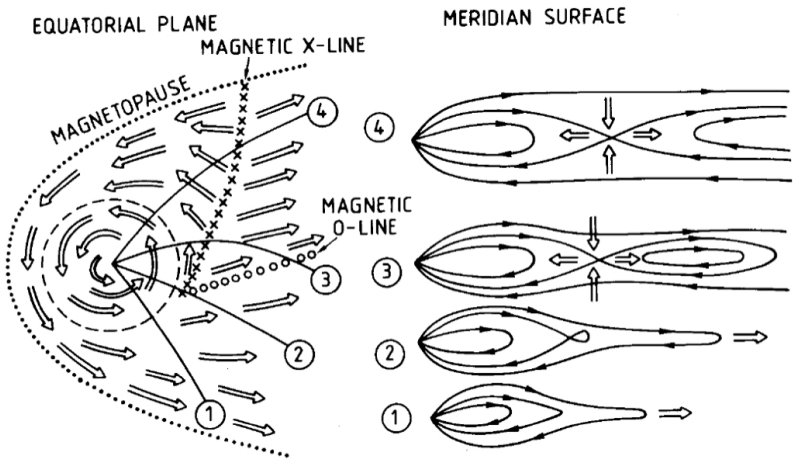

Figure 1.7: Sketch of the Vasyliunas cycle (Dessler 1983) for the Jovian magnetosphere.

The prime example for an internally controlled magnetosphere is the Jovian magnetosphere. Jupiter is a fast rotator (9.9 h) and the equatorial surface magnetic field is about 420,000 nT. Io, the main plasma source inside the magnetosphere, produces approximately 10^3 kg s^{-1} of plasma. The Vasyliunas cycle is a plasma convection cycle that is controlled by mass-loaded field lines that stretch out in the magnetotail and are then eventually released tailwards. Fig. 1.7 sketches the Vasyliunas cycle for the Jovian system. Reconnection and plasmoid release looks very similar in the Terrestrial magnetosphere, even though the generation process is different. The meridian surface cut sketch on the right hand side of Fig 1.7 shows from (1) to (4) the plasmoid formation and release. First the magnetic field lines are stretched due to plasma adding (1) and magnetic field line reconnect in the magnetotail and a plasmoid is formed (3). This plasmoid is then released through the magnetotail whereas the other side of the X-line snap back planetwards (4).
In the case of Saturn, both convection cycles do play an important role. In contrast to the Dungey cycle at Earth, the centrifugal force is one of the most dominant forces. Therefore, also the Vasyliunas cycle is pronounced in the magnetosphere of Saturn. In general, the magnetosphere can be divided into three distinct parts in which different plasma flow patterns control the dynamics (Cowley and Bunce 2003). The inner region is dominated by the planet's rotation and the newly produced plasma corotates. In Fig. 1.8 this region is marked with closed flow lines that stretch more to the nightside due to the compressed

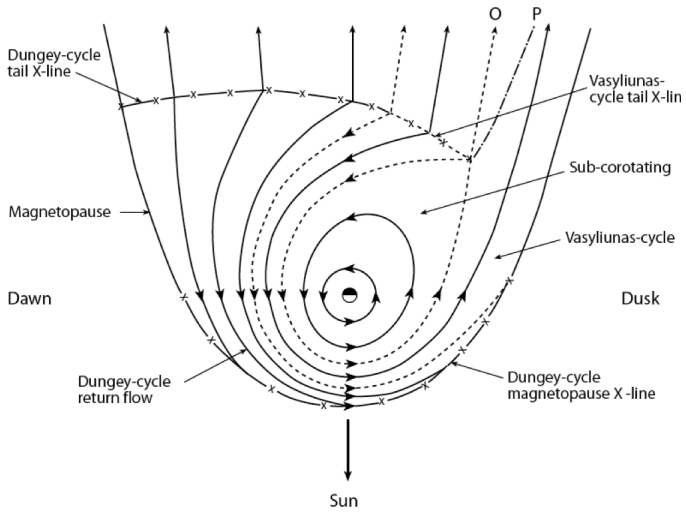

Figure 1.8: Sketch of the plasma flow cycles in the Kronian magnetosphere (Cowley and Bunce 2003).

field lines on the dayside. The region beyond rigid corotation is characterized with sub-corotating plasma and radial outflow down the dusk flank magnetotail. Jackman et al. (2007) reported on three plasmoid releases through the magnetotail, identified by typical changes in the components of the magnetic field, like strong rapid dipolarizations with north- and southward turnings. Another generation possibility of these plasmoids was postulated by Russell et al. (2008). The authors have shown that at the time of plasmoid release, Titan was located at midnight local time. That suggested the possibility of Titan being the trigger for plasmoid release through the magnetotail.
The third and outermost region in Fig. 1.8 goes along with the Dungey cycle. The reconnection region is relatively broad at the dayside magnetopause. The plasma is transported across the poles towards the tail X-line from where closed field lines return sunward to complete the cycle (Cowley and Bunce 2003).

	Earth	Saturn	Jupiter
Heliocentric distance [AU]	1	9.5	5.2
Equatorial radius [km]	6,371 (R_E)	60,268 (R_S)	71,492 (R_J)
Magnetic moment $\left[\mathrm{T\ m^{-3}}\right]$	$7.75 \cdot 10^{15}$	$4.6 \cdot 10^{18}$	$1.55 \cdot 10^{20}$
Equatorial magnetic field [nT]	31,000	20,000	420,000
Dipole tilt [°]	10.5	0.5	10
Dayside magnetopause distance	~10 R_E	~22 R_S	~50 R_J
Magnetospheric plasma source $\left[\mathrm{kg\ s^{-1}}\right]$	~1	~300	$\sim 10^3$
Equatorial rotation period [h]	23.934	10.53	9.925

Table 1.1: Magnetospheric and physical parameters of Earth, Saturn, and Jupiter (Gombosi et al. 2009).

1.2.3 Electron distributions

The magnetosphere can be divided in different parts in many ways. One is to characterize plasma parameter and define boundaries, where these parameter change. Schippers et al. (2008) have defined three different plasma regions with boundaries at 9 R_S and 14 R_S. In the inner region up to 9 R_S the density of the suprathermal plasma with energies from 0.1 keV to 10 keV increases about one magnitude and reaches a maximum at 9 R_S. The plasma beta also increases and reaches a value around one and stays constant for higher radial distances. This behaviour is also shown by Sergis et al. (2007), where the authors identified the region between $L = 8$ R_S and $L = 14$ R_S as the one with a high plasma beta β of values near 1. For higher L-shells than 15 R_S, the plasma beta seems to be quite scattered around 1. Paranicas et al. (2010) analysed the transport of energetic electrons into the inner magnetosphere of Saturn and showed that the intensity of electrons with energies from 41 keV to 60 keV exhibit a clear peak between 7 R_S and 9 R_S. In this region also a local time asymmetry is visible in Fig 1.9. On the nightside, the intensities are one to two magnitudes higher than on the dayside. This asymmetry is also revealed in Carbary et al. (2009). The authors analysed the energy ranges from 110 keV to 395 keV and from 220 kev to 485 keV separately. In the lower energy range their distribution looks almost the same as in Paranicas et al. (2010). The intensities show a maximum between 6 R_S and 10 R_S, the orbits of Dione and Rhea, respectively. In addition to this, a second maximum is visible between 2 R_S and 4 R_S with the same LT asymmetry.

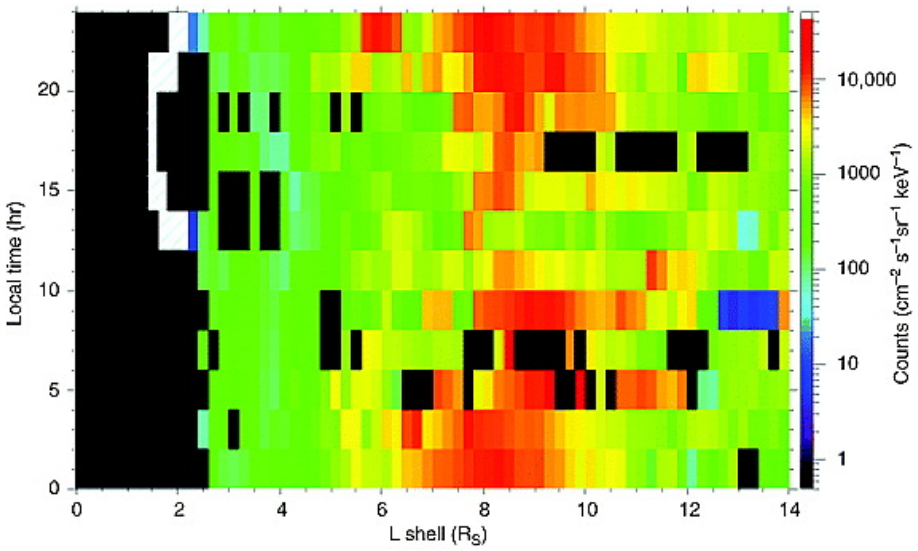

Figure 1.9: Differential intensities of electrons with energies from 41 keV to 60 keV with equatorial pitch angles between 50° and 130° obtained by Paranicas et al. (2010). LEMMS data between mid 2004 and 2010 are averaged and binned by L-shell and local time.

This behaviour is similar for thermal energies. As shown in Fig. 1.10, the electron density increases also towards the planet of about one magnitude and reaches a maximum near the orbit of Enceladus. Also the ion source rate reaches a maximum at $L = 4$ R_S, as shown by Smith et al. (2010) due to the cryovolcanism on Enceladus. The pick-up ion source

rate is about 4 magnitudes higher at Enceladus than at a distance of 6 R_S. Krimigis et al. (2007) have analysed the ring current at Saturn and found the inner boundary of the ring current to be at about the orbit of Rhea (8.74 R_S). Between the orbits of Rhea and Titan (20.2 R_S) there exist an enhanced flux of ENAs, which is not symmetric in local time.

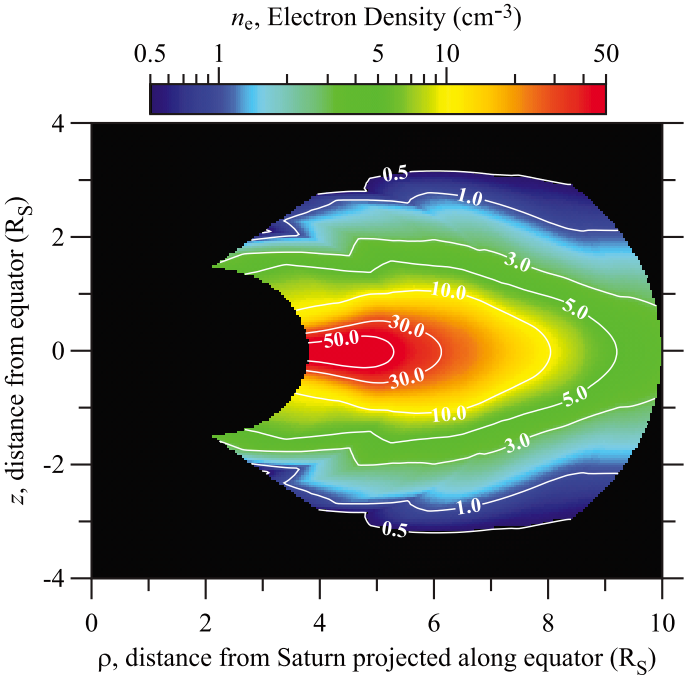

Figure 1.10: Model of electron densities obtained by Persoon et al. (2009) by a comparison of the diffusive equilibrium model and measured densities from the Cassini Radio and Plasma Wave Science (RPWS) instrument.

1.3 Injection events

Injection events have been observed in the Kronian magnetosphere between 3 < L < 13 R_S and were reported by several authors (e.g. Burch et al. (2005), Mauk et al. (2005), Hill et al. (2005), Chen and Hill (2008), Rymer et al. (2008), Müller et al. (2010), Paranicas et al. (2010)). Before they were reported at Saturn, they have been observed in the Earth' magnetosphere (Deforest and McIlwain 1971) and later at Jupiter (Mauk et al. 1999).

1.3.1 Injections at Earth

The Terrestrial magnetosphere is always reported as a prototype of an externally driven magnetosphere (Kivelson and Russell 1995). The primary phenomenon that drives geomagnetic activity is the magnetospheric substorm. Already Akasofu (1964) described the substorm phenomenon in the magnetosphere of Earth. The energy transport from the solar wind through the magnetosphere into the atmosphere is visible in dynamical changes

in the auroral oval. The plasma transport is governed by the Dungey cycle.
During southward configuration of the interplanetary magnetic field, reconnection can take place at the dayside of the magnetosphere. That means, solar magnetic field lines merge with Terrestrial field lines and plasma, originating from the Sun, can enter the Earth's magnetosphere. This plasma is then transported tailwards and energy is released in the magnetotail.
The *substorm* can be divided into three different phases:

- growth phase,
- expansion phase, and
- recovery phase.

Fig. 1.11 illustrates the different phases. During the *growth phase* the reconnection rate at the dayside is enhanced due to a southward oriented IMF. The flux is transported into the magnetotail and partly convected back to the dayside. The magnetic flux that is not convected is stored in the magnetotail. The growth of the tail lobe magnetic field is associated with a growing neutral sheet current that stretches the magnetic field lines to a more tail-like configuration (see upper panel of Fig. 1.11).

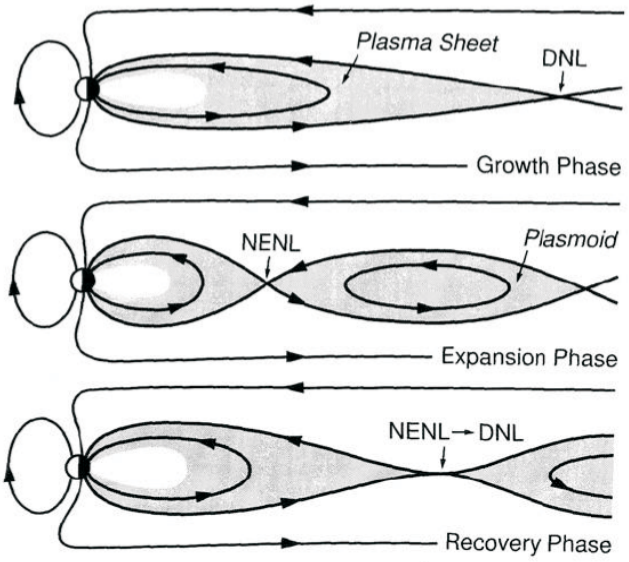

Figure 1.11: Sketch of the magnetotail evolution during a substorm, where DNL is the distant neutral line, and NENL being the near earth neutral line (Baumjohann and Treumann 1996).

Reconnection at the nightside is associated at distances of about a few hundreds R_E, called the *distant neutral line* (DNL). After about the typical time scale of one hour the magnetotail becomes unstable. During the *expansion phase* reconnection occurs at a distance of about 30 R_E, named the *near-Earth neutral line* (NENL), and the magnetic field becomes

more dipolar (see left hand side of the middle panel of Fig. 1.11). Between the two reconnection points a magnetic bubble with plasma inside is formed, called a *plasmoid*. The time period for the expansion phase is typically 30 - 60 minutes.
The *substorm recovery phase* lasts for about 1 - 2 hours and is characterized with a 'normalization' of the magnetic field configuration and energy release. The near-Earth stretched magnetic field lines dipolarise and move rapidly towards the planet. Plasma is transported into the inner magnetosphere and becomes adiabatically heated. This plasma convection is associated with *energetic particle injection events*. The plasmoid is transported tailwards and is lost again to the solar wind (see lower panel of Fig. 1.11).

1.3.2 Injections at Jupiter

Jovian injection events have been reported by Mauk et al. (1997, 1999) in the energy range above 20 keV and at radial distances between 9 and 27 R_J. Measurements were made by the Energetic Charged Particles Detector (EPD) onboard the Galileo spacecraft. The reported injections show similar characteristics to the 'substorm' events at Earth, even though the Jovian magnetosphere is believed to be the opposite prototype than the Terrestrial magnetosphere. Jupiter is a fast rotator and the main internal plasma source is very strong. Dynamical processes like the injection events are therefore thought to be caused due to the fast rotation of the planet and the gradient of plasma content rather than the solar wind. The so-called 'interchange instability' can cause the exchange of magnetic flux tubes from the inner magnetosphere with flux tubes originating in the outer magnetosphere (Southwood and Kivelson 1987). Io populates the magnetic flux tubes with plasma. These flux tubes become unstable due to the centrifugal force and can move radially outward. To compensate the outflow motion, a flux tube originating in the outer magnetosphere, moves radially inward. This motion is equatable to injection events. These injections of energetic particles are observable in energy-time spectrograms as dispersed features. The plasma is transported from outer parts of the magnetosphere planetwards, where the magnetic field gets more intense. The energetic particles are adiabatically heated, therefore they represent a subpopulation of high energetic particles within a colder background plasma. The particles are detected by a particle instrument in the following sequence

1. high energetic ions,
2. low energetic ions,
3. low energetic electrons, and
4. high energetic electrons.

In section 2.5 we will explain the processes that cause the particles to be measured in this order. This dispersion is independent of the generation process, e.g. interchange or substorm events. Fig. 1.12 shows measurements of EPD illustrated as an energy-time-spectrogram. The black lines show the dispersion in that sense that the low energetic electrons were detected prior to the high energetic ones.

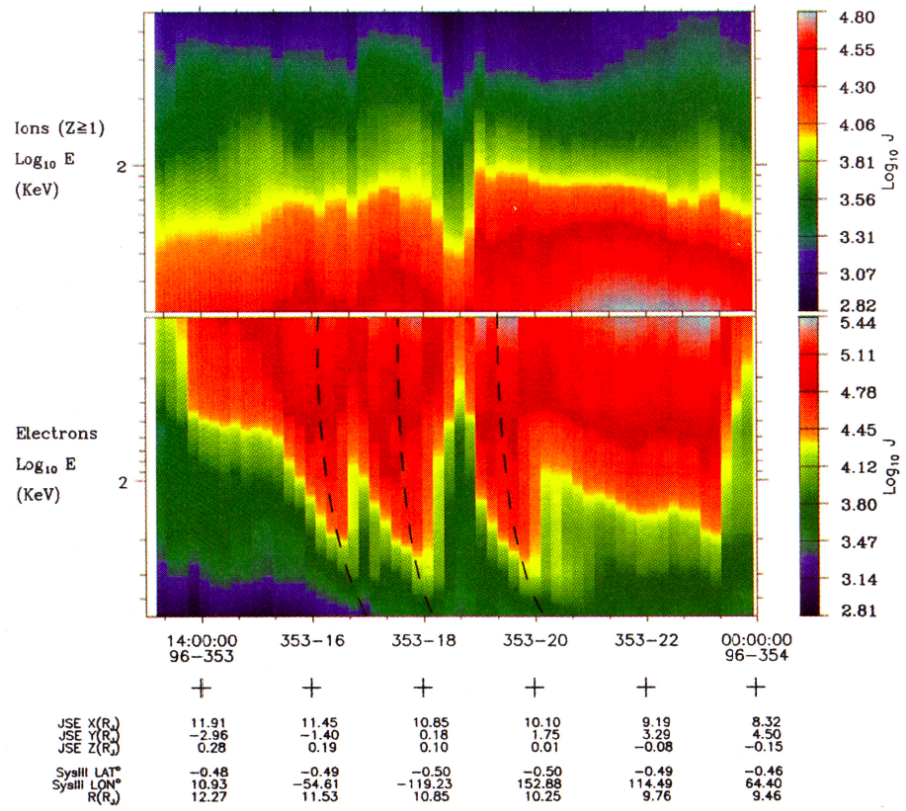

Figure 1.12: Energy-time-spectrograms for ions (upper panel) and electrons (lower panel) (Mauk et al. 1999). The black lines are hand-drawn to clarify the dispersed nature of the injections.

1.3.3 Injections at Saturn

Injection events are observable in the magnetosphere of Saturn between 3 and 13 R_S. It is still an ongoing discussion whether the injection events are generated by substorm-like events as in the Terrestrial magnetosphere or caused by the centrifugal interchange instability as at Jupiter. The decrease of flux tube content with increasing distance to the planet, that is fundamental for the centrifugal interchange instability, has been observed by Sittler et al. (2008) for $L > 6$ R_S. With the Cassini spacecraft taking continuous measurements of the energetic particle distribution, we have the ultimate tool to better understand the origin, generation, and importance of energetic particle injection events in the Kronian magnetosphere.

Injections in the Kronian magnetosphere have been reported by numerous authors (e.g. Mauk et al. (2005), Paranicas et al. (2007, 2010), Müller et al. (2010)) that used the Low Energy Magnetosphere Measurement System (LEMMS) of MIMI. Since we will use data of this detector, we will give a detailed description of the instrument in section 3.2.1. Also the Ion and Neutral Camera (INCA) detected the injections at Saturn through remote sensing, as shown by Mitchell et al. (2005, 2009). Injections cause an increase of energetic particles at a given distance. If this increase occurs at regions where neutral gas

is present like in the neutral gas cloud, the energetic ions will undergo charge exchange, creating energetic neutral atoms (ENAs) that can be detected by INCA. These ENA emissions show the precence of energetic particles which have been injected on the nightside of the magnetosphere, see Fig. 1.13. Since they are very extended in radial distance and local time, it is still an ongoing discussion if these emissions features in the remote sensing data are even identical to the in-situ injection events we are studying in this thesis. In section 5.2.1 we will show evidence that both injections are somehow related.

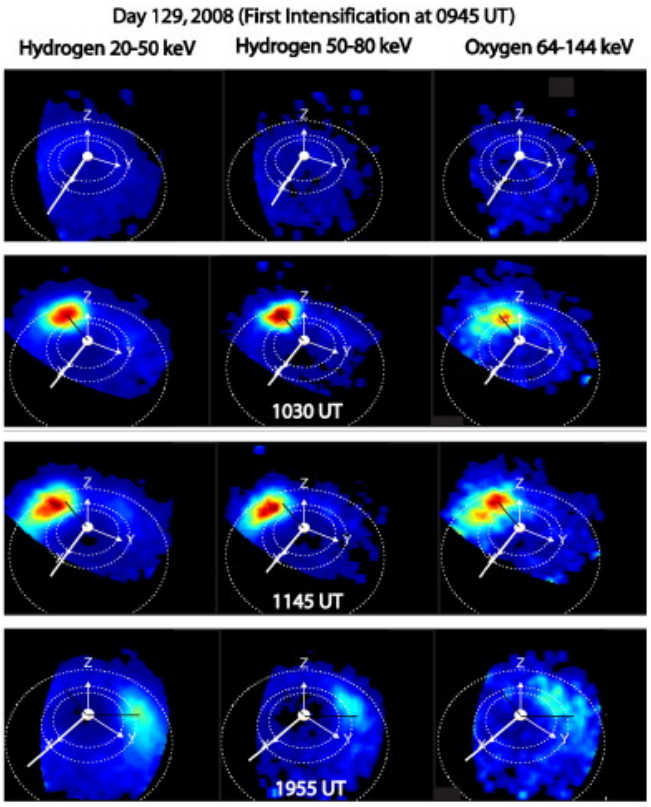

Figure 1.13: ENA emissions of a large-scale injection (Mitchell et al. 2009). The direction to the Sun is indicated by the heavy white line, the arrowed white line points to dusk. From top panel to bottom panel the evolution of an injection event is displayed for different ion species and energies.

The signatures of the injection events have not just been seen by detectors of MIMI but also with the Cassini Plasma Spectrometer (CAPS), that measures the energetic particle population in a lower energy range than MIMI. Burch et al. (2005), Hill et al. (2005), Chen and Hill (2008) reported on these events and have analysed their ages, local time distribution, longitude distribution and periodicities.
In this thesis we concentrate on electron injection events in the Kronian magnetosphere as measured by the MIMI/LEMMS instrument. Even though in some cases electron features appear paired with ion features, the dispersion features of ions are much less visible in the data since the ion lifetimes are of the order of just a few hours (Mauk et al. 2005, Dialynas et al. 2009).

1.3.3.1 Pitch angle distribution of injections

To determine the source location of injections, Rymer et al. (2008) performed simulations of adiabatic radial plasma transport under the assumption of first and second adiabatic invariant conservation. In section 2.3 we describe in detail the concept of pitch angle distributions (PADs) as well as their cause. Rymer et al. (2008) characterized the change in PAD for injections in the energy range of 1 eV to 13 keV and compared their results with measurements of CAPS. Fig. 1.14 shows an energy-time spectrogram of a recent injection on 2005/303. The authors detected three different pitch angle distributions in the high energy CAPS from some keV to 10 keV. Inside the injection the distribution clearly shows a *pancake* distribution with a peak intensity at 90° pitch angle for electrons of 12.9 to 15.0 keV. For electrons just before and after the injection in the energy range of 2.2 to 2.7 keV the distribution shows a *butterfly* distribution with intensity peaks at about 60° and 120°. In the lower energy range from 24.1 to 28.24 eV and 405.0 to 473 eV the distribution is *field aligned* with intensity peaks at 0° and 180°. The pancake distribution can be achieved if energetic particles with an isotropic distribution at large radial distances are adiabatically transported to low L-shells. The butterfly distribution can just be obtained if also non-adiabatic processes are acting on the plasma population. The authors conclude from the field-aligned distribution that 'these low energetic electrons are the signature of the flux tube interchange connection to the ionosphere'.

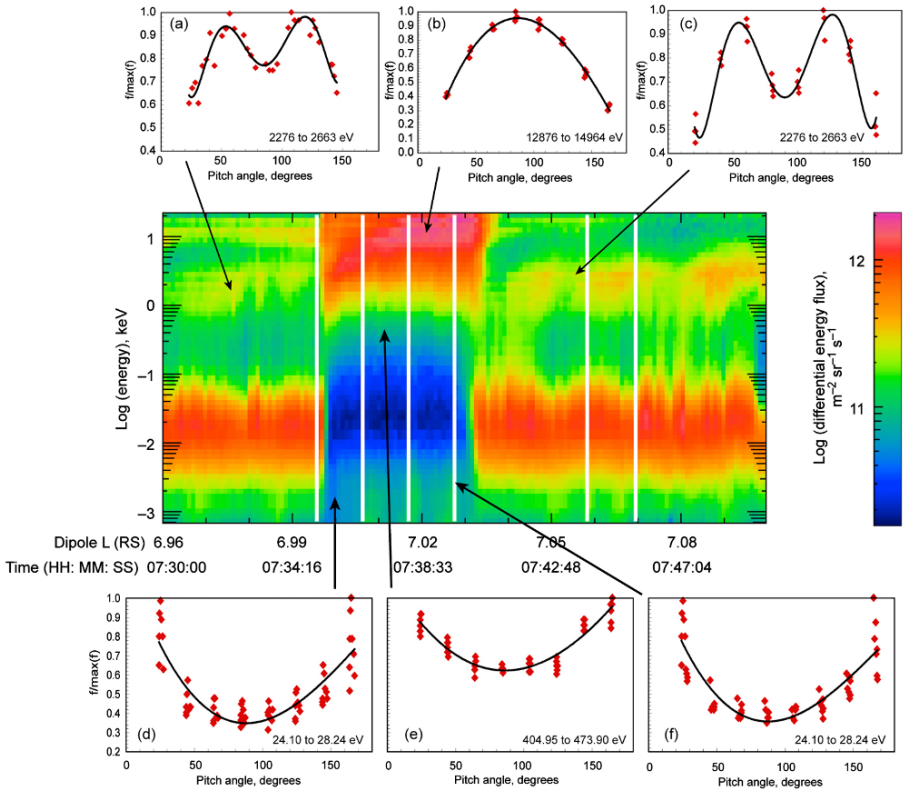

Figure 1.14: Energy-time spectrogram and pitch angle distributions of a recent injection event on day 2005/303 for differnet energies (Rymer et al. 2008).

1.3.3.2 Inverted dispersion profiles

In contrast to the injection events at Jupiter, the injections at Saturn show inverted dispersion profiles on most of the outbound part of the spacecraft trajectories. That means, the electrons are detected in an inverse order: high energetic electrons prior to the low energetic ones (see Fig. 1.15). At first, there was no explanation for the occurrence of these inverted electron injections, mainly they have not been observed in the magnetosphere of Jupiter. Due to the fact that the inverted profiles are just detected on the outbound path of the spacecraft trajectory, it is obvious that the occurrence is somehow related to the spacecraft motion. Mauk et al. (2005) explained the inverted dispersion profiles with a differential plasma velocity profile with decreasing angular velocity with increasing radial distance. Due to the motion of charged particles based on magnetic drifts and due to the positive radial velocity of the spacecraft, it is possible to observe these kinds of dispersion profiles. In section 4.1 we will give a detailed description of these mechanisms and show simulations of particle motion in the magnetic field of Saturn.

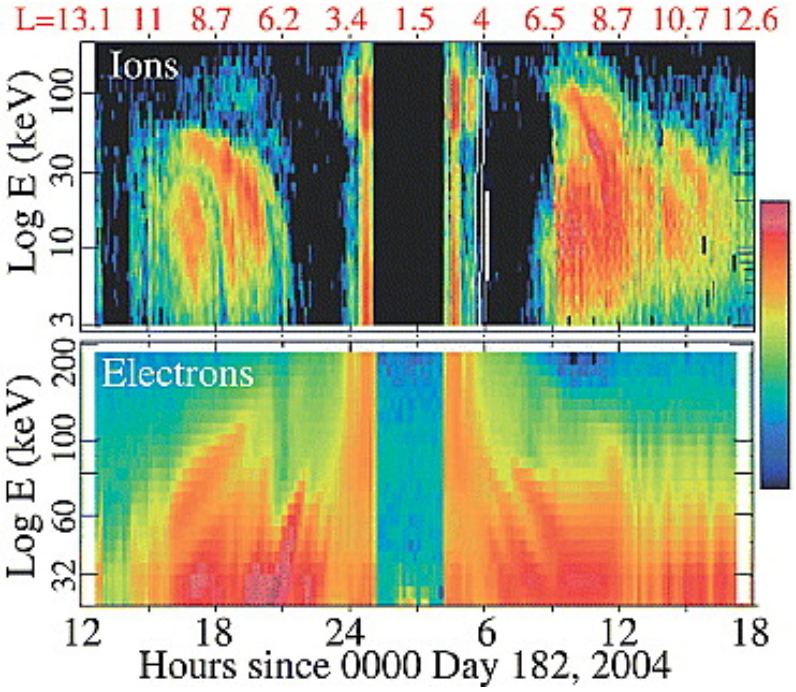

Figure 1.15: Energy-time-spectrogram of Saturn Orbit Insertion (SOI) ion (upper panel) and electron data (lower panel) (Mauk et al. 2005). Clear signatures of injections are visible around closest approach. 'Normal' injections are observable on the inbound path of the trajectory (see *L*-shell of the spacecraft at the top). 'Inverted' dipsersion profiles are clearly visible at the outbound path between hours 6 and 12 of day 183.

2 Theoretical background

2.1 Space plasmas

Approximately 99 % of the visible mass in the universe is in the plasma state. This is also known as the fourth state of matter. A plasma can be partly or fully ionised. In nature there exist a huge variety of plasmas (see Fig. 2.1).

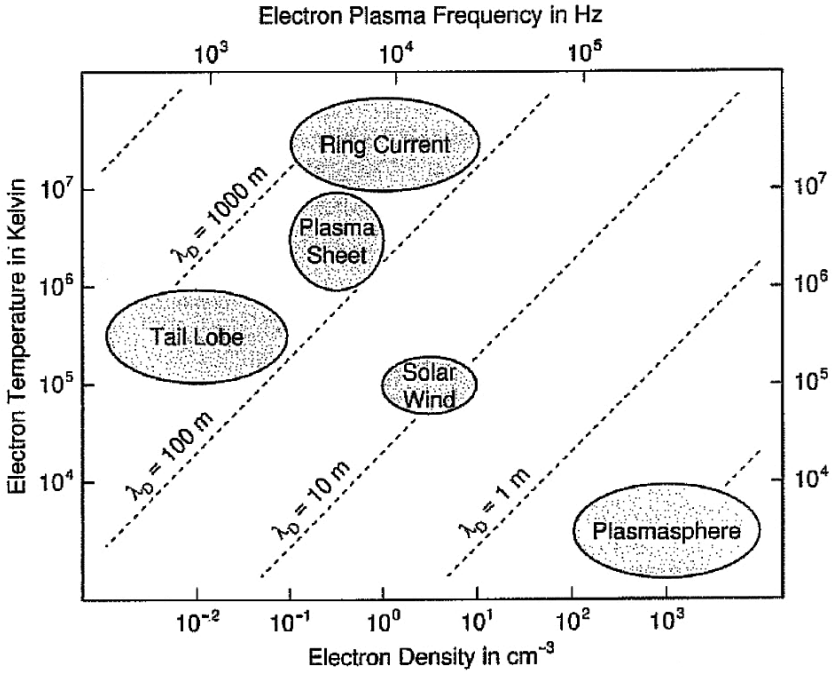

Figure 2.1: Temperature and density of various geophysical plasmas (Baumjohann and Treumann 1996) with λ_D being the Debye length, see (2.1) for definition.

Additionally to the pressure, mass density and temperature, which are the three independent parameters that can be used to describe ordinary material, the description of plasma requires more parameters such as

- number density,
- Debye length, and
- plasma frequency.

For each species the number density has to be defined. If we assume singly charged particles, the number densities for electrons and ions must be roughly the same to fulfil the condition of quasi neutrality. The Debye length λ is one of the most important quantities to describe a plasma. In Gurnett and Bhattacharjee (2005) a simple and practical equation is given by

$$\lambda_D[cm] = 6.9\sqrt{\frac{T_e}{n_0}} \tag{2.1}$$

where T_e is the electron temperature in Kelvin and n_0 the number density in cm^{-3}. The Debye length λ_D is the distance over which the plasma can maintain the charge neutrality. The definition of a plasma implies that the deviation of charge neutrality is very small.

2.2 Single particle motion

There are different ways to describe a plasma:

- single particle approach,
- magnetohydrodynamics (MHD),
- multi-fluid approach,
- kinetic theory, and
- hybrid approach.

Each of these methods has got advantages and disadvantages. Their application strongly depend on the scientific problem of interest.
To fully describe a plasma, it is necessary to take into account the motion of single particles, their collective behaviour, the electric and magnetic fields generated by their distribution and motion, and in turn the influence of the fields on the distribution and motion of the particles.
The first step to describe a plasma is to concentrate on the motion of a *single particle* inside a magnetic or electric field and neglect the fields that are produced by the motion of this single particle. If external fields are strong and the plasma is tenuous, then the generated fields by particle motions are weak and can be neglected (Gurnett and Bhattacharjee 2005). This is the case for the energetic particles discussed in this thesis.
In *MHD*, all single particle motions are neglected and the plasma is treated as a fluid with macroscopic variables such as average density, average velocity, and average temperature.
In the *multi-fluid approach*, the plasma is not just assumed as one fluid but accounts for different species as electrons, protons or even heavier ions. Each of them is treated as a separate fluid.
Since a plasma consists out of a large number of individual particles, their behaviour can be described using a statistical approach. In the *kinetic theory*, the plasma of interest is described by distribution functions in physical and velocity space. The system of equations is known as the *moment equations*, with the most commonly used averages as number density, average velocity, kinetic energy density, and the pressure tensor.

There also exist mixture approaches to describe a plasma. In the *hybrid approach*, the electrons are treated as a fluid whereas the ions are treated as single particles.

2.2.1 Gyration

In contrast to neutral matter such as gases, fluids or dust, the motion of charged particles is determined by electric and magnetic fields. A particle with charge q within an electric field **E** and a magnetic field **B** experiences the *Lorentz force*

$$\mathbf{F}_L = q\,(\mathbf{v} \times \mathbf{B}) \tag{2.2}$$

as well as the *Coulomb force*

$$\mathbf{F}_C = q\mathbf{E} \tag{2.3}$$

These two forces lead to the equation of motion for the non-relativistic case, that can be written as

$$m\frac{\mathrm{d}\mathbf{v}}{\mathrm{d}t} = q\,(\mathbf{E} + \mathbf{v} \times \mathbf{B}) \tag{2.4}$$

with m being the rest mass of the particle. In the absence of an electric field ($\mathbf{E} = 0$), this equation reduces to

$$m\frac{\mathrm{d}\mathbf{v}}{\mathrm{d}t} = q\,(\mathbf{v} \times \mathbf{B}) \tag{2.5}$$

Taking the dot product with **v** and the vector relation $\mathbf{v} \cdot (\mathbf{v} \times \mathbf{B}) = 0$, we obtain

$$m\frac{\mathrm{d}\mathbf{v}}{\mathrm{d}t} \cdot \mathbf{v} = \frac{\mathrm{d}}{\mathrm{d}t}\left(\frac{mv^2}{2}\right) = 0 \tag{2.6}$$

From this and $\mathrm{d}m/\mathrm{d}t = 0$ it is obvious that both, the particle's energy $\left(mv^2/2\right)$ as well as the magnitude of its velocity v are constant.
The electron or ion performs a *gyromotion* on circular orbit around the magnetic field lines. The *gyro-* or *cyclotron frequency* can be derived from (2.5) with the centrifugal force and yield

$$\omega_g = \frac{qB}{m} \tag{2.7}$$

and the *gyroradius*

$$r_g = \frac{v_\perp}{\left|\omega_g\right|} = \frac{mv_\perp}{|q|\,B} \tag{2.8}$$

with $v_\perp$ being the velocity perpendicular to the magnetic field **B**. Fig. 2.2 illustrates the motion of an ion and an electron. Since the direction of the gyromotion depends on the particle's charge, electrons and ions gyrate in opposite directions. The gyroradius is proportional to the mass of the particle, so the ion's gyroradius is much larger than the one of the electrons for the same $v_\perp$. The center of the gyromotion is called the *guiding center*.

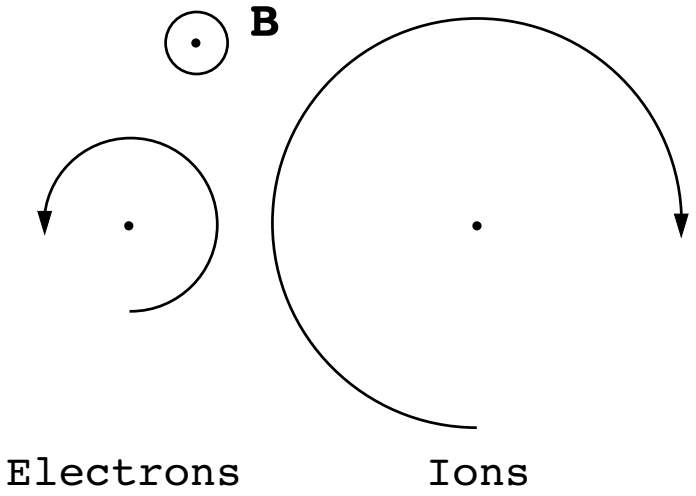

Figure 2.2: Gyromotion of electrons and ions.

A particle with a velocity component perpendicular to the magnetic field **B** performs a helix with the *local pitch angle*

$$\alpha = \tan^{-1} \frac{v_\perp}{v_\parallel} \tag{2.9}$$

with $v_\perp$ the velocity component perpendicular to the magnetic field **B**, and $v_\parallel$ the parallel component, see Fig 2.9. The local pitch angle α describes the angle between the velocity **v** of the particle and the magnetic field **B**. Magnetospheric charged particles perform a *bounce motion*. While they gyrate around the magnetic field lines, their local pitch angle changes as they move from the equator to higher latitudes. Since the magnetic field becomes stronger due to higher concentration of field lines, the local pitch angle converges to 90° and the particle is reflected and bounces back. The *drift* of a particle describes the bounce averaged change of position of the guiding center.

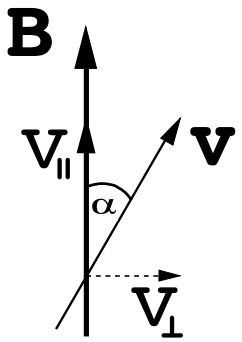

Figure 2.3: The pitch angle of an electrically charged particle is defined as the angle α between the magnetic field **B** and the velocity of the particle **v**.

2.2.2 E × B drift

In the presence of electric field **E** and magnetic field **B**, the particle experiences the **E** × **B** drift. In case of homogeneous electric and magnetic fields, the solution of the equation of motion (2.4) yields (Baumjohann and Treumann 1996)

$$\mathbf{v}_E = \frac{\mathbf{E} \times \mathbf{B}}{B^2} \tag{2.10}$$

where $\mathbf{v}_E$ is the drift velocity of the guiding center. The drift $\mathbf{v}_E$ is called the **E** × **B** drift. Fig. 2.4 illustrates the trajectory of a drifting ion and an electron. An ion gyrates around the magnetic field line and is accelerated while moving into the direction of the electric field **E** and decelerated while moving into the opposite direction. Thus the gyroradius increases and decreases during one gyroperiod and the ion performs a drift that is perpendicular to the electric as well as the magnetic field. Since the ion and the electron gyrate in opposite directions, the resulting **E** × **B** drift acts for both particles in the same direction, see Fig. 2.4.

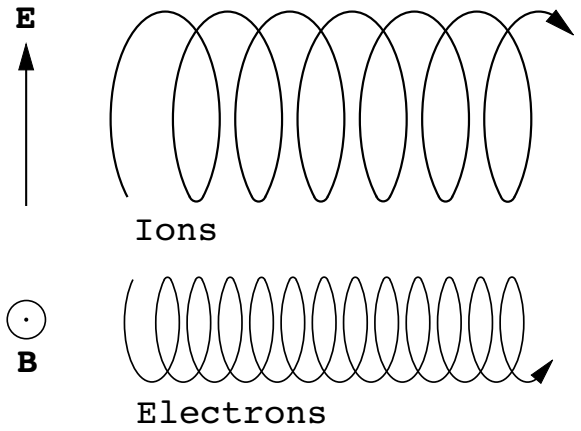

Figure 2.4: **E** × **B** drift for ions and electrons.

In a magnetosphere surrounding a rotating planet exists a radial electric field causing an azimuthal drift that corotates with the planet. This drift is called *rigid corotation* if the angular velocity is identical to the angular velocity of the planetary rotation. In large regions of Saturn's magnetosphere the drift is slower than this, which is called *subcorotation*.

2.2.3 Magnetic gradient and curvature drifts

Two major magnetic drifts in a planetary magnetosphere are the gradient and curvature drift. The gyroradius of a charged particle is related to the inverse of the magnetic field strength, see (2.8). In case of a spatially inhomogeneous magnetic field and a field perpendicular gradient, the gyroradius of a particle decreases when the particle moves during the gyromotion into the direction of the magnetic field increase, and vice versa. These variations lead to a drift motion perpendicular to the magnetic field and its gradient (Baumjohann and Treumann 1996)

$$\mathbf{v}_\nabla = \frac{mv_\perp^2}{2qB^3}(\mathbf{B} \times \nabla B) \tag{2.11}$$

The far magnetic field strength of a dipole with magnetic moment M can be obtained as

$$\begin{aligned} B &= \frac{\mu_0 M}{4\pi r^3}\left(1 + 3\sin^2\lambda\right)^{1/2} \\ &= \frac{\mu_0 M}{4\pi r^3}\left(1 + 3\cos^2\vartheta\right)^{1/2} \end{aligned} \tag{2.12}$$

with r the distance from the center of the dipole, λ the latitude, ϑ the colatitude, and μ_0 the magnetic permeability. In the equatorial plane of the dipole, (2.11) reduces to

$$v_{\nabla_\varphi} = \frac{6mv_\perp^2\pi r^2}{q\mu_0 M} \tag{2.13}$$

The gyrating particle experiences the centrifugal force due to their guiding center motion along the field line. This force yields the curvature drift

$$\mathbf{v}_C = \frac{mv_\parallel^2}{q}\frac{\mathbf{R}_c \times \mathbf{B}}{R_c^2 B^2} \tag{2.14}$$

where $\mathbf{R}_c$ is the local radius of curvature.
For particles in the equatorial plane, the drift can be written as

$$v_{C_\varphi} = \frac{12mv_\parallel^2\pi r^2}{q\mu_0 M} \tag{2.15}$$

The gradient and curvature drifts depend on the sign of the charge of the particle and of the magnetic moment of the dipole. Therefore the electrons move westward around the planet while the ions move eastward in the southward pointing magnetic field at Saturn, see Fig. 2.5.

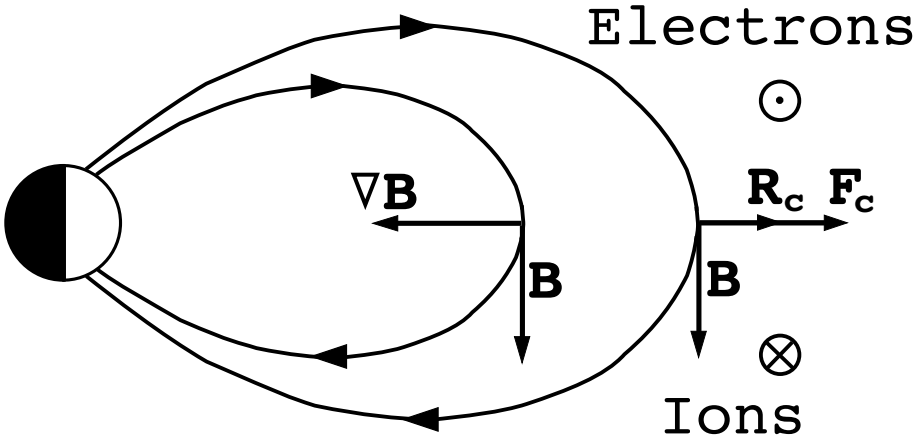

Figure 2.5: Magnetic gradient and curvature drift in Saturn's magnetic field configuration.

For a certain particle both drifts point into the same direction. They can be combined to the total magnetic drift $\mathbf{v}_B$

$$\mathbf{v}_B = \mathbf{v}_C + \mathbf{v}_\nabla = \left(v_\perp^2 + \frac{1}{2}v_\parallel^2\right)\frac{\mathbf{B}\times\nabla B}{\omega B^2} \tag{2.16}$$

2.3 Pitch angle distributions

The local pitch angle α is defined as the angle between the velocity $\mathbf{v}$ of the particle and the direction of the magnetic field vector $\mathbf{B}$, see (2.9) and Fig 2.3. We are interested in the collective behaviour of a huge number of particles rather than in a single particle. Therefore we analyse *distributions* of particles. The *pitch angle distribution* of a particle population can give clues about their origin and transport processes. Fig. 2.6 shows the pitch angle distribution at $L = 3$ R_E at different latitudes. Based on Walt (2005), the differential flux peaks at 90° and decreases to nearly zero at the atmospheric loss cone angle. If the mirror point of the particles reaches regions of the altitude of the atmosphere, the charged particles interact with atmospheric neutral gas and are lost. The flux of trapped particles is symmetric around 90° due to mirroring geometry. With increasing latitude λ, the PAD becomes more narrow. This is because particles with mirror points below the observed latitude do not reach the detector. The loss cone becomes larger with increasing mirror point, compare the PAD for equatorial particles ($\lambda = 0°$) and for particles mirroring at $\lambda = 40°$.

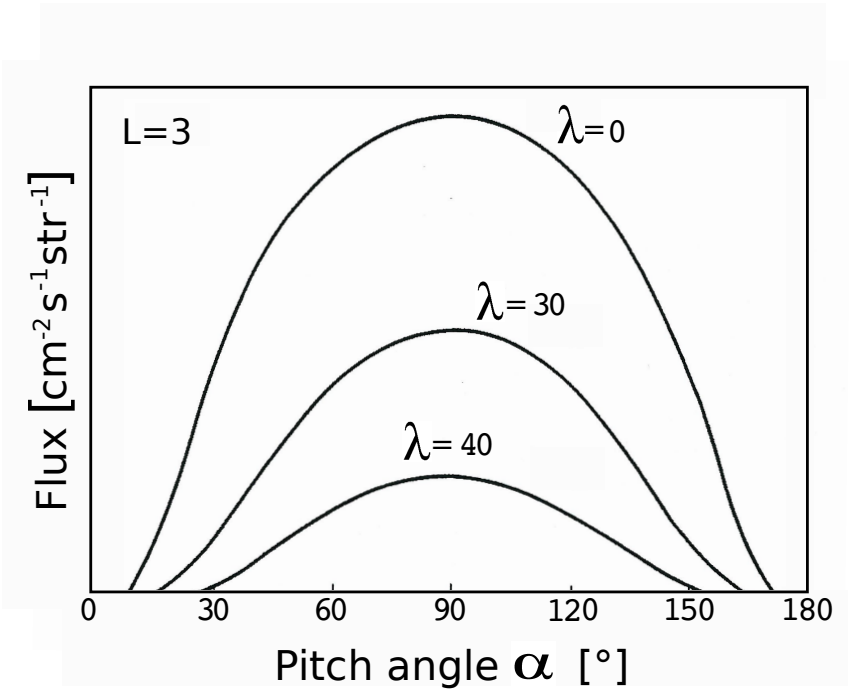

Figure 2.6: Typical pitch angle distributions at $L = 3$ R_S at three latitudes. With increasing latitude also the loss cone angle increases and the flux at 90° pitch angle decreases (Walt 2005). Here the pitch angle means the local pitch angle.

In general, four types of pitch angle distributions that typically can occur in a planetary magnetosphere, see Fig. 2.7

1. isotropic,
2. pancake,
3. field aligned, and
4. butterfly.

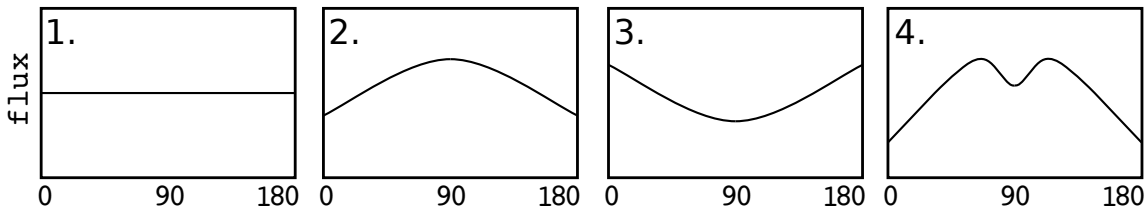

Figure 2.7: Different pitch angle distributions: 1. isotropic, 2. pancake, 3. field aligned, and 4. butterfly.

Rymer et al. (2008) have calculated the change of pitch angle distributions of radially and adiabatically transported energetic particles in a dipole field, as already discussed in section 1.3.3.1. Due to the conservation of the first and second adiabatic invariants (see section 2.4), the pitch angle distribution changes during adiabatic transport (see Fig. 2.8). The formation of a butterfly distribution is only explainable if non-adiabatic processes are involved additionally to radial transport. Interaction processes between charged particles and neutrals, confined in a equatorial neutral gas cloud - like the neutral gas torus or E-Ring - would affect the distribution of the pitch angle. The particles with pitch angles near 90° spend more time near the equator than particles with a high latitude mirror point. This increases the probability that equatorially mirroring particles are lost during a bounce period. An originally pancake distribution will end up in a butterfly distribution. Mitchell et al. (2009) reported on electron beams that show field aligned distributions. They can either be one- or bi-directional.
Besides adiabatic transport, pitch angles can also be modified via pitch angle diffusion. Diffusion in pitch angles can occur due to two processes: via collisions with neutral atoms or due to particle wave interactions. In the Terrestrial case, the particles collide with atmospheric atoms (loss cone scattering) and generate aurorae. At Saturn, the charged particles can also collide with the neutral gas torus or ice grains of the E-ring. Aurorae at Saturn were not only observed with the Cassini spacecraft but also with the Hubble Space Telescope (HST). Since the arrival of the Cassini spacecraft at Saturn, there have been several HST campaigns to observe auroral emissions at Saturn to allow scientists to compare spacecraft data with remote data taken at Earth (Gérard et al. 2006, Bunce et al. 2008). The two main types of plasma waves that cause pitch angle diffusion are whistler waves and ion cyclotron waves that have been reported at Saturn by Akalin et al. (2006) and Rodríguez-Martínez et al. (2010).

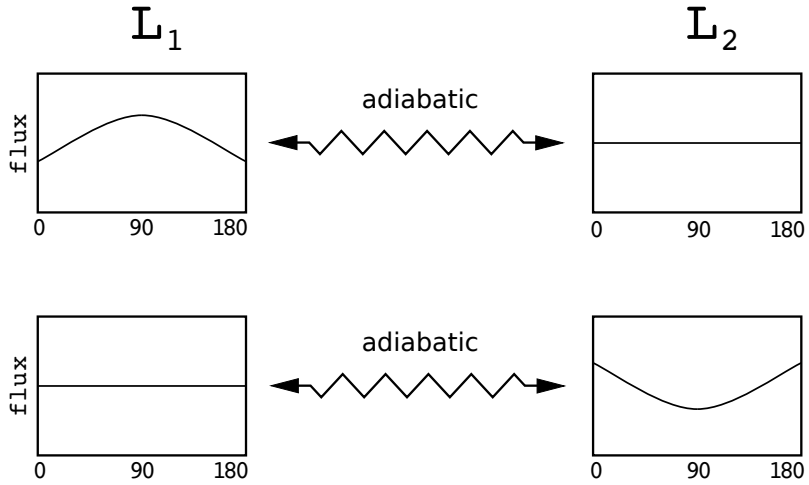

Figure 2.8: Concept of the change in pitch angle distribution due to adiabatic transport between L_1 and L_2. The particles are transported under the assumption of conservation of the first and second adiabatic invariants. Since purely adiabatic transport is fully reversible, this figure holds for a transport from L_1 to L_2 as well as for a transport from L_2 to L_1.

2.4 Adiabatic invariants

In every physical system that is periodic in the momentum component p_i and that only changes on timescales much larger than this periodicity, the adiabatic invariant J_i is conserved ($\omega_c << \omega$, where ω_c is the oscillation of change and ω the oscillation frequency of the particle). It is calculated using the action integral

$$J_i = \oint p_i \mathrm{d}q_i \tag{2.17}$$

where q_i represents the particle's coordinate. In plasma physics, the adiabatic invariants perform the role of constants of motion. The three adiabatic invariants are associated with the three basic motions that a charged particle undergoes within a planetary magnetic field if its energy is not too high: the first adiabatic invariant, or *magnetic moment* μ, the second adiabatic invariant, or *longitudinal invariant* J, and the third adiabatic invariant, or *total magnetic flux* Φ. The first and second adiabatic invariants are associated with gyro- and bounce motion of the charged particles. The timescales of gyro- and bounce motions are relatively fast, so that the invariants are conserved if the timescales of changes are longer than that of gyro- and bounce motion. Since the drift motion, that is related to the third adiabatic invariant is relatively slow, the validity of $\Delta\Phi = 0$ is not always applicable.
In the non-relativistic case, the magnetic moment can be expressed as (Walt 2005)

$$\mu \approx \frac{p_\perp^2}{2m_0 B} = \frac{mv_\perp^2}{2B} = \frac{mv^2 \sin^2 \alpha}{2B} \tag{2.18}$$

If $\Delta\mu = 0$, the local pitch angle α changes while the particle moves inside the dipole field of the planet. As the particle moves along the magnetic field line to higher latitudes, it moves to regions with enhanced magnetic field B. Since the total energy $(1/2)mv^2$ is

a constant of motion on the timescale of the gyromotion (if no changes faster than this occur) and μ has to be conserved, it is the local pitch angle α of the particle that changes and converges towards 90° while moving to increasing magnetic field, see (2.18). When $\alpha = 90°$ is reached, all the energy of the particle has been transferred into the perpendicular energy $W_\perp$ and the particle cannot penetrate any further since it does not have any parallel energy $W_\parallel$. The particle is then reflected and moves backwards along the field line. The point of mirroring is called the *mirror point latitude* λ_m with the magnetic field magnitude B_m. This concept is illustrated in Fig. 2.9. In a dipole magnetic field the particle bounces between the northern and southern magnetic mirror point $\pm\lambda_m$ and the particle becomes trapped. During each bounce, the particle pass the equator, where it has the equatorial pitch angle α_{eq}. To compare pitch angle distributions of particles measured at different latitudes λ, it is meaningful not to compare their local pitch angle α but their equatorial pitch angle α_{eq}. It can be derived from the conservation of μ as

$$\alpha_{eq} = \arcsin\left(\sin\alpha\sqrt{\frac{B_{eq}}{B}}\right) \tag{2.19}$$

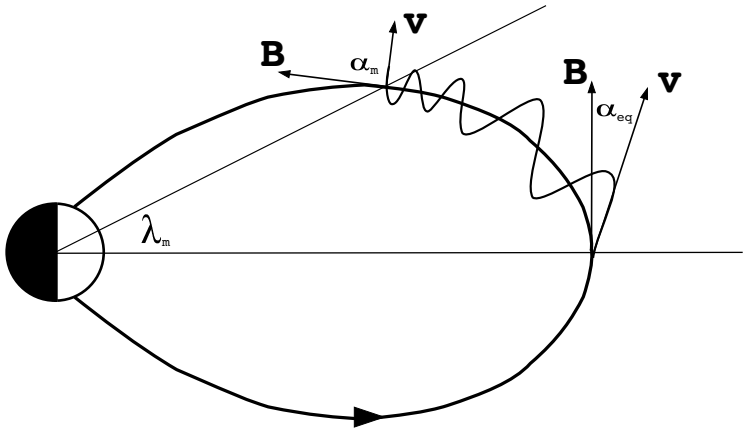

Figure 2.9: Concept of mirroring particles: At the equator an energetic particle has the equatorial pitch angle α_{eq}. While the particle undergoes gyration and bounce motion, the magnetic field B changes and so does the local pitch angle until it reaches $\alpha_m = 90°$ and is reflected, see (2.18). λ_m is called the *mirror point latitude*.

In conformity with Baumjohann and Treumann (1996), the second adiabatic or longitudinal invariant is defined as

$$J = \oint m v_\parallel \mathrm{d}s \tag{2.20}$$

where the integration covers a full bounce path and ds represents an element of the guiding center path. The third adiabatic or drift invariant can be written as

$$\Phi = \oint_{\psi=0}^{2\pi} v_d r \mathrm{d}\psi \tag{2.21}$$

with v_d the sum of all perpendicular drift velocities and ψ the azimuth angle.

2.5 Dispersion theory

We now introduce the dispersion theory that will be applied for the injection studies. After the ions and electrons are injected into the inner magnetosphere they experience, additionally to the energy and charge independent $\mathbf{E} \times \mathbf{B}$ drift, the magnetic curvature and gradient drift caused by the inhomogeneous magnetic field of the planet. Compared to the drift timescales of injected particles, the radial inward transport of the energetic plasma population due to the centrifugal interchange instability or reconnection in the magnetotail takes place on short timescales. Burch et al. (2005) estimated the planetward speed of the electrons and ions at Saturn with 25 km s^{-1}, whereas in our model we assume an instantaneous population of energetic particles in the inner magnetosphere.

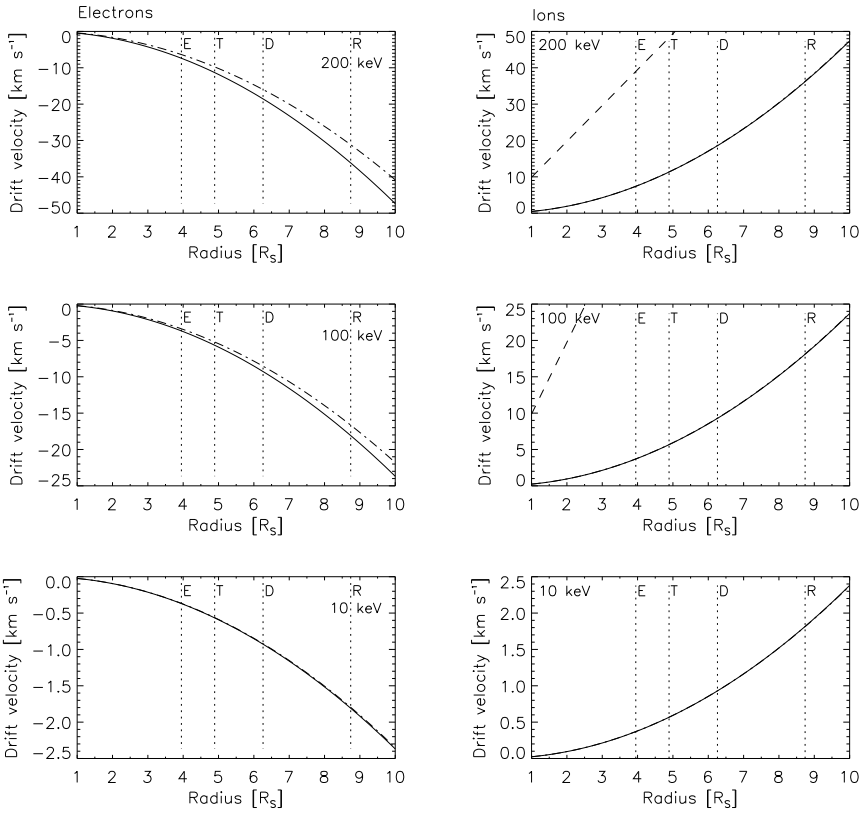

Figure 2.10: Magnetic gradient and curvature drift velocities for electrons (left) and ions (right) with equatorial pitch angle of 60° of typical energies of 10, 100, and 200 keV (from bottom to top). The dashed dotted line in the electron plot is the non-relativistic drift velocity based on (2.16) whereas the solid line marks the velocity for relativistic electrons, based on (2.22). The dashed line in the ion plots denotes the rigid corotation speed. The vertical dotted lines mark the orbits of the inner Saturnian moons Enceladus, Tethys, Dione and Rhea. While we assume a simple magnetic dipole field, our obtained values are in good agreement with Khurana et al. (2008).

Fig. 2.10 shows typical magnetic gradient and curvature drift velocities for electrons and ions in the assumed dipole field configuration of Saturn. Following Connerney et al. (1984), the assumption of a dipolar configuration of the Saturnian magnetic field is justified in our analysed L-shell range (Saur et al. 2004). The total magnetic drift velocity, meaning the sum of curvature and gradient drift, is for a 10 keV electron with an equatorial pitch angle of 60° about 0.37 km s^{-1}, and 6.42 km s^{-1} for a 200 keV electron at the orbital distance of Enceladus (3.95 R_S), see also Fig. 2.10. After Mauk et al. (2005), the relativistically correct and bounce averaged magnetic gradient and curvature drift velocity in the Kronian magnetosphere can be written as

$$\Omega_d = 3.94 \cdot 10^{-5} \left(\frac{q}{q_0}\right) E \frac{(E/2 + m_0c^2)}{(E + m_0c^2)} [LH] \tag{2.22}$$

where q is the charge of the particle, q_0 is the proton charge, E the energy of the particle in MeV, m_0c^2 its rest energy, $L = R/(\cos^2 \lambda)$ the McIlwain L-parameter or drift shell, and $H \cong 0.7 + 0.3 \cdot \sin(\alpha_{eq})$, with α_{eq} being the equatorial pitch angle of the particle, see (2.9).
Following Paranicas et al. (2007), the total angular velocity of drifting particles $\Omega(L, E, \alpha)$ can be expressed as the sum of the angular velocity of the magnetosphere $\Omega_0(L)$ and the magnetic curvature and gradient drift $\Omega_d(L, E, \alpha)$

$$\Omega(L, E, \alpha) = \Omega_0(L) + \Omega_d(L, E, \alpha) \tag{2.23}$$

We assume that the particles of an injection event are instantaneously transported inward and are then distributed at a certain azimuthal position along a non-zero radial extent. Furthermore, we assume that drift takes place only in the azimuthal direction and that the particles travel on circular orbits. After Mauk et al. (2005) the dispersion relation dE/dt, that describes the energy of the injection as a function of time, can be written as

$$\frac{\mathrm{d}E}{dt} = \frac{\partial E}{\partial \phi} \frac{\mathrm{d}\Phi}{dt} + \frac{\partial E}{\partial L} \frac{\mathrm{d}L_{SC}}{\mathrm{d}t} \tag{2.24}$$

with ϕ and L being the azimuthal and L-shell position of drifting particles, and Φ and L_{SC} the positions of the spacecraft. Under the assumption that the particle population exhibits a radial extension and that electrons and ions just drift azimuthally, the following relations apply

$$\begin{aligned}
\frac{\partial E}{\partial L} &= \left(\frac{\partial E}{\partial \phi}\right)\left(\frac{\partial \Phi}{\partial L}\right) \\
\frac{\partial \phi}{\partial E} &= \left(\frac{d\Omega_d}{dE}\right) \cdot T_A \\
\frac{\partial \Phi}{\partial L} &= \left(\frac{d\Omega_0}{dL} + \frac{d\Omega_d}{dL}\right) \cdot T_A \\
\frac{d\Phi}{dt} &= \Omega_{SC} - \Omega_0 - \Omega_d \\
\frac{dL_{SC}}{dt} &= v_L
\end{aligned}$$

with (t - t_i) = T_A the age of the injection when being detected, Ω_{SC} the azimuthal, and v_L the L-shell, i.e. mostly radial, velocities of the spacecraft. Inserting these in (2.24), the dispersion relation can be written as

$$\frac{\mathrm{d}E}{\mathrm{d}t} = \frac{(\Omega_{SC} - \Omega_0 - \Omega_d)}{(t - t_i)(\mathrm{d}\Omega_d/\mathrm{d}E)} - \frac{v_L[(\mathrm{d}\Omega_0/\mathrm{d}L) + (\mathrm{d}\Omega_d/\mathrm{d}L)]}{\mathrm{d}\Omega_d/\mathrm{d}E} \tag{2.25}$$

Ω_0 and T_A are the only unknown parameters in (2.25). These values will be constrained by a least-mean-square fit of the modelled $E(t)$ from (2.25) (E_{th}) and the observed energy as a function of time (E_{obs}) in section 4. Fig. 2.11 shows a Jupiter-oriented dispersion profile as would be observed with a non-moving particle detector in the magnetosphere. The high energetic ions are observed first, followed by the low energetic ions, then the detector would measure the low energetic electrons and finally the high energetic electrons.

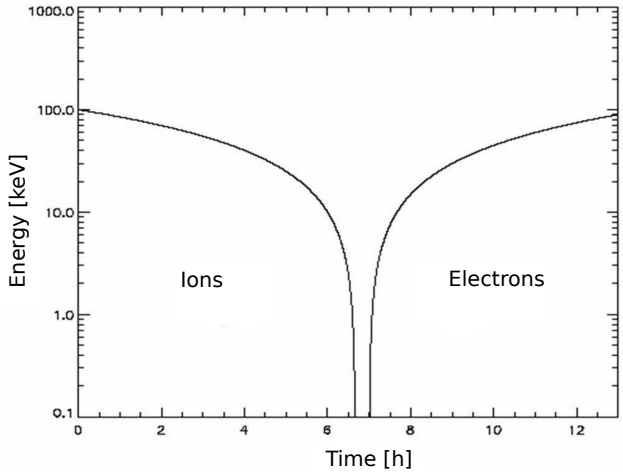

Figure 2.11: Theoretical ion and electron dispersion profile (Müller 2007).

3 Instrumentation

3.1 The Cassini spacecraft

Figure 3.1: Cassini with Huygens probe. Left hand side: picture of the spacecraft before launch, see engineers for size comparison. Image courtesy of NASA/JPL/SSI. Right hand side: model of the Cassini spacecraft at JPL, January 2008.

The Cassini spacecraft was launched in October 1997 from Cape Canaveral Air Force Station and arrived in the Saturnian system after a seven years journey through the solar system in July 2004. It's nominal mission ended already in June 2008. It was then extended until September 2010, and was named Cassini Equinox Mission. Saturn's equinox occurred in August 2009, when the planets orientation led the sun shine parallel to the plane edge of its ring system. In February 2010, NASA extended the mission for a second time, until 2017 (Solstice Mission). Altogether, the spacecraft will then have spent 13 years at Saturn. This is more than one Solar magnetic activity cycle, which last for about 10.7 years. This allows scientists to observe periodicities in the Saturnian system that are caused by changing solar activity.
The mission consists of a spacecraft, the Cassini orbiter (named after the French astronomer Giovanni Domenico Cassini) and the Titan lander Huygens (named after the Dutch astronomer, mathematician and physicist Christiaan Huygens). The Huygens probe

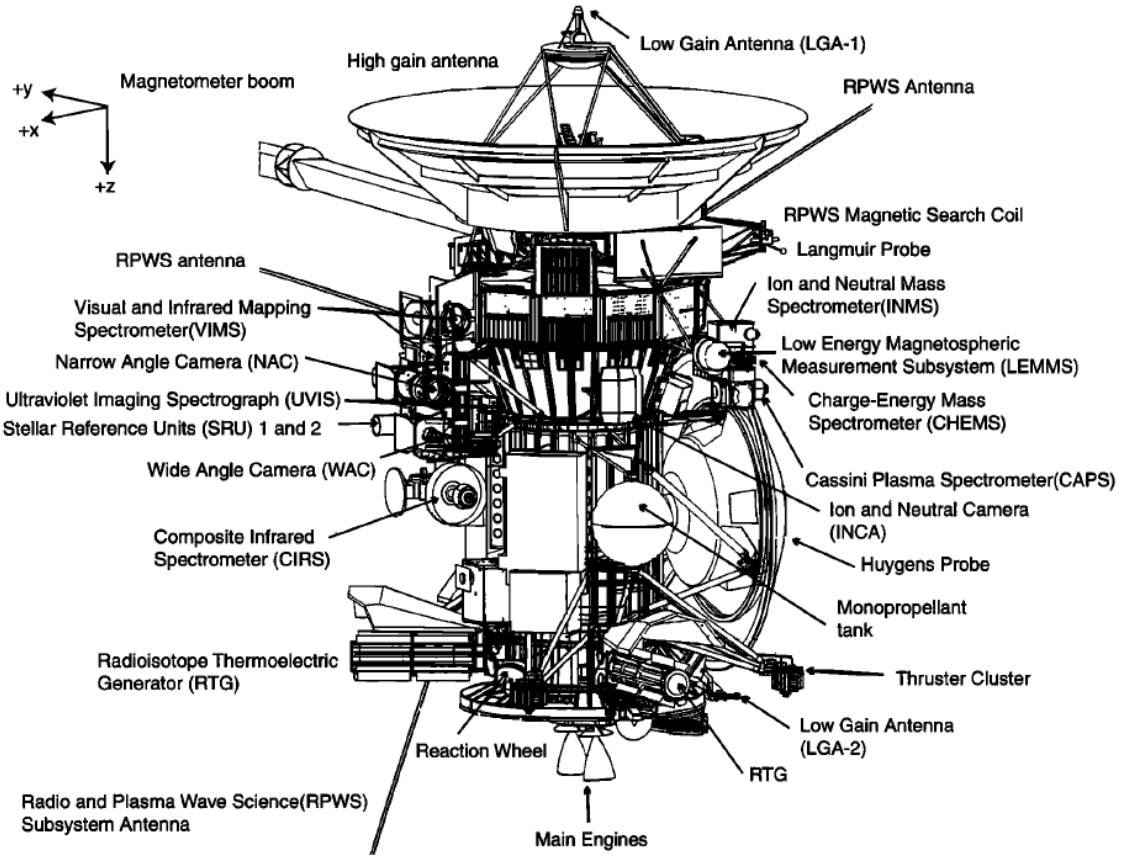

Figure 3.2: Sketch of the Cassini spacecraft with instrumentation (Burton et al. 2001).

descent took place in January 2005, where in-situ measurements of the atmosphere and surface were made.
The instruments of the Cassini orbiter can be divided into three subclasses:

- optical remote sensing,
- in-situ measurements of fields, particles and waves, and
- microwave remote sensing,

with altogether 12 scientific instrument packages. The primary objectives of the Cassini mission are the study of the ring system, satellites, magnetosphere, atmosphere, and the atmosphere and surface of Titan, Saturn's largest moon. Scientific goals for the magnetosphere of Saturn are the

- temporal variability of the plumes of Enceladus,
- seasonal and solar cycle induced variability of the magnetosphere,
- seasonal variations of the ionosphere ot Titan,

- dynamics of the magnetotail of Saturn,
- coupling between the ionosphere and inner radiation belts,
- coupling between the ionosphere and ring system, and
- magnetopheric periodicities.

In this thesis, we present data of the Magnetospheric Imaging Instrument (MIMI) that consists of three detectors. It will be described in section 3.2. Some of the data we use are obtained with the help of Magnetometer (MAG) data.

3.2 Magnetospheric Imaging Instrument: MIMI

One of the particle instruments onboard Cassini is the Magnetospheric Imaging Instrument, that is designed to perform global imaging as well as in-situ measurements. The instrument consists of three different sensors, the *Low Energy Magnetosphere Measurement System* (LEMMS), the *Charge Energy Mass Spectrometer* (CHEMS), and the *Ion and Neutral Camera* (INCA). This package of sensors enables us to perform global imaging as well as in-situ measurements of the magnetosphere.
In our work we have concentrated on the data analysis of LEMMS, hence a detailed description of the instrument and its functionality is given in section 3.2.1.

3.2.1 Low Energy Magnetosphere Measurement System: LEMMS

The Low Energy Magnetosphere Measurement System is designed to measure the three-dimensional distributions of energetic ions and electrons in the energy range between a few 10 keV up to the MeV range. LEMMS consists of two detector heads, the low energy (LE) end that measures particles with energies below 1-2 MeV, and the high energy (HE) end that also measures particles with energies above a few MeV. Mounted on a rotating turntable, LEMMS is able to perform a two dimensional scan of the pitch angle distribution (see Fig. 3.3). Within 86 seconds it rotates about the y-axis of the spacecraft, which means the time resolution of pitch angle distribution is 86 seconds if the turntable rotates. Combined with spacecraft rotation even a three dimensional scan of the particles' distribution is possible. Early in 2005, the turntable of LEMMS stopped rotating. Therefore it only measures two directions with its two detector heads. This increases the time resolution at the according pitch angle. Full pitch angle distributions can only inferred if the spacecraft itself is spinning.
The LE and HE detectors are divided into different energy channels for different energies and mass ranges, see table 3.1 for different passbands of the energy-channels. Note that the energy ranges differ from the ones given in Krimigis et al. (2004) since the calibration of the different energy channels is still an ongoing project. We use the current calibration given in Krupp et al. (2009).

In this thesis, we mostly use electron data from the electron rate channels (C0 - C7), for which the typical time resolution is ~ 5 sec per data point. For some of our data analysis we also use the so called PHA channels. To obtain a higher energy resolution, LEMMS uses a pulse height analyser (PHA) that divides an electron spectrogram into 128 energy bins.

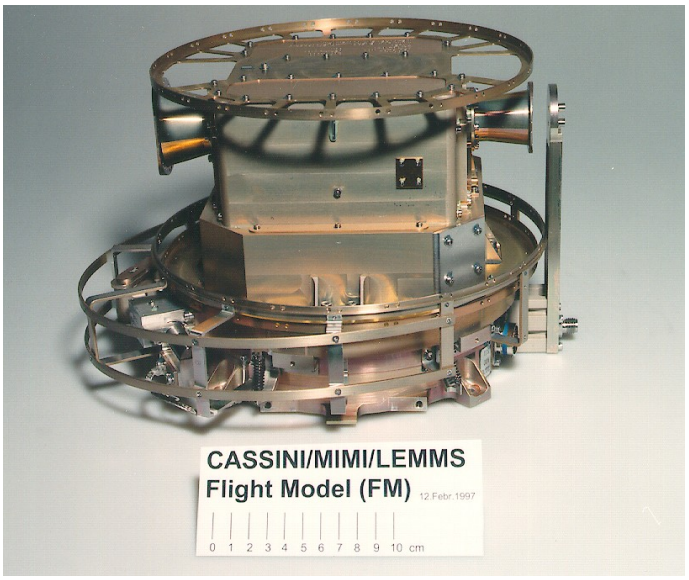

Figure 3.3: Flight model of the LEMMS detector, mounted on the rotating turntable.

Due to the energy range LEMMS is measuring, the method used is the energy deposition of energetic particles in semiconductors. The configuration and positions of the 11 semiconductor silicon detectors are shown in Fig. 3.4. The low energy end is meant to measure electrons between 15 keV and 1 MeV, as well as ions with energies higher than 30 keV up to several MeV. To separate ions and electrons, an inhomogeneous magnetic field is produced inside the detector (see Fig. 3.4, right hand side). Trajectories of electrons are shown in red, while the trajectories of the ions are displayed in green.
To obtain the pitch angle of a particle, we need knowledge of the LEMMS pointing as well as the background magnetic field orientation. Due to the design of the LEMMS detector head, it measures particles from a fraction of the 360° unit sphere.

3.2.2 CHEMS and INCA

The Charge Energy Mass Spectrometer (CHEMS) utilizes electrostatic deflection, combined with a time of flight detector (TOF) and energy measurements in a solid state detector. It detects ions (up to mass of iron) in a range between 10 KeV/charge and 220 keV/charge.
The Ion and Neutral Camera (INCA) is a time of flight detector that analyses the composition and direction of motion of incident energetic neutral atoms and ions in the energy range from 7 keV/nucleon to 3 MeV/nucleon.

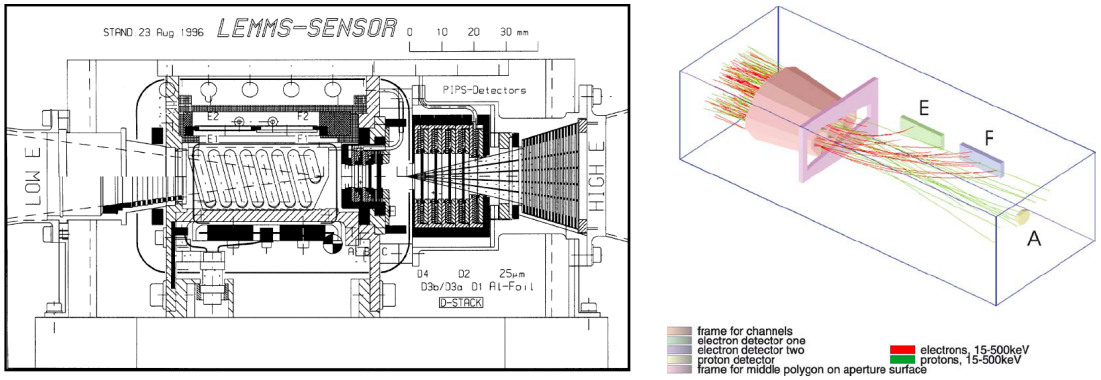

Figure 3.4: Configuration of the LEMMS detector head (left) and sketch of simulations of particle trajectories in the low energy end (Krimigis et al. (2004)).

Sensor head	Channel	Energy of ions [keV]	Channel	Energy of electrons [keV]
LE	A0	27 - 35	C0	18 - 40
LE	A1	35 - 56	C1	27 - 48
LE	A2	56 - 106	C2	41 - 60
LE	A3	106 - 255	C3	56 - 100
LE	A4	255 - 506	C4	92 - 183
LE	A5	506 - 805	C5	175 - 300
LE	A6	805 - 1600	C6	265 - 550
LE	A7	1615 - 4000	C7	510 - 832
HE	P1	1424 - 2278	E0	110 - 365
HE	P2	2280 - 4492	E1	220 - 485
HE	P3	4491 - 5744	E2	340 - 1350
HE	P4	13,200 - 25,400	E3	600 - 4950
HE	P5	8311 - 11,449	E4	790 - 4750
HE	P6	11,474 - 13,433	E5	800 - 2800
HE	P7	12,101 - 58,902	E6	1600 - 21,000
HE	P8	25,185 - 59,000	E7	7000 - 20,000

Table 3.1: List of the most commonly used LEMMS energy channels and their energy ranges (Krupp et al. 2009).

4 Azimuthal plasma flow

4.1 Drift paths and dispersion profiles

Measurements of the radial velocity profile are crucially important for understanding the dynamics of the magnetosphere of Saturn. They constrain the coupling of the magnetosphere to Saturn's ionosphere and also provide important information about internal processes such as mass loading and radial plasma transport (e.g. Cowley and Bunce 2003, Saur et al. 2004, Pontius and Hill 2009). Mass loading in the magnetosphere occurs mainly by means of two processes: photo and electron impact ionization. Due to charge exchange processes, momentum but no mass from the neutral cloud is drained from the corotating plasma and transferred to the newly generated ions by charge exchange, photo- or electron ionization. All these three processes contribute to the corotation lag of the magnetospheric plasma because the neutrals orbit Saturn with the Keplerian speed which is much slower than the rigid corotation speed (Saur et al. 2004).

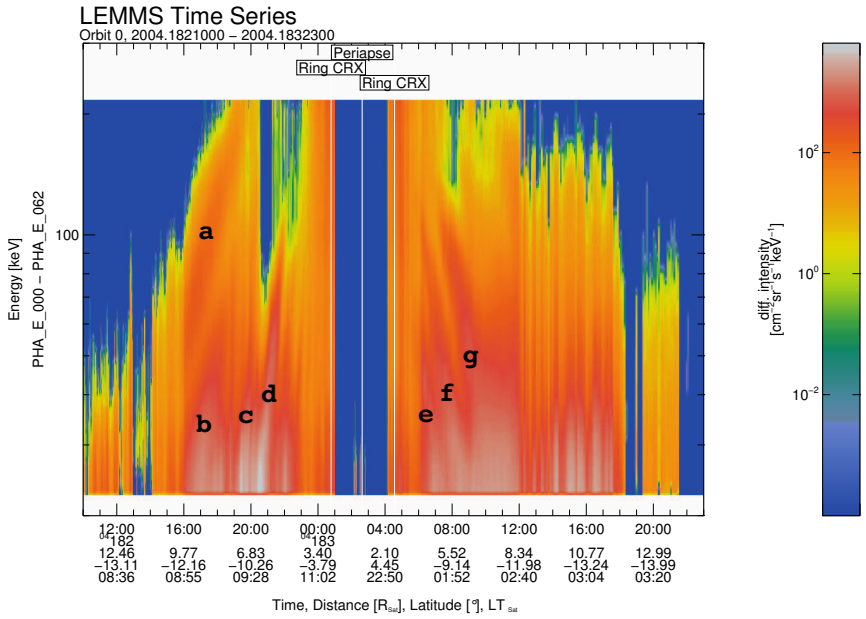

Figure 4.1: Energy-time-spectrogram of Saturn Orbit Insertion (SOI) electron data. Clear signatures of injections are visible around closest approach. 'Normal' injections are marked with (a), (b), (c), and (d), the 'inverted' events are marked with (e), (f), and (g).

Figure 4.1 shows an electron energy spectrogram of days 2004/182 - 183. Closest approach to Saturn was at 01:20 UT. Around this time clear dispersion profiles can be seen. The most dominant injections are marked from (a) to (g). On the inbound path of the spacecraft the profiles (a) to (d) show the Jupiter-like orientation, i.e the low energetic electrons are measured prior to the high energetic ones. However, when Cassini departs from the planet, the profiles appear in a reversed manner, which means the high energetic part arrives in the detector before the low energetic one. In Fig. 4.1, this is revealed by the structures (e) to (g) measured between 07:30 UT and 12:00 UT, DOY 183 on the outbound path of the Cassini trajectory.
In order to reproduce the dispersed features of an injection event, we first assume that the particles of this event have been instantaneously transported inward. To clarify the evolution of the energetic particle population and in order to explain the inverted electron profiles, we have calculated the evolution of drift angles for different species at different energies, based on the drifts given in (2.22). Magnetic drifts of electrons and ions are in opposite directions (electrons move westward and ions move eastward with respect to the cold plasma), while the corotational $\mathbf{E} \times \mathbf{B}$-drift is energy-independent and eastward for both species. In order to calculate the total drift $\Omega(L, E, \alpha)$ of a particle, these drifts have to be combined, see 2.23.

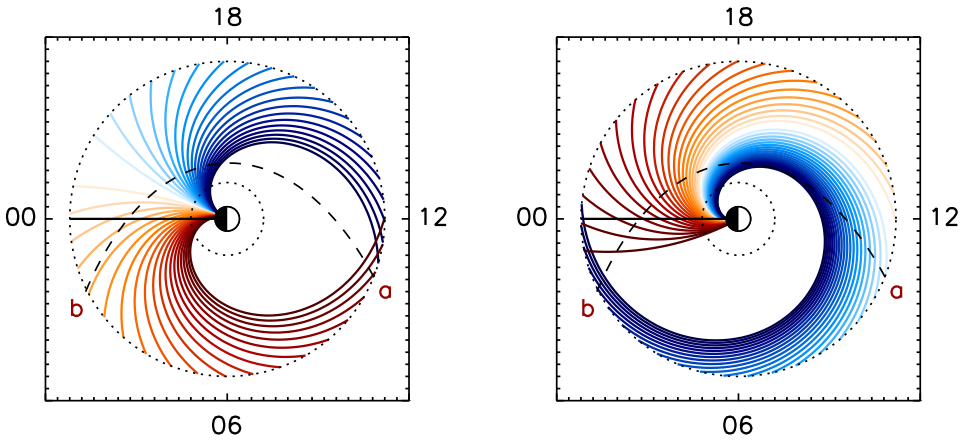

Figure 4.2: Top-view of the L-shell range up to 13 R_S. Drift angles of electron (blue) and ion (red) energies after an injection time of 10 h are displayed. 10 keV electrons are displayed in light blue, 200 keV electrons in dark blue with ΔE = 10 keV between two neighbouring lines. Ions span the same energy range from 10 keV (yellow) to 200 keV (dark red). Particles were injected along the black line at local midnight. The trajectory of the Cassini trajectory of day 2005/302 - 2005/304 is displayed as a dashed line, going from point (a) to point (b). For the left panel we assumed rigid corotation whereas on the right hand side we assumed an azimuthal plasma flow profile that decreases linearly from rigid corotation to 50 % of corotation at a radial distance of 13 R_S, to show the effect on the drift angles.

Fig. 4.2 shows two different scenarios to illustrate the dependence of the drift angle of the particle on the amount of corotation: on the left hand side the drift angles for electrons and ions are calculated for a rigidly corotating magnetosphere, on the right hand side the

same calculations were made, but the plasma does not rigidly corotate. The azimuthal velocity decreases linearly from rigid corotation at 3 R_S to 50 % of corotation at 13 R_S. The trajectory of the spacecraft of 2005/302 00:00 - 2005/304 00:00 goes from point (a) to point (b) in Fig. 4.2. An energetic particle detector at a fixed radial distance and azimuth would first measure the high energetic ions, subsequently the low energetic ones, then the low energetic electrons and finally the high energetic electrons, as shown in Fig. 2.11. With this simple picture, the dispersion profiles observed at Jupiter could be well explained (Mauk et al. 1999). But in the case of Saturn, on almost each outbound path of the spacecraft trajectory, inverted electron profiles are revealed by the data. That means the electrons arrive in the detector opposite to the anticipated manner, see Fig. 4.1. Fig. 4.2 illustrates the scenario how these inverted electron profiles can be measured. On the outbound path of the trajectory, the velocity of the spacecraft is high enough to overtake the narrow spiral structure of energetic electrons. Therefore, the energetic particle detector measures the high energetic electrons prior to the low energetic portion of the distribution. To explain the slope of the inverted dispersion profiles as injections (e), (f), and (g) in Fig. 4.1, a velocity profile is needed that decreases with increasing radial distance.
As can be seen in Fig. 4.2, the spiral of the ions is much less wound, hence inverted ion profiles have not been observed. Even though it is possible to obtain inverted electron profiles with the assumption of a rigidly corotating magnetosphere, the slope of these is not steep enough to match the data.

4.2 Dataset and detection of injections

An injection event appears in the intensity or count rate line plots of the different energy channels at different times. For normally oriented injections, LEMMS measures for the energy E_0 at time t_0 the peak intensity $I_{0,max}$ or count rate $c_{0,max}$. For the next energy channel with $E_1 > E_0$, LEMMS measures at time t_1 the peak intensity $I_{1,max}$ or count rate $c_{1,max}$, see Fig. 4.3. To compare theoretical dispersion profiles (E_{th}) with observed ones (E_{obs}), we first extract the energy as a function of time from the data. We then numerically calculate dispersion profiles with different ages for the individual injections and for different azimuthal plasma flow profiles. We compare this two dimensional set of dispersion profiles $E_{th}(T_A, \Omega)$ with a least-mean-square fit to the data. Applying this method, we obtain ages for the individual injections and a global model for the plasma flow in the magnetosphere.
To obtain the energy of an injection event as a function of time, we followed the maxima of the event in the different PHA-channels. We have chosen the PHA channels to obtain a much better energy resolution than with the normal electron channels. The blue dots in Fig. 4.3 represent our selection criteria for injection events. We just considered signatures for our analysis that show a peak width c_w at 3/4 of the maximum value c_{max}

$$c_w = \frac{3}{4} c_{max} \tag{4.1}$$

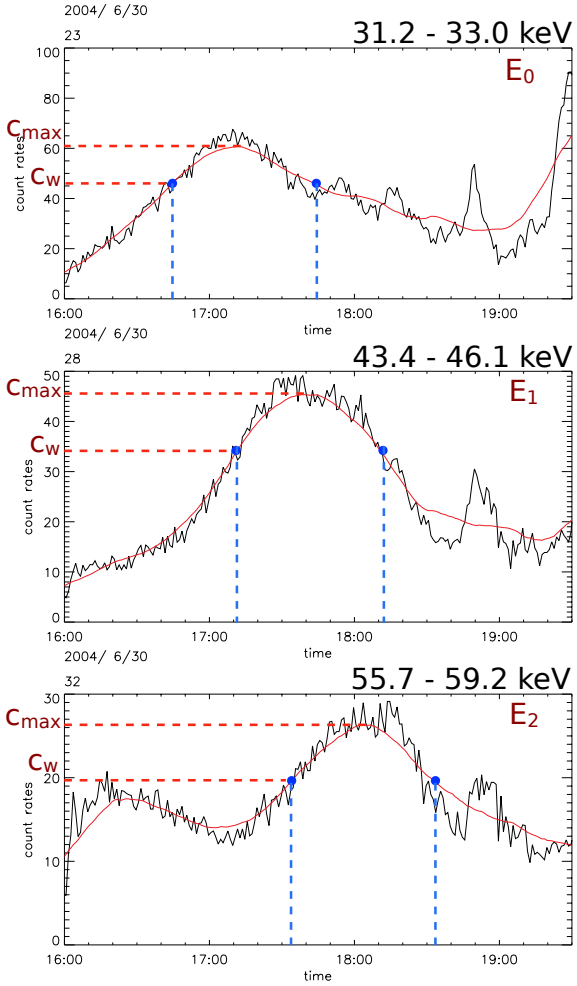

Figure 4.3: Count rates $\left[\text{counts sec}^{-1}\right]$ as a function of time for different PHA energy channels. The injection event (b) of Fig. 4.1 is shown. The red curve represents smoothed data.

The observed energy profile E_{obs} is obtained by deriving $E_j(t_j)$ from the data. The energy of the different PHA channels was obtained by taking the geometric mean

$$\overline{E}_j = \left(\prod_{k=1}^{n} E_{j,k} \right)^{-1/2}$$

with $n = 2$ and $E_{j,1}$ and $E_{j,2}$ the lower and upper energy of the energy passband of the PHA channel j (see Tab. 3.1). Fig. 4.3 and 4.4 show the injection event (b) of Fig. 4.1 in the line-plot illustration and as an energy-time spectrogram.
Due to our selection criteria (4.1) and due to the fact that the model apply close to the equator our dataset is limited to 52 injection events. Eq. (2.25) does not consider a latitudinal velocity of the spacecraft, so we had to exclude passages where the trajectory of Cassini differed from equatorial tracks. Moreover, some of the injections are very faint or superimposed on other dynamical events. These events could not be used for our study. The 52 injection events, retrieved from the MIMI/LEMMS data between June 2004 (SOI)

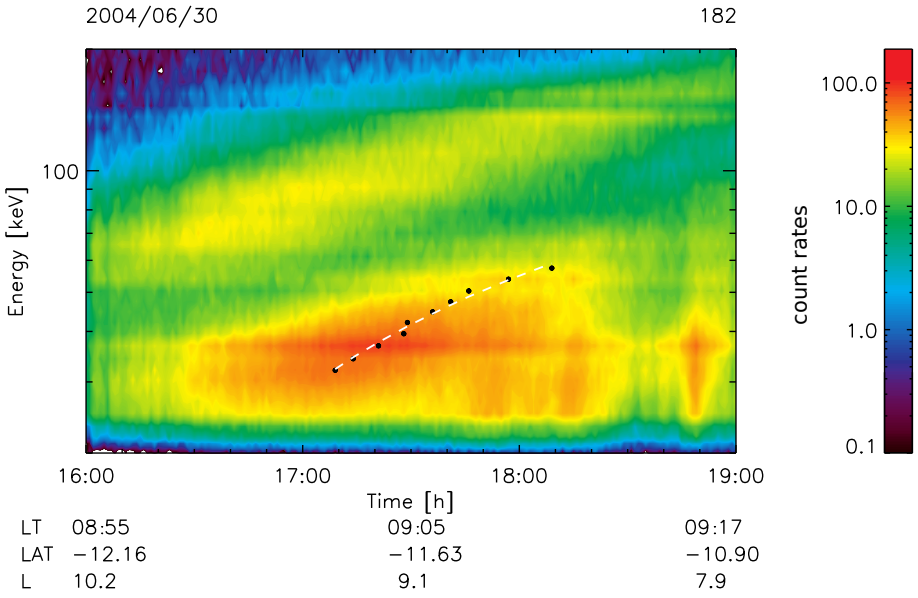

Figure 4.4: Energy-time-spectrogram of injection (b) of Fig 4.1, see also Fig. 4.4. The black points correspond to the count rate maximum of the different PHA channels. The white dashed line represents the linear fit through the energy channels.

and the end of 2007, represent a subset of much more observed injection events. During the nominal and one year of extended mission of Cassini, MIMI/LEMMS detected more than 800 events. About 40 % of the subset of events were observed within a latitudinal range smaller than ± 1°, 21 % between ± 1° and 10°, 31 % between ± 10° and 20°, 6 % between ± 20° and 30° and 2 % between ± 30° and 40°. These observations are biased by the trajectory of the spacecraft.

4.3 Plasma flow model

To represent the real velocity profile better than the simple assumption of one linear decrease, we separated the radial range into three parts: from 3 R_S to 6.3 R_S, from 6.3 R_S to 9.6 R_S, and from 9.6 R_S to 13 R_S. The velocity can have different linear slopes in each sector. In each of these ranges the injection events were binned together. In each bin the injections were allowed to have different ages, but they all experience the same angular velocity profile, which is assumed not to change in time.
To characterize $\Omega_0(L)$ adequately, we assume for each injection event an individual linear angular velocity profile as a function of L

$$\Omega_0(L) = \Omega_1 \frac{(L_2 - L)}{(L_2 - L_1)} + \Omega_2 \frac{(L - L_1)}{(L_2 - L_1)} \tag{4.2}$$

where L_1 and L_2 are the innermost and outermost L-shells of the different L-shell bins, Ω_1 and Ω_2 are the corresponding angular velocities at these distances. By binning the injections and separating the radial range of interest into different sections, we permit the magnetosphere of our model to recover from subcorotation, in contrast to the model used

by Mauk et al. (2005). Their model only allowed a decrease of the azimuthal plasma velocity with increasing radial distance.
The binning of the injections was done to increase the statistics and thus to better constrain the free parameters in Eq. (2.25) and Eq. (4.2), i.e. (Ω_1, Ω_2, and $t - t_i = T_A$). Increasing the number of bins obscures the dependence of the velocity profile on radial distance. More bins result in a more poorly constrained velocity profile with larger error bars, and less bins give less spatial information.
First we perform a least-mean-square fit for all our individual injection events in the first bin between 3 R_S and 6.3 R_S. In the first bin we assumed rigid corotation for Ω_1 at $L = 3$ R_S (Mauk et al. 2005, Wilson et al. 2009). We allowed the two remaining parameters Ω_2 to vary within 10 % and 110 % of rigid corotation and T_A to vary between 1 and 48 hours, and constrained their values by a least mean square fit. We assumed stationarity for the azimuthal velocity and thus assumed the same Ω_1^j and Ω_2^j for each injection event i in an individual bin j, but each injection event i was allowed to have varying ages T_i^j. Thus we searched for a minimum of $\chi^2_{sum,j}$ in each bin, where

$$\chi^2_{sum,j} = \sum_i \chi^2(T_i^j, \Omega_2^j)$$

$$\text{with } \chi^2 = \frac{1}{n} \sum_n \frac{(E_{th}(T_i^j, \Omega_2^j) - E_{obs})^2}{E_{obs}^2}$$

where n is the number of data points of an individual injection event. For the second and third bin Ω_1^j is identical to Ω_2^j of the previous bin, i.e. $\Omega_2^{j-1} = \Omega_1^j$ for $j > 1$ due to continuity of the velocity profile and $\Omega_1^1 = \Omega_{cr}$, with Ω_{cr} being rigid corotation.

4.4 Azimuthal plasma flow

The role of the neutrals on the dynamics of Saturn's magnetosphere became of particular relevance after the discovery of a strong neutral mass source of 200 kg s^{-1} or more due to the cryovolcanism on Enceladus (Waite et al. 2006, Dougherty et al. 2006, Burger et al. 2007, Tian et al. 2007, Saur et al. 2008).
Analyzing the 52 detected injection events with the mathematical approach of dispersion theory, introduced in sections 2.5 and 4.3, we derive the azimuthal angular velocity in the radial range approximately coinciding with the E-ring and the neutral gas cloud of Enceladus. Results of our determination are shown in Fig. 4.5. The magnetospheric plasma clearly shows subcorotation beyond 3 R_S. In our model, the angular velocity decreases from rigid corotation at 3 R_S over 85 % at 6.3 R_S to 76 % at 9.6 R_S and reaches 79 % at 13 R_S. The error range χ^2_{err} was determined with the least-mean-square values of the fit, $\chi^2_{err} = 2 \cdot \chi_{min}$, and gives 78 % to 90 % of corotation at 6.3 R_S, 71 % and 83 % of corotation at 9.6 R_S and 59 % and 92 % of corotation at 13 R_S. These values are summarised in Tab. 4.1.

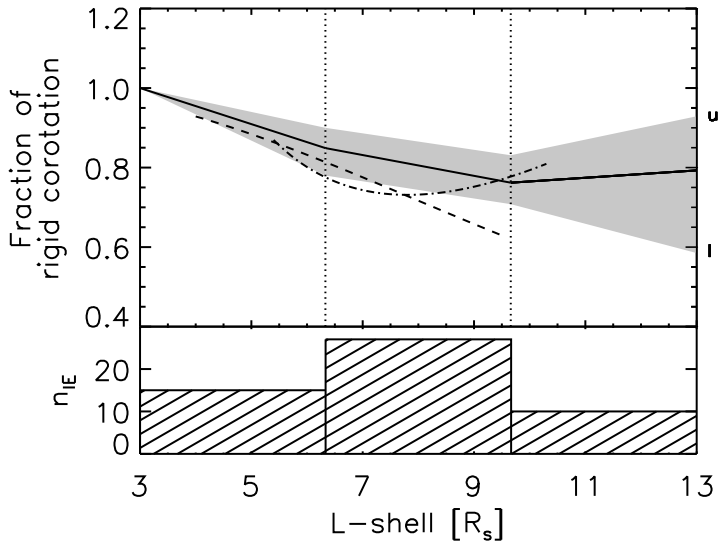

Figure 4.5: Top: Model of the azimuthal plasma flow in the Kronian magnetosphere, with error range included (grey), (u) upper angular velocity profile, (l) lower angular velocity profile. The dashed line represents the model by Mauk et al. (2005), the dashed-dotted line is the result of the moment calculation made by Wilson et al. (2008). Bottom: Number of observed injections inside different *L*-shell range bins.

Radial distance at equator [R_S]	Corotation [%]
3.0	100
6.3	85
9.6	76
13.0	79

Table 4.1: Radial distance and corotation, derived by the analysis of our dataset of injections.

4.4.1 Comparison and conclusions

Results of our computations and comparison with the model of Mauk et al. (2005) (dashed) and moment calculations made by Wilson et al. (2008) (dashed-dotted) are shown in Figure 4.5. For the innermost part of the magnetosphere up to 7 R_S, values of Mauk et al. (2005) are within our error range. By analysing 2 ion and 3 electron injections, they applied the same method of analysis and showed that the magnetosphere does not rigidly corotate but subcorotates. Outside 7 R_S their profile deviates from ours since the Mauk et al. (2005) profile does not allow recovery of the magnetospheric speed from local mass loading. Our velocity model is applicable in a broader region than those of Mauk et al. (2005) (3.9 R_S - 9 R_S).
The results of a moment calculation made by Wilson et al. (2008) and based on CAPS

measurements of the cold plasma show a minimum in the angular velocity at 7.8 R_S with 73 % of rigid corotation. Further outward, the velocity increases and reaches a value of about 80 % at a distance of 10.3 R_S. In Wilson et al. (2009), the authors extended the angular velocity profile from 5.5 R_S to 3 R_S. At 5.5 R_S the magnetosphere rotates with 84 % of rigid corotation. Further inward, the profile again shows a dip at the orbital distance of Enceladus with a rotation speed smaller than 80 %. Due to our *L*-shell binning, we are not able to resolve this in our plasma flow model. Our assumption that the magnetosphere rigidly corotates at 3 R_S is confirmed by the Wilson et al. (2009) model.

Radial distance at equator [R_S]	Corotation [%] (Mauk et al. 2005)	Corotation [%] (Wilson et al. 2009)
3.00	95	99.9
6.25	81	80.4
9.50	62	78.4

Table 4.2: Radial distance and corotation of Mauk et al. (2005), Wilson et al. (2009).

The plasma convection speed from INCA anisotropies obtained by Kane et al. (2008) was applied to the region between 13 R_S and 36 R_S. Due to radial distance coverage, it perfectly affiliates to our model. It shows corotation at distances between 13 R_S to 20 R_S. This corresponds to our upper velocity profile (u) in Fig. 4.5. The Kane et al. (2008) profile shows a more or less constant azimuthal plasma velocity of 170 km s^{-1} at distances up to 36 R_S. This is much further out than we measure any injection events, and therefore our method is not applicable in this region.
Our angular velocity model also shows a slightly positive gradient between 9.6 R_S and 13 R_S, which is not only in agreement with Wilson et al. (2009) but also with the measurements formerly made by the two Voyager spacecrafts (Richardson and Sittler Jr. 1990).
Saur et al. (2004) suggested and analysed three different mechanisms which can cause deviation from full corotation: radial plasma flow in the magnetosphere, collisions/charge exchange of the ions with neutrals, and ionization of neutrals (pickup). They demonstrated that the breakdown of corotation in the inner and middle magnetosphere is due to the neutrals in Saturn's magnetosphere. Only the latter two mechanisms can generate an azimuthal angular velocity profile, that increases again with radial distance. Another possible mechanism to cause the corotation lag to decrease, is that the ionospheric conductivity could become larger, so that the ionosphere-magnetosphere coupling becomes stronger (Pontius 1997).
Our velocity profile and in particular the slight increase of the angular velocity at radial distances between 9 R_S and 13 R_S are consistent with the idea that the breakdown of corotation inside this region is due to the large amount of neutrals in Saturn's magnetosphere. The neutral gas torus has a peak column density at around 4 R_S (Enceladus' orbit) of about 10^{14} molecules cm^{-2} and decreases to 10^{11} molecules cm^{-2} at L = 10 R_S, as presented by Johnson et al. (2006). The decrease of the neutral density is related to ion mass loss processes such as dissociative recombination. Since the density is decreasing, also the interaction between the neutrals and plasma is decreasing and the angular velocity of the magnetosphere is able to recover to rigid corotation due to the coupling of Saturn's magnetosphere to its ionosphere.

4.5 Injection site and ages

Knowledge of the angular velocity of the background plasma and the age of the injection events (see Fig. 4.6) enables us to trace back these events to the place where the hot plasma has been injected into the inner magnetosphere. The injection sites can give hints about the generation processes of the energetic particle injections. Results of these calculations are shown in Fig. 4.7. We divide the local time into four sectors. On the top panel of Figure 4.7 the locations of the measurements of the injections are displayed. The back traced injection site, based on the calculation of the injection age and azimuthal velocity, are shown in the bottom panel. The observations are highly biased by the trajectory of the spacecraft. Most of the injection events were detected in the LT day sector from 9:00 LT - 15:00 LT.

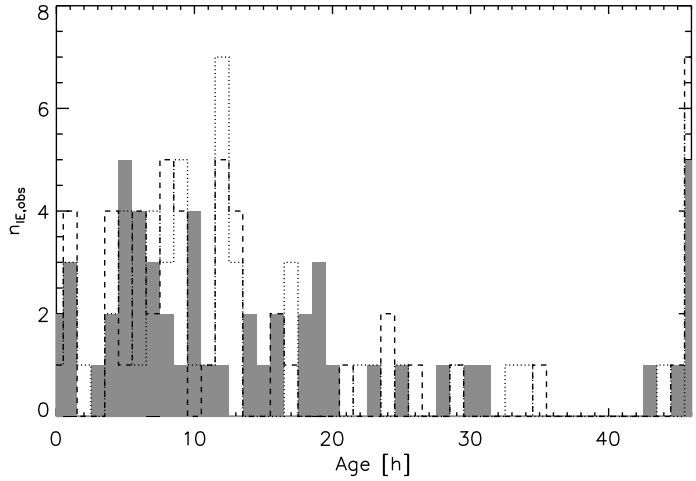

Figure 4.6: Statistical distribution of the ages of the 52 injection events. Filled grey: ages for injection events for the calculated angular velocity profile, dashed line: upper angular velocity profile (profile (u) in Fig. 4.5), dotted line: lower angular velocity profile (profile (l) in Fig. 4.5).

We assume that the occurence of hot plasma injections are LT independent and therefore, the LT dependency in the upper panel of Fig. 4.7 is only attributed to observational bias. Even if the injection site of injections exhibits a LT dependency, the hot plasma is expected to be measured evenly at all local times since they show a huge variety in ages (see Fig. 4.6). For this reason, the number of measured injections was first averaged for all LT bins. We then calculated the weighting factor ξ based on the averaging

$$\xi = \overline{n}/n_{LT}$$

where $\overline{n}$ is the LT average, and n_{LT} the total number of measured injections per bin. The number of back traced injection events was then multiplied with the weighting factor ξ. Without the weighting, the four sectors are more or less equally populated with injections with a slight preference of the morning sector, going from 3 LT to 9 LT. Taking into

account the non-equally distributed measurements, the pattern changes dramatically. The night (21 LT to 3 LT) and the morning sectors (3 LT to 9 LT) are clearly preferred by injections, whereas in the day sector from 9 LT to 15 LT just 10 % of the hot plasma was injected.

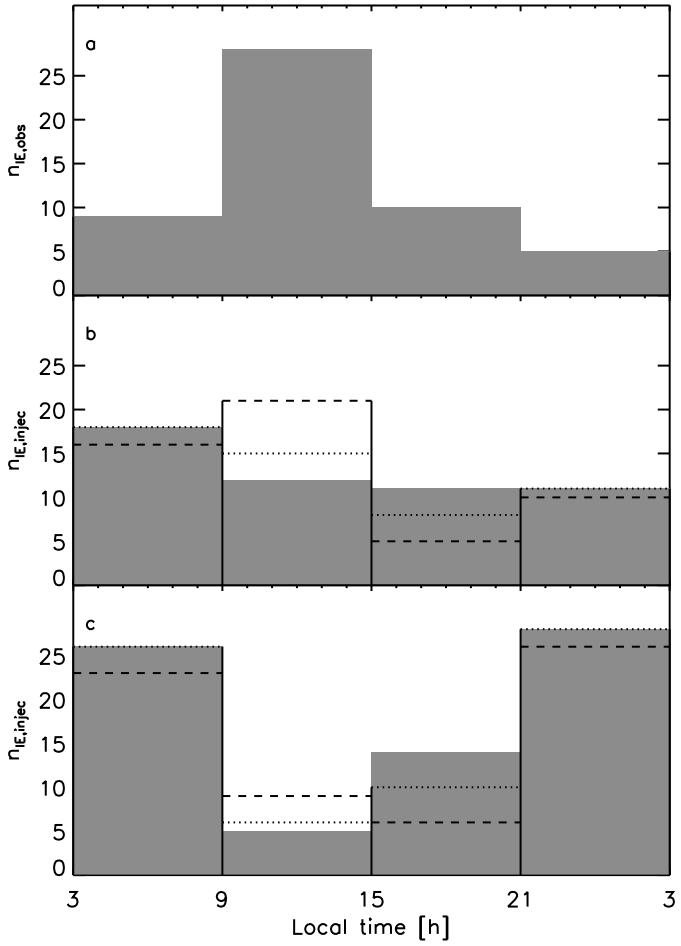

Figure 4.7: Statistical distribution of the number of injection events as a function of the Saturnian local time: (a): distribution of the locations of the measured injections, (b) filled grey: distribution of the origin of the injection site for the calculated angular velocity profile, dashed line: distribution for angular profile (u) in Fig. 4.5, dotted line: distribution for angular profile (l) in Fig. 4.5, (c) weighted distribution of the origin of the injection site for the calculated angular velocity profile, dashed line: distribution for angular profile (u) in Fig. 4.5, dotted line: distribution for angular profile (l) in Fig. 4.5.

40 % of the analysed injections are younger than 10 hours, 33 % have ages between 10 and 20 hours and 27 % are older than 20 hours. The injections that are older than 10 hours (60 %) have survived more than one rotation of the planet (10.53 hours). The ones which are older than 20 hours have survived even two or more rotations.

Age [h]	Percentage
0-10	40
10-20	33
> 20	27

Table 4.3: Percentage of different ages of injection events.

4.5.1 Comparison and conclusions

Chen and Hill (2008) obtained a clustering of injections in the morning sector between 4:00 LT and 12:00 LT, which is shifted to later local times with respect to our results. For their statistical analysis they predefined the velocity profile of Wilson et al. (2008) and did not take into account the trajectory of Cassini. The majority of their analysed injections in the energy range of a few 100 eV to 20 keV are younger than 3 hours. These low energetic plasma clouds are much more short-living than the higher energetic particles MIMI/LEMMS is measuring.
As shown in Mitchell et al. (2009), the large scale injections light up in the midnight to dawn sector, see Fig. 1.13. This behaviour of injections is also revealed in aur data. Unfortunately it is not possible to measure the large scale plasma clouds of Mitchell et al. (2009) simultaneous to our in-situ injections. Either the injections represent the identical feature, or they are somehow related. Possibly the large scale injections trigger small scale injections that can be detected in-situ. In subsection 5.2.1 we analysed the intensity ϵ and spectral index κ. These observations give additional hints, that in any way the large scale injections are somehow correlated with our injection events.

5 Properties of injection events

5.1 Pitch angle distribution of injections

Pitch angle distributions can give hints about the transport processes in the magnetosphere. Rymer et al. (2008) have shown how PADs change during radial adiabatic transport (see section 2.4).

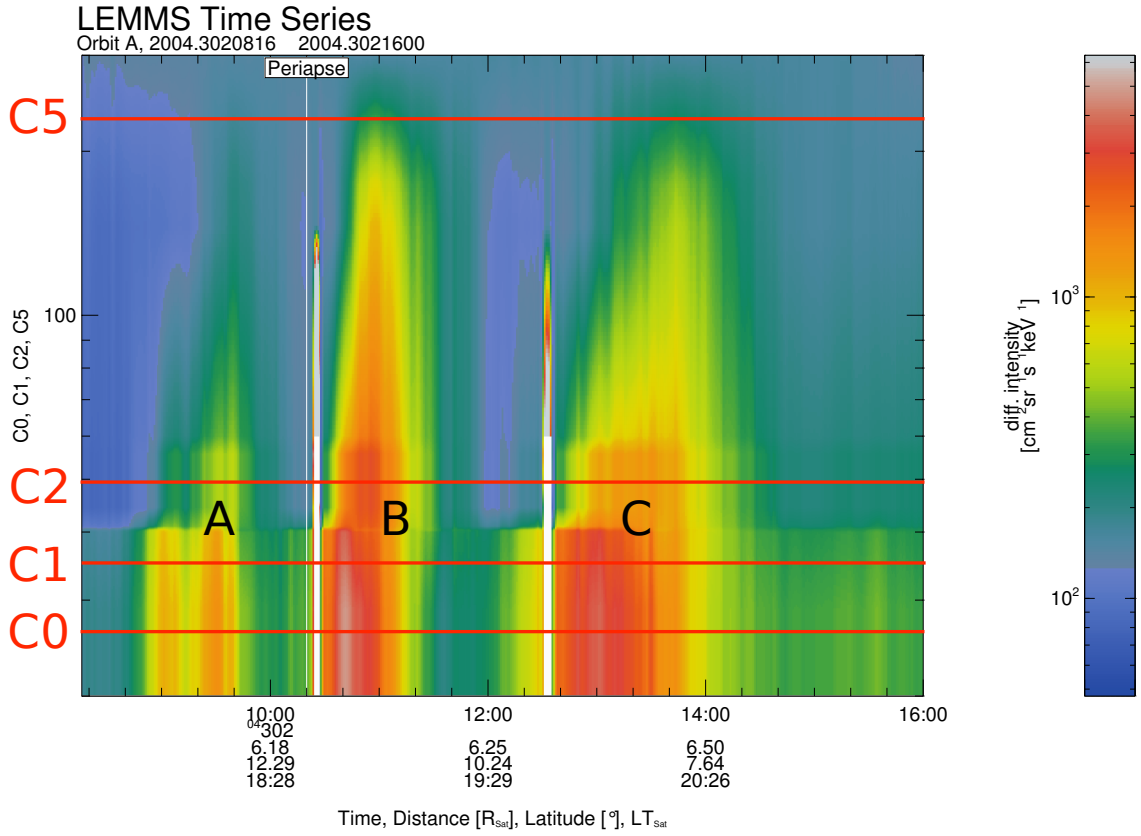

Figure 5.1: Energy time spectrogram of 2004/302. Three injections are labelled with (A), (B), and (C). Marked with red lines are the mean energy of the four different energy channels for which we analysed the PADs.

Since the LEMMS detector head stopped rotating early in 2005, our dataset with good pitch angle coverage is very limited. We analyse three injection events in year 2004, DOY 302. These three injections are shown in the energy-time spectrogram in Fig. 5.1. The

PADs of the three injection events look very similar for all the injections. We therefore show event (A) as a representative example. Fig. 5.2 shows the corresponding intensity-line plot, where the times before, inside, and after the injection event, for which we create PAD plots, are marked in green.

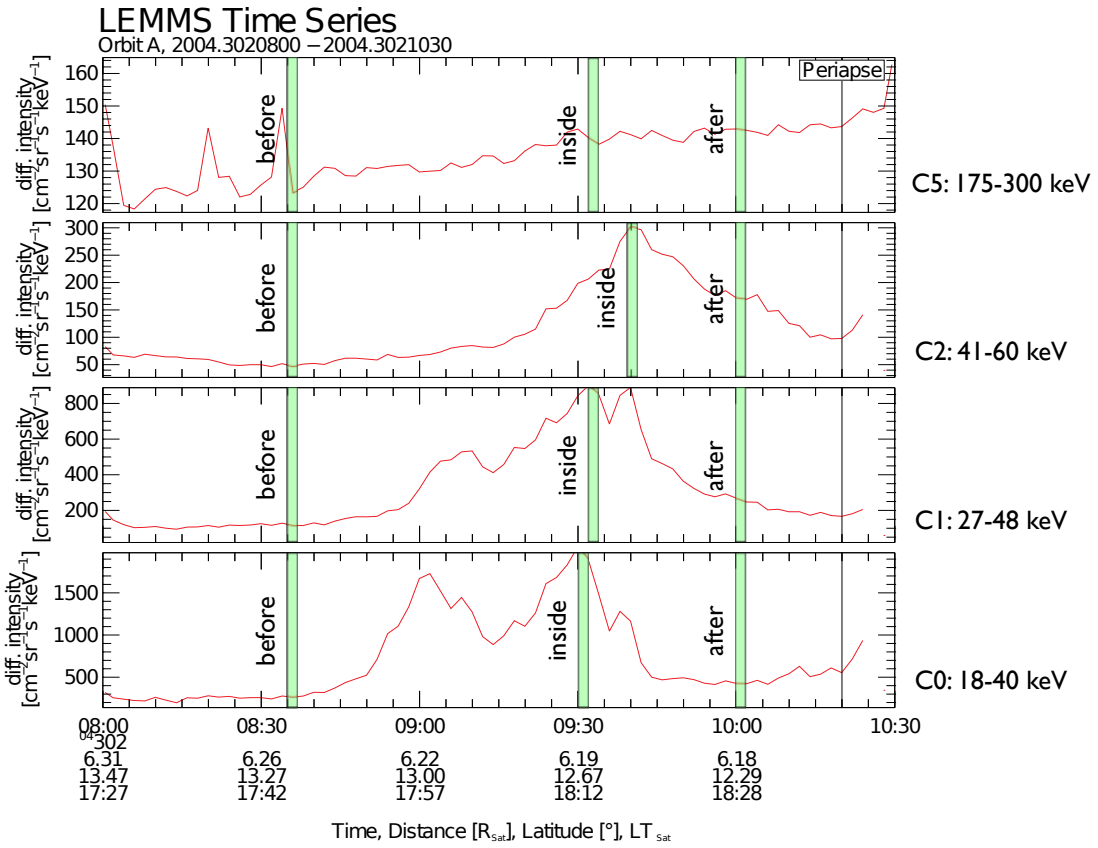

Figure 5.2: Pitch angle averaged differential intensity line plot of 2004/302, injection (A) of the four different energy channels.

In Fig 5.3 we show data fits of PADs for the four different energies. The datapoints were fit to the function

$$c_{fit} = a + b(\sin\alpha) \tag{5.1}$$

The size of the error bars is calculated as

$$\sigma = \left(\frac{1}{k-1} \sum_{n=1}^{k} \left(c_{obs,n} - c_{fit,n} \right)^2 \right)^{1/2} \tag{5.2}$$

where k is the number of data points, c_{obs} the observed count rates and c_{fit} the fit of the observed count rates, according to (5.1). The time intervals inside the injection are chosen where the fluxes of the energy channels show their maximum (see Fig. 5.2).
C0 shows a slightly steeper and narrower pancake distribution inside the injection than before and after. None of the energy channels C0, C1, or C2 show any significant change

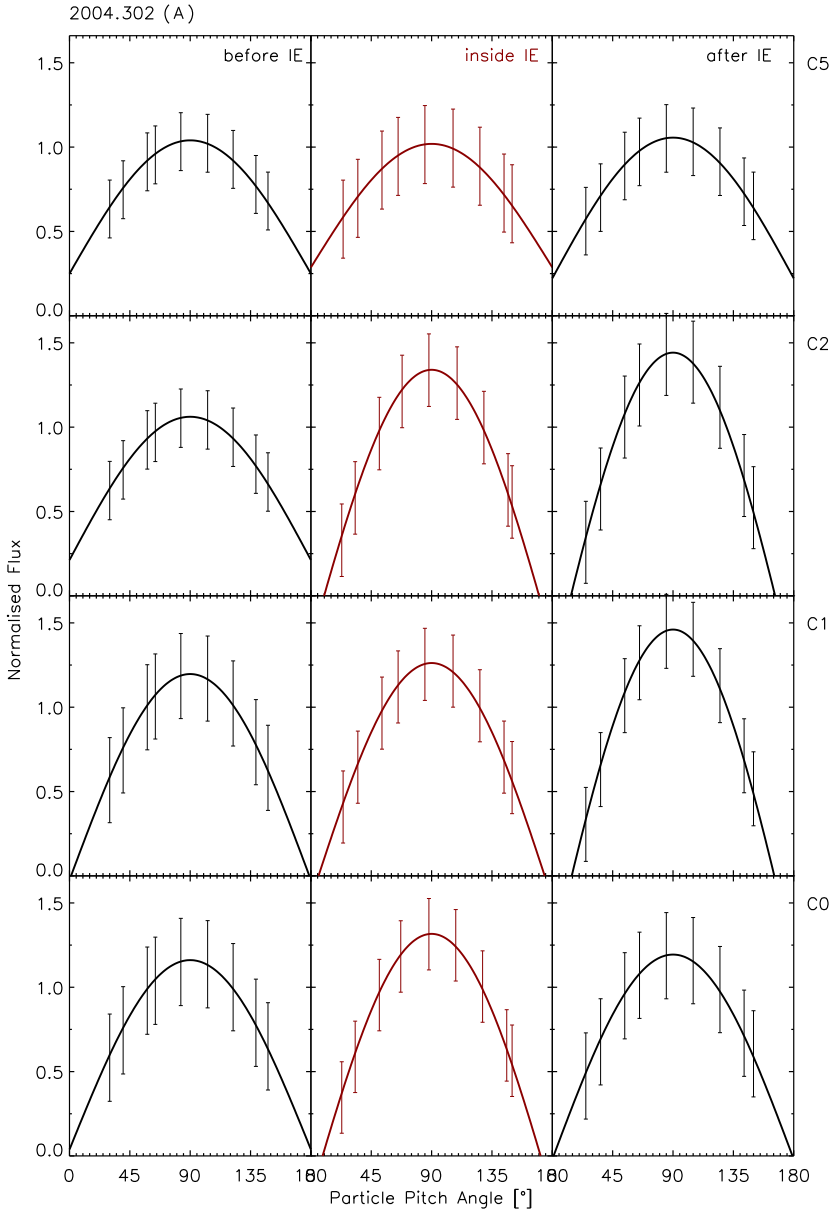

Figure 5.3: Local pitch angle distribution of injection (A) for the marked times before, inside, and after injection of Fig. 5.2 for the energy channels C0 - C2, and C5. The flux has been normalized to the integral of the local pitch angle.

during the passing of the intensity maxima. C1 and C2 show a faint tendency to a steeper and narrower distribution throughout the whole time interval. In C5, no injection signature shows up in the line plot and there is also no change visible in the PAD.

5.1.1 Conclusions

Rymer et al. (2007, 2008, 2009) studied properties of injection events such as the pitch angle distribution (PAD) in the low energy range, see Fig. 1.14. By numerical calculations of PADs, the authors found that the injections originate from a radial distance of about 11 R_S which is consistent with our observations that injections are detected inside of approximately 13 R_S.
Our conceptual view of an injection event is illustrated in Fig. 5.4. Plasma inside a magnetic flux tube is exposed to the magnetic field B_o, that is the same as the magnetic field outside the flux tube. The plasma is then transported radially inward from L_2 to L_1. Due to the transport to increasing magnetic field, the plasma is adiabatically heated. The magnetic moment μ is defined as the energy of a particle, divided by the magnetic field, see (2.18). If the plasma is transported to stronger magnetic field, the energy has to increase to keep μ conserved.

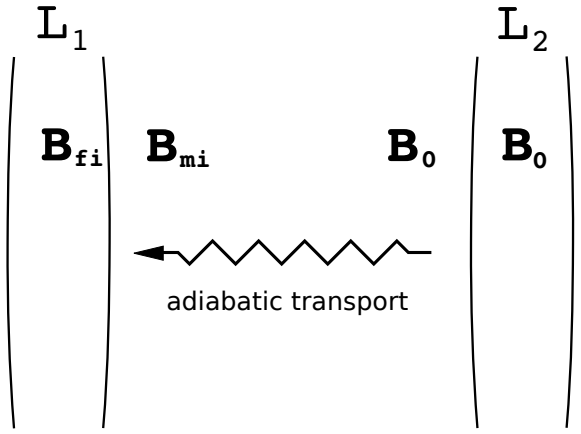

Figure 5.4: Sketch of the magnetic field change during radial plasma transport due to energetic injection events. In the outer magnetosphere, the magnetic field inside and outside the flux tube has the same value and is identified with B_o. B_o corresponds to the magnetic field before the injection initiation. $\mathbf{B}_{fi}$ is the field inside the flux tube (f) in the inner magnetosphere (i), and $\mathbf{B}_{mi}$ is the magnetic field outside the fluxtube (m) in the inner magnetosphere (i). The plasma is radially transported from L_2 to L_1, with $L_1 < L_2$.

Since for the energy range, for which we have analysed the data, the magnetic curvature and gradient drifts do play a significant role (see section 4.1), particles drift out of the inward moving magnetic flux tube. Therefore, they no longer experience the magnetic field inside the flux tube $\mathbf{B}_{fi}$ but the dipole background magnetic field $\mathbf{B}_{mi}$, with $\mathbf{B}_{fi} > \mathbf{B}_{mi}$. This means that the particles are effectively transported from $\mathbf{B}_o$ to $\mathbf{B}_{mi}$.
Unlike to our observations, the PADs in the lower energy range, analysed by Rymer et al. (2008), show a different behaviour, see Fig. 1.14. As their energy range is significant lower than ours, the particles have not yet drifted out of the flux tube and therefore the particles still experience the flux tube magnetic field $\mathbf{B}_{fi}$.
The change in the PAD of the injection plasma population after adiabatic transport is only determined by the final magnetic field (i.e. $\mathbf{B}_{mi}$ or $\mathbf{B}_{fi}$). It is independent on the details of the transport process. There are two fundamental radial plasma transport processes:

injection events and diffusion.
Radial diffusion occurs if the third adiabatic invariant is violated. This is commonly the case in planetary magnetospheres. It can be caused by magnetic fluctuations or by fluctuating electric potential fields (Walt 2005). If the perturbations are on drift timescales, they disturb the drift motion in such a way that the particles perform a radial motion. For particles with large equatorial pitch angles α_{eq}, the magnetic perturbations are most effective. These kind of particles are most affected by radial diffusion processes.
In absence of injection events, the energetic particles are transported via radial diffusion. When transported from L_2 to L_1, the magnetic field exposed on the particles changes from $\mathbf{B}_o$ to $\mathbf{B}_{mi}$. This is the same effective change in $\mathbf{B}$ than in case of an injection in our energy range. Since the change of the PAD only depends on the change in $\mathbf{B}$, there is no difference between the PAD outside the injection (created via radial diffusion) and the PAD inside the injection (created while the injection was driving the particles inward). This is different for the injections at lower energies as described in Rymer et al. (2008). The two final magnetic fields differ, and therefore, there is a significant difference between the PADs after injection and diffusive transport.
The fact that Fig. 5.3 does not show a significant change in the PAD supports the concept that injections and diffusion act adiabatically and that none of the processes has significant non-adiabatic contributions. Such contributions could arise due to loss processes such as pitch angle scattering to the loss cone, to the neutral gas cloud, and to the E-ring torus. We conclude that if loss processes nevertheless play a role for electrons in our energy range, their associated lifetime has to be much larger than the typical time in which the electrons are transported from L_2 to L_1.

5.2 Intensity and spectral index

To obtain the spectrum of an injection event, we followed the injection in time. Usually the energy spectrum is given for one time t. In the case of injections, it is a function of the time. For each energy channels E_n we searched for the maxima in the count rates c_n and obtained the corresponding time t_n, see black dots in Fig. 5.6. To obtain the spectrum of the injection events, we then converted the count rates c_n of the different PHA channels to intensities I_n

$$I_n = \frac{c_n}{\Delta E \cdot G}$$

with ΔE the energy passband and G the geometric factor of the energy channels. We then plotted the intensities I_n as a function of energy E_n and maintained the spectral intensity. For the high energy portion of the injections with $E > 36$ keV, we could fit the spectrum with a power law of the form

$$I = I_0 \cdot E^{-\kappa} \tag{5.3}$$

which is shown exemplarily in Fig. 5.5. For some of the injections, the intensity decreased to lower energies, so we concentrated on the high energy portion of the injections. Some of the injections could not be fit to power law so our data set reduced to 34 injections

that we could analyse. If both, the intensities I and energy E are plotted on a logarithmic scale, the power law can be fit by a straight line of the form

$$\log I = \log I_0 - \kappa \log \frac{E}{E_0} \tag{5.4}$$

where κ is the slope and represents the spectral index, see Fig. 5.5.

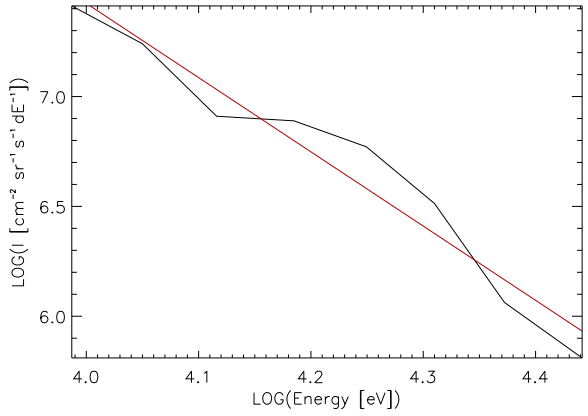

Figure 5.5: Fit of the energy spectra of an injection on day 2006/285. The energy and the intensity are both shown on a logarithmic scale.

Fig. 5.6 shows the corresponding energy time spectrogram of day 2006/285. Since this injection events shows up at high energies with $E > 36$ keV, we could use the whole energy range of the injection for the spectral fit.

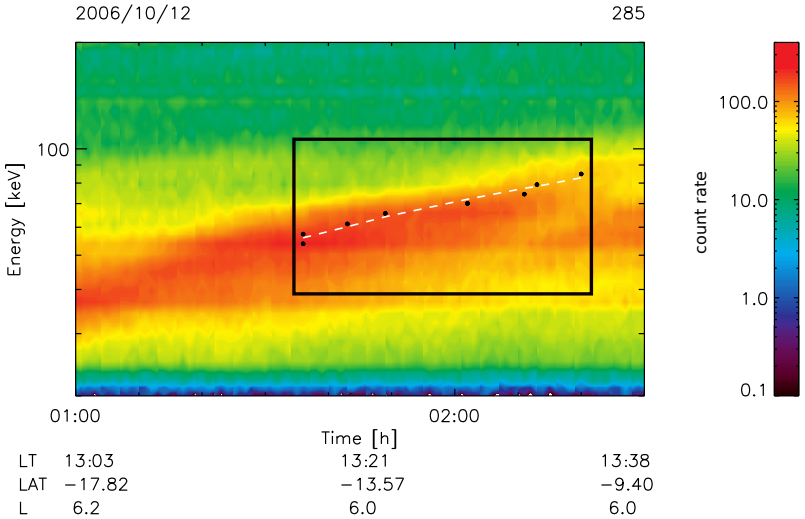

Figure 5.6: Energy time spectrogram of injection event on day 2006/285. The black dots represent the count rate maxima of the different PHA channels, the dashed white line is the fit to the data to obtain $E(t)$ with equidistant time steps.

5.2.1 Observations and conclusions

In the following we show plots of the total intensity ϵ and spectral index κ as a function of the

- L-shell (Fig. 5.7),
- local time of injection site (Fig. 5.8),
- latitude (Fig. 5.10), and
- injection age (Fig. 5.11).

The total intensity ϵ of an injection event is defined as

$$\epsilon = \int_{E_1}^{E_2} I \, \mathrm{d}E \tag{5.5}$$

with E_1 being the lowest and E_2 the highest energy of an injection, see Figs. 5.5 and 5.6. We find that ϵ may show two maxima at $L \approx 9$ R_S and at $L \approx 5$ R_S. Due to the small amount of data points, these maxima are perhaps not meaningful and have to be regarded with care. The values for κ do not show any maxima or minima, see Fig. 5.7.

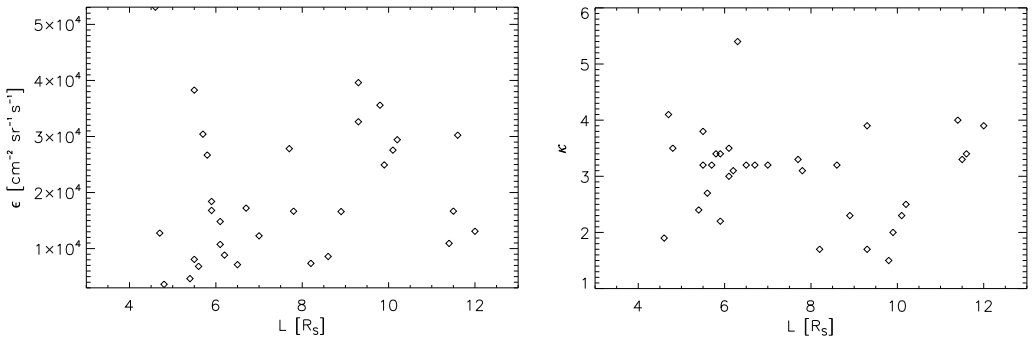

Figure 5.7: ϵ (left hand side) and κ (right hand side) as a function of L-shell. Black diamonds represent the data.

Even though we have analysed a small number of injections, the position of our observed maxima correspond very well with the plasma boundaries described in section 1.2.3. Persoon et al. (2009) identified an electron total density maximum near the orbit of Enceladus at around 4 R_S, which is in agreement with findings of Smith et al. (2010). The density is dominated by small energies. The authors found a maximum pick-up ion source rate at 4 R_S, which also implies a maximum in electron density, due to quasi-neutrality of the magnetospheric plasma. At the radial distance of 9 R_S Schippers et al. (2008) identified a plasma boundary where the density of suprathermal electrons reaches a maximum.
These two density peaks of the background plasma correspond very well with our observations of injection intensities. We therefore conclude that the peak intensities of injections are caused by background plasma intensity peaks rather than being an injection event characteristic. Our finding of the two intensity peaks at $L \approx 5$ R_S and $L \approx 9$ R_S are

also revealed in the data of Paranicas et al. (2010). The authors have averaged the energies between 41 KeV and 60 keV over the time intervall from day 2004/182 to day 2010/155. Since they averaged all the intensities for this energy range, also our analysed injections as well as the injection events we did not consider in our studies are included in the average values. This also shows up in the coincidence with the local time asymmetry. The maximum energy of the injections we have analysed is between 70 keV and 100 keV. The minimum energy that was included in the study of Carbary et al. (2009) is 110 keV. Even though this energy is slightly higher than the energies of our injections, the two peaks in radial distance as well as the local time asymmetry shows up in their averages taken for the time interval from mid 2004 to late 2008.
The intensity ϵ has higher values on the morning sector from 00:00 LT to 12:00 LT than on the evening sector, going from 12:00 LT to 24:00 LT. κ shows the opposite behaviour: lower values in the morning than in the evening sector. The injections coming from the morning sector have higher intensities ϵ and since κ is smaller, more high energetic particles contribute to the intensity than to the injections coming from the evening sector.

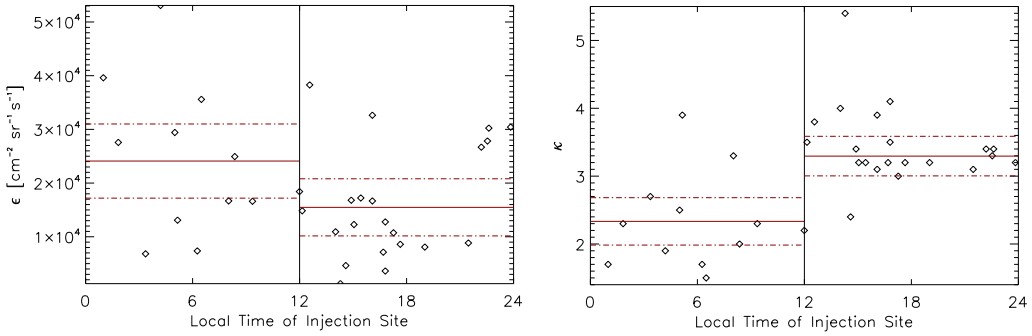

Figure 5.8: ϵ (left hand side) and κ (right hand side) as a function of local time of injection site. The red solid line represents the average value for the two LT sectors, the dotted-dashed line is the standart deviation. For ϵ the distributions shows higher values in the morning sector (around 6:00 LT) than in the evening sector (around 18:00 LT). For κ we find lower values in the morning than in the evening sector.

Mitchell et al. (2009) have shown that the large scale plasma injections detected by INCA with remote sensing, lighten up in the midnight to dawn quadrant. To clarify the injection topology we have marked in Fig. 5.9 the different injection regions. In orange we indicate the region that Mitchell et al. (2009) identified as the injection region associated with depolarization due to reconnection processes in the magnetosphere. In yellow we assigned the region with low ϵ and high κ whereas the region in red represents the sector with high ϵ and low κ injections.
In our conceptual view of injections, there are more than one generation process active in the magnetosphere. Injections due to the centrifugal interchange instability can be injected at any local time, with no preference of any LT sector. In contrast to that, injections due to reconnection in the magnetotail are injected mostly in the midnight to dawn sector. In our dataset we could identify two subclasses of injections. The injections with low intensities ($\epsilon < 2 \cdot 10^4$) and high spectral index ($\kappa > 2.8$) occur mostly on the noon to midnight sector from 12:00 LT to 24:00 LT. The high intensity ($\epsilon > 2 \cdot 10^4$) and low

κ (< 2.8) injections occur mainly between 24:00 LT and 12:00 LT. We associate these injection with reconnection processes occurring along the Vasyliunas- and Dungey-cycle X-line, see also Fig. 1.8, and compare with Mitchell et al. (2009). It is not clear if the large-scale injections are identical with our in-situ measured injections. The large-scale injections are less frequent, that is also revealed in our observations.

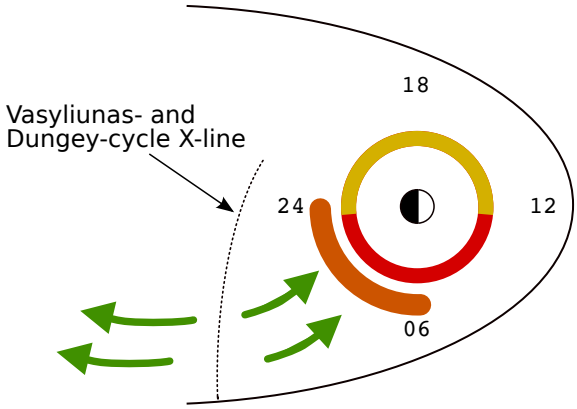

Figure 5.9: Sketch of plasma injection topology at Saturn. Green arrows indicate plasma blobs moving towards the magnetotail as well as injections travelling towards the planet. The orange area marks the region where Mitchell et al. (2009) observed enhanced ENA emission. In red is the region where we observe injections with $\epsilon > 2 \cdot 10^4$, in yellow with $\epsilon < 2 \cdot 10^4$. Numbers represent the LT.

Fig. 5.10 shows ϵ and κ as a function of the absolute value of the latitude. Ignoring the sign of the latitude improves the statistics. It is a valid approach, since the magnetic field, and therefore the bounce motion is mirror symmetric to the equatorial plane. Deviations from this only occur at larger distances, where the current sheet is significantly warping (Arridge et al. 2008). The intensity ϵ as well as the spectral index κ show the highest values near the equator and decrease to higher/lower latitudes, see Fig. 5.10. To emphasize this behaviour, we overplotted the envelope on the data in the shape of a triangle. As displayed in Figure 5.10, the intensity ϵ as well as the spectral index κ covers a large range of values. The envelope of their values is highest near the equator and decreases to higher/lower latitudes. This distribution is consistent with a pancake pitch angle distribution of the injections. Single injections of our dataset are often observed within a small range of pitch angles. Depending upon this pitch angle range, LEMMS measures intensities between the maximum of the PAD and the minimum. This yields the scattering of the intensities. As can be seen in Fig. 2.6, the maximum of a pancake PAD decreases with increasing latitude. This yields the decreasing envelope. If the typical PAD of the injections would be field aligned, the maximum value would stay constant even at high latitudes. Figure 5.10 is an indirect approach to derive the approximate shape of the PADs of injection events. In contrast to Figure 5.3, where the PAD of a single injection is exemplarily shown, it yields that at least a large fraction of the considered injections are indeed following the exemplarily shown PAD.

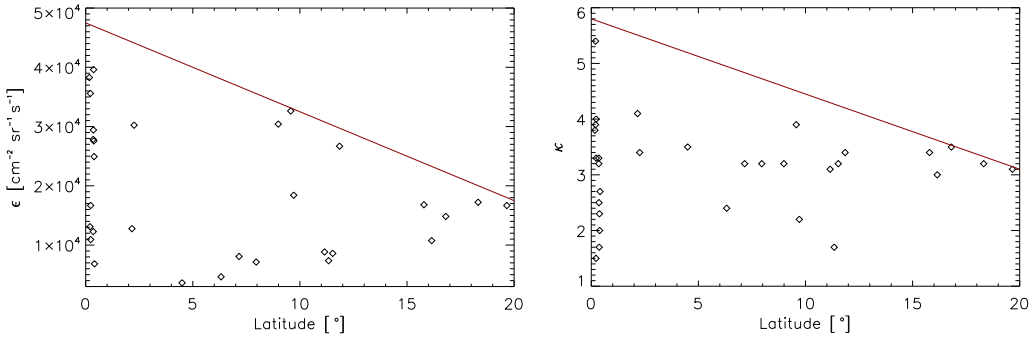

Figure 5.10: ϵ (left hand side) and κ (right hand side) as a function of latitude. There is a tendency for higher values for both, ϵ and κ for lower values of the latitude λ.

For the intensity as a function of age, we could fit the data with an exponential decay of the form

$$\epsilon_{fit}(T_A) = \epsilon_0 \cdot e^{(T_A/\tau)} \tag{5.6}$$

with T_A the age of the injection events and τ the 'lifetime' of the injections. We found a lifetime of $\tau = 21$ h, which is in agreement with Fig. 4.6, where the majority of the injections are younger than 21 h. Paranicas et al. (2010) argues that electrons are most likely to be lost to the neutral gas cloud than to the ring. Cassidy and Johnson (2010) have shown that the total neutral gas densities become significant for distances lower than 8 R_S. Paranicas et al. (2010) calculated the energy loss of a 30 keV electron for 1 keV to 90 h. To get lost to energies that are not observable for LEMMS ($E < 20$ keV) this lifetime is two to three orders of magnitude higher than the lifetime we have observed for injections. Therefore this energy loss can not be the dominant process for electrons in our observed energy range. Loss processes are equally effective for high energies as well as low energies of our observed energy range, indicated by the slope of the first order polynomial fit of κ as a function of the age of the injection events.

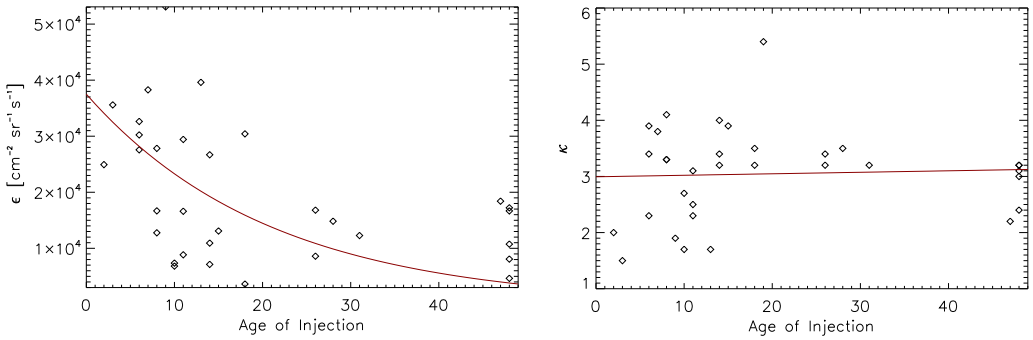

Figure 5.11: ϵ (left hand side) and κ (right hand side) as a function of injection age. For ϵ we fit the data to an exponential decay (red solid line). The intensity decreases with proceeding age. The first order polynomial fit of κ shows no dependency with increasing age.

6 Conclusions and outlook

This thesis deals with the study of energetic particle injection events in Saturn's magnetosphere. It describes properties of the events themselves and uses them as a tool to characterize aspects of the global configuration of the magnetosphere.
The focus of this work is on electron injections in the energy range between several 10 keV and several 100 keV. The covered time period is between mid 2004 and late 2007. Our data is based on a carefully selected set of 52 injection events that show exceptionally clear signatures. For parts of the analysis, the dataset was even more filtered with respect to spectral shape.
A simulation of the electron motion in the magnetosphere has been used to qualitatively understand the formation of inverted and regular dispersion profiles of the injections. For this, knowledge about the known electron drifts was combined with an assumption of the angular corotation velocity of the magnetosphere and spacecraft trajectories. It could be shown that the used physics can reproduce the observations if the corotation is not rigid (Fig. 4.2). For a more quantitative approach, a relation between the measured slope of the dispersed profile, the azimuthal velocity profile and the injection age was used. The results show that the magnetosphere is indeed subcorotating, with a minimum value of $\approx 80\%$ of rigid corotation at $L \approx 10\ \mathrm{R_S}$.
The relation mentioned above has also been used to derive the age of the observed injections (Fig. 4.6). Most of them are younger than one rotation period of Saturn. Besides counting the appearance of injections of different ages, it is also possible to study how the overall intensity of the injections is decreasing with time. An analysis shows that the intensity decreases to $1/e$ of the initial value after about 21 h (Fig. 5.11).
The rate of this decay yields information about its mechanism. If the electrons would be lost due to deceleration within the neutral torus or the E-ring, the decay should occur on much larger timescales. Therefore, it has to be another process. A probable candidate for this is diffusion, which causes that the particles redistribute in space and therefore escape the measurement.
Knowledge of the age of the injections can, together with the azimuthal velocity profile, being used to determine the local time of the origin of the injections. The results show that most injections occur on the nightside of the planet, between 21 LT and 9 LT (Fig. 4.7). A large fraction of the injections in this region shows higher intensities than in other parts of the magnetosphere (Fig. 5.9).
These two facts help to infer the mechanism that causes the injections. The region where the most and the most intense injections are observed coincides with the region, where frequently large ENA enhancements are observed. These are thought to be a subclass of injection events that originate from a depolarization. From this fact, it can be concluded that at least the intense injections are somehow related to dipolarization. If they are direct

signature or a secondary effect of this process is still an open question. Beside this, there is also the possibility that some of the observed injections occur due to interchange instabilities.
Another important characteristic of an injection event is its pitch angle distribution. In the considered region of the magnetosphere, usually pancake distributions exist. Injection events typically show the same kind of distribution (Figs. 5.3 and 5.10). This fact can be used to understand the mechanism that drives the particles inward during the initial formation of the injection. The pitch angle distributions are consistent with fully adiabatic transport that conserves the first two adiabatic invariants. If losses occur during the radial motion, they are negligible.
Although it was possible to infer a wealth of knowledge from the described studies of injection events, there are possibilities to refine the results or study other characteristics of the injections. The use of a larger dataset of injections would allow increasing the resolution in L-shell and local time of all the shown results. It could also decrease the scattering, yielding conclusions that are more confident. While this work derived the local time of origin of the injections, it is still an open question from which radial distances they originate. An analysis using phase space densities at constant first and second adiabatic invariant could yield at least lower limits of the origin in radial distance (Thorne et al. 1997, Krupp et al. 2004).

A Appendix

A.1 Constants and variables

$q = 1.6 \cdot 10^{-19}$ C	unit charge
$\mu_0 = 1.257 \cdot 10^{-6}$ Vs Am^{-1}	magnetic permeability
$M = 4.6 \cdot 10^{25}$ Am^2	magnetic moment of Saturn (Hansen et al. 2005)
$R_S = 60,268$ km	radius of Saturn
$\omega = 1.638 \cdot 10^{-4}$ rad sec^{-1}	angular velocity
$m_e = 9.1 \cdot 10^{-31}$ kg	mass of electron
$m_i = 1.67 \cdot 10^{-27}$ kg	mass of ion
ϑ	latitude
B	magnetic field
E	electric field
$v_{\parallel} = \left(\frac{k_B T}{m}\right)^{1/2}$	thermal speed
$v_{\perp} = \omega r$	corotation speed
ϵ	intensity of injections
κ	spectral index of injections

Table A.1: Constants and variables.

A.2 Acronyms

MHD	Magnetohydrodynamics
DOY	Day of year
SOI	Saturn orbit insertion
LT	Local time
MIMI	Magnetospheric Imaging Instrument
LEMMS	Low Energy Magnetosphere Measurement System
LE	Low energy end
HE	High energy end
PHA	Pulse height analyser
CHEMS	Charge-Mass-Energy Spectrometer
INCA	Ion and Neutral Camera
CAPS	Cassini Plasma Spectrometer
EPD	Energetic Charged Particles Detector
MAG	Cassini Magnetometer
ENA	Energetic neutral atoms
PAD	Pitch angle distribution
EFD	Energy flux density
IMF	Interplanetary magnetic field

Table A.2: Acronyms

Bibliography

Akalin, F., Gurnett, D. A., Averkamp, T. F., Persoon, A. M., Santolik, O., Kurth, W. S., Hospodarsky, G. B., 2006, First whistler observed in the magnetosphere of Saturn, Geophys. Res. Lett., 33, 20 107

Akasofu, S., 1964, The development of the auroral substorm, Planet. Space Sci., 12, 273

Arridge, C. S., Russell, C. T., Khurana, K. K., Achilleos, N., André, N., Rymer, A. M., Dougherty, M. K., Coates, A. J., 2007, Mass of Saturn's magnetodisc: Cassini observations, Geophys. Res. Lett., 34, 9108

Arridge, C. S., Khurana, K. K., Russell, C. T., Southwood, D. J., Achilleos, N., Dougherty, M. K., Coates, A. J., Leinweber, H. K., 2008, Warping of Saturn's magnetospheric and magnetotail current sheets, J. Geophys. Res., 113, 8217

Baines, K. H., Drossart, P., Momary, T. W., Formisano, V., Griffith, C., Bellucci, G., Bibring, J. P., Brown, R. H., Buratti, B. J., Capaccioni, F., Cerroni, P., Clark, R. N., Coradini, A., Combes, M., Cruikshank, D. P., Jaumann, R., Langevin, Y., Matson, D. L., McCord, T. B., Mennella, V., Nelson, R. M., Nicholson, P. D., Sicardy, B., Sotin, C., 2005, The Atmospheres of Saturn and Titan in the Near-Infrared First Results of Cassini/vims, Earth Moon and Planets, 96, 119–147

Baum, W. A., Kreidl, T., Westphal, J. A., Danielson, G. E., Seidelmann, P. K., Pascu, D., Currie, D. G., 1981, Saturn's E ring, Icarus, 47, 84–96

Baumjohann, W., Treumann, R. A., 1996, Basic Space Plasma Physics, Imperial College Press

Bunce, E. J., Arridge, C. S., Clarke, J. T., Coates, A. J., Cowley, S. W. H., Dougherty, M. K., Gérard, J., Grodent, D., Hansen, K. C., Nichols, J. D., Southwood, D. J., Talboys, D. L., 2008, Origin of Saturn's aurora: Simultaneous observations by Cassini and the Hubble Space Telescope, J. Geophys. Res., 113, 9209

Burch, J. L., Goldstein, J., Hill, T. W., Young, D. T., Crary, F. J., Coates, A. J., André, N., Kurth, W. S., Sittler, E. C., 2005, Properties of local plasma injections in Saturn's magnetosphere, Geophys. Res. Lett., 32, 14

Burger, M. H., Sittler, E. C., Johnson, R. E., Smith, H. T., Tucker, O. J., Shematovich, V. I., 2007, Understanding the escape of water from Enceladus, J. Geophys. Res., 112, 6219

Burton, M. E., Buratti, B., Matson, D. L., Lebreton, J., 2001, The Cassini/Huygens Venus and earth flybys: An overview of operations and results, J. Geophys. Res., 106, 30 099–30 108

Carbary, J. F., Mitchell, D. G., Krupp, N., Krimigis, S. M., 2009, L shell distribution of energetic electrons at Saturn, J. Geophys. Res., 114, 9210

Cassidy, T. A., Johnson, R. E., 2010, Collisional spreading of Enceladus' neutral cloud, Icarus, 209, 696–703

Chen, Y., Hill, T. W., 2008, Statistical analysis of injection/dispersion events in Saturn's inner magnetosphere, J. Geophys. Res., 113, 7215

Connerney, J., Davis, L., Chenette, D., 1984, Magnetic field models, in Saturn, (Eds.) T. Gehrels, M. Matthews, pp. 354–377, The University of Arizon Press, Arizon

Cowley, S. W. H., Bunce, E. J., 2003, Corotation-driven magnetosphere-ionosphere coupling currents in Saturn's magnetosphere and their relation to the auroras, Annales Geophysicae, 21, 1691–1707

Deforest, S. E., McIlwain, C. E., 1971, Plasma clouds in the magnetosphere, J. Geophys. Res., 76, 3587–3611

Dessler, A. J., 1983, Physics of the Jovian magnetosphere

Dialynas, K., Krimigis, S. M., Mitchell, D. G., Hamilton, D. C., Krupp, N., Brandt, P. C., 2009, Energetic ion spectral characteristics in the Saturnian magnetosphere using Cassini/MIMI measurements, J. Geophys. Res., 114, 1212

Dougherty, M. K., Khurana, K. K., Neubauer, F. M., Russell, C. T., Saur, J., Leisner, J. S., Burton, M. E., 2006, Identification of a Dynamic Atmosphere at Enceladus with the Cassini Magnetometer, Science, 311, 1406–1409

Dougherty, M. K., Esposito, L. W., Krimigis, S. M., 2009, Saturn from Cassini-Huygens

Gérard, J., Grodent, D., Cowley, S. W. H., Mitchell, D. G., Kurth, W. S., Clarke, J. T., Bunce, E. J., Nichols, J. D., Dougherty, M. K., Crary, F. J., Coates, A. J., 2006, Saturn's auroral morphology and activity during quiet magnetospheric conditions, J. Geophys. Res., 111, 12 210

Gombosi, T. I., Armstrong, T. P., Arridge, C. S., Khurana, K. K., Krimigis, S. M., Krupp, N., Persoon, A. M., Thomsen, M. F., 2009, Saturn's Magnetospheric Configuration, in Saturn from Cassini-Huygens, (Eds.) M. K. Dougherty, L. W. Esposito, S. M. Krimigis, pp. 203–255, Springer

Gurnett, D. A., Bhattacharjee, A., 2005, Introduction to Plasma Physics

Hansen, K. C., Ridley, A. J., Hospodarsky, G. B., Achilleos, N., Dougherty, M. K., Gombosi, T. I., Tóth, G., 2005, Global MHD simulations of Saturn's magnetosphere at the time of Cassini approach, Geophys. Res. Lett., 32, 20

Hill, T. W., Rymer, A. M., Burch, J. L., Crary, F. J., Young, D. T., Thomsen, M. F., Delapp, D., André, N., Coates, A. J., Lewis, G. R., 2005, Evidence for rotationally driven plasma transport in Saturn's magnetosphere, Geophys. Res. Lett., 32, 14

Hillier, J. K., Green, S. F., McBride, N., Schwanethal, J. P., Postberg, F., Srama, R., Kempf, S., Moragas-Klostermeyer, G., McDonnell, J. A. M., Grün, E., 2007, The composition of Saturn's E ring, Mon. Not. R. Astron. Soc., 377, 1588–1596

Hubbard, W. B., Burrows, A., Lunine, J. I., 2002, Theory of Giant Planets, Annu. Rev. Astron. Astr., 40, 103–136

Hurford, T. A., Helfenstein, P., Hoppa, G. V., Greenberg, R., Bills, B. G., 2007, Eruptions arising from tidally controlled periodic openings of rifts on Enceladus, Nature, 447, 292–294

Jackman, C. M., Russell, C. T., Southwood, D. J., Arridge, C. S., Achilleos, N., Dougherty, M. K., 2007, Strong rapid dipolarizations in Saturn's magnetotail: In situ evidence of reconnection, Geophys. Res. Lett., 34, 11 203

Johnson, R. E., Smith, H. T., Tucker, O. J., Liu, M., Burger, M. H., Sittler, E. C., Tokar, R. L., 2006, The Enceladus and OH Tori at Saturn, Astrophys. J., 644, L137–L139

Kane, M., Mitchell, D. G., Carbary, J. F., Krimigis, S. M., Crary, F. J., 2008, Plasma convection in Saturn's outer magnetosphere determined from ions detected by the Cassini INCA experiment, Geophys. Res. Lett., 35, 4102

Khurana, K. K., Russell, C. T., Dougherty, M. K., 2008, Magnetic portraits of Tethys and Rhea, Icarus, 193, 465–474

Kivelson, M. G., Russell, C. T., 1995, Introduction to Space Physics

Krimigis, S. M., Mitchell, D. G., Hamilton, D. C., Livi, S., Dandouras, J., Jaskulek, S., Armstrong, T. P., Boldt, J. D., Cheng, A. F., Gloeckler, G., Hayes, J. R., Hsieh, K. C., Ip, W.-H., Keath, E. P., Kirsch, E., Krupp, N., Lanzerotti, L. J., Lundgren, R., Mauk, B. H., McEntire, R. W., Roelof, E. C., Schlemm, C. E., Tossman, B. E., Wilken, B., Williams, D. J., 2004, Magnetosphere imaging instrument (mimi) on the cassini mission to saturn/titan, Space Sci. Rev., 114, 233–329

Krimigis, S. M., Sergis, N., Mitchell, D. G., Hamilton, D. C., Krupp, N., 2007, A dynamic, rotating ring current around Saturn, Nature, 450, 1050–1053

Krupp, N., Vasyliunas, V. M., Woch, J., Lagg, A., Khurana, K. K., Kivelson, M. K., Mauk, B. H., Roelof, E. C., Williams, D. J., Krimigis, S. M., Kurth, W. S., Frank, L. A., Paterson, W. R., 2004, Dynamics of the Jovian Magnetosphere, in Jupiter - The Planet, Satellites and Magnetosphere, (Eds.) F. Bagenal, T. Dowling, W. McKinnon, pp. 617–638, Cambridge Planetary Science

Krupp, N., Roussos, E., Lagg, A., Woch, J., Müller, A. L., Krimigis, S. M., Mitchell, D. G., Roelof, E. C., Paranicas, C., Carbary, J., Jones, G. H., Hamilton, D. C., Livi, S., Armstrong, T. P., Dougherty, M. K., Sergis, N., 2009, Energetic particles

in Saturn's magnetosphere during the Cassini nominal mission (July 2004-July 2008), Planet. Space Sci., 57, 1754–1768

Mauk, B. H., Williams, D. J., McEntire, R. W., 1997, Energy-time dispersed charged particle signatures of dynamic injections in Jupiter's inner magnetosphere, Geophys. Res. Lett., 24, 2949–2952

Mauk, B. H., Williams, D. J., McEntire, R. W., Khurana, K. K., Roederer, J. G., 1999, Storm-like dynamics of Jupiter's inner and middle magnetosphere, J. Geophys. Res., 104, 22 759–22 778

Mauk, B. H., Saur, J., Mitchell, D. G., Roelof, E. C., Brandt, P. C., Armstrong, T. P., Hamilton, D. C., Krimigis, S. M., Krupp, N., Livi, S. A., Manweiler, J. W., Paranicas, C. P., 2005, Energetic particle injections in Saturn's magnetosphere, Geophys. Res. Lett., 32, L14S05

Mitchell, D. G., Brandt, P. C., Roelof, E. C., Dandouras, J., Krimigis, S. M., Mauk, B. H., Paranicas, C. P., Krupp, N., Hamilton, D. C., Kurth, W. S., Zarka, P., Dougherty, M. K., Bunce, E. J., Shemansky, D. E., 2005, Energetic ion acceleration in Saturn's magnetotail: Substorms at Saturn?, Geophys. Res. Lett., 32, L20S01

Mitchell, D. G., Krimigis, S. M., Paranicas, C., Brandt, P. C., Carbary, J. F., Roelof, E. C., Kurth, W. S., Gurnett, D. A., Clarke, J. T., Nichols, J. D., Gérard, J., Grodent, D. C., Dougherty, M. K., Pryor, W. R., 2009, Recurrent energization of plasma in the midnight-to-dawn quadrant of Saturn's magnetosphere, and its relationship to auroral UV and radio emissions, Planet. Space Sci., 57, 1732–1742

Müller, A. L., 2007, Das azimuthale Geschwindigkeitsprofil der inneren und mittleren Saturnmagnetosphäre, Diplomarbeit, Institute of Geophysics and Meteorology at the Univeristy of Cologne

Müller, A. L., Saur, J., Krupp, N., Roussos, E., Mauk, B. H., Rymer, A. M., Mitchell, D. G., Krimigis, S. M., 2010, Azimuthal plasma flow in the Kronian magnetosphere, J. Geophys. Res., 115, 8203

Paranicas, C., Mitchell, D. G., Roelof, E. C., Mauk, B. H., Krimigis, S. M., Brandt, P. C., Kusterer, M., Turner, F. S., Vandegriff, J., Krupp, N., 2007, Energetic electrons injected into Saturn's neutral gas cloud, Geophys. Res. Lett., 34, 2109

Paranicas, C., Mitchell, D. G., Roussos, E., Kollmann, P., Krupp, N., Müller, A. L., Krimigis, S. M., Turner, F. S., Brandt, P. C., Rymer, A. M., Johnson, R. E., 2010, Transport of energetic electrons into Saturn's inner magnetosphere, J. Geophys. Res., 115, 9214

Persoon, A. M., Gurnett, D. A., Santolik, O., Kurth, W. S., Faden, J. B., Groene, J. B., Lewis, G. R., Coates, A. J., Wilson, R. J., Tokar, R. L., Wahlund, J., Moncuquet, M., 2009, A diffusive equilibrium model for the plasma density in Saturn's magnetosphere, J. Geophys. Res., 114, 4211

Pontius, D. H., 1997, Radial mass transport and rotational dynamics, J. Geophys. Res., 102, 7137–7150

Pontius, D. H., Hill, T. W., 2006, Enceladus: A significant plasma source for Saturn's magnetosphere, J. Geophys. Res., 111, 9214

Pontius, D. H., Hill, T. W., 2009, Plasma mass loading from the extended neutral gas torus of Enceladus as inferred from the observed plasma corotation lag, Geophys. Res. Lett., 36, 23 103

Porco, C. C., Helfenstein, P., Thomas, P. C., Ingersoll, A. P., Wisdom, J., West, R., Neukum, G., Denk, T., Wagner, R., Roatsch, T., Kieffer, S., Turtle, E., McEwen, A., Johnson, T. V., Rathbun, J., Veverka, J., Wilson, D., Perry, J., Spitale, J., Brahic, A., Burns, J. A., Del Genio, A. D., Dones, L., Murray, C. D., Squyres, S., 2006, Cassini Observes the Active South Pole of Enceladus, Science, 311, 1393–1401

Richardson, J. D., Sittler Jr., E. C., 1990, A plasma density model for Saturn based on Voyager observations, J. Geophys. Res., 95, 12 019–12 031

Rodríguez-Martínez, M., Blanco-Cano, X., Russell, C. T., Leisner, J. S., Wilson, R. J., Dougherty, M. K., 2010, Harmonic growth of ion-cyclotron waves in Saturn's magnetosphere, J. Geophys. Res., 115, 9207

Roussos, E., Jones, G. H., Krupp, N., Paranicas, C., Mitchell, D. G., Lagg, A., Woch, J., Motschmann, U., Krimigis, S. M., Dougherty, M. K., 2007, Electron microdiffusion in the Saturnian radiation belts: Cassini MIMI/LEMMS observations of energetic electron absorption by the icy moons, J. Geophys. Res., 112, 6214

Russell, C. T., Jackman, C. M., Wei, H. Y., Bertucci, C., Dougherty, M. K., 2008, Titan's influence on Saturnian substorm occurrence, Geophys. Res. Lett., 35, 12 105

Rymer, A. M., Mauk, B. H., Hill, T. W., Paranicas, C., André, N., Sittler, E. C., Mitchell, D. G., Smith, H. T., Johnson, R. E., Coates, A. J., Young, D. T., Bolton, S. J., Thomsen, M. F., Dougherty, M. K., 2007, Electron sources in Saturn's magnetosphere, J. Geophys. Res., 112, 2201

Rymer, A. M., Mauk, B. H., Hill, T. W., Paranicas, C., Mitchell, D. G., Coates, A. J., Young, D. T., 2008, Electron circulation in Saturn's magnetosphere, J. Geophys. Res., 113, 1201

Rymer, A. M., Mauk, B. H., Hill, T. W., André, N., Mitchell, D. G., Paranicas, C., Young, D. T., Smith, H. T., Persoon, A. M., Menietti, J. D., Hospodarsky, G. B., Coates, A. J., Dougherty, M. K., 2009, Cassini evidence for rapid interchange transport at Saturn, Planet. Space Sci., 57, 1779–1784

Saur, J., Mauk, B. H., Kaßner, A., Neubauer, F. M., 2004, A model for the azimuthal plasma velocity in Saturn's magnetosphere, J. Geophys. Res., 109, 5217

Saur, J., Neubauer, F. M., Connerney, J. E. P., Zarka, P., Kivelson, M. G., 2004, Plasma Interaction of Io with its Plasma Torus, in Jupiter - The Planet, Satellites and Magnetosphere, (Eds.) F. Bagenal, T. Dowling, W. McKinnon, pp. 537–560, Cambridge Planetary Science

Saur, J., Neubauer, F. M., Schilling, N., 2007, Hemisphere coupling in Enceladus' asymmetric plasma interaction, J. Geophys. Res., 112, 11 209

Saur, J., Schilling, N., Neubauer, F. M., Strobel, D. F., Simon, S., Dougherty, M. K., Russell, C. T., Pappalardo, R. T., 2008, Evidence for temporal variability of Enceladus' gas jets: Modeling of Cassini observations, Geophys. Res. Lett., 35, 20 105

Schippers, P., Blanc, M., André, N., Dandouras, I., Lewis, G. R., Gilbert, L. K., Persoon, A. M., Krupp, N., Gurnett, D. A., Coates, A. J., Krimigis, S. M., Young, D. T., Dougherty, M. K., 2008, Multi-instrument analysis of electron populations in Saturn's magnetosphere, Journal of Geophysical Research (Space Physics), 113, 7208

Sergis, N., Krimigis, S. M., Mitchell, D. G., Hamilton, D. C., Krupp, N., Mauk, B. M., Roelof, E. C., Dougherty, M., 2007, Ring current at Saturn: Energetic particle pressure in Saturn's equatorial magnetosphere measured with Cassini/MIMI, Geophys. Res. Lett., 34, 9102

Sittler, E. C., Johnson, R. E., Smith, H. T., Richardson, J. D., Jurac, S., Moore, M., Cooper, J. F., Mauk, B. H., Michael, M., Paranicas, C., Armstrong, T. P., Tsurutani, B., 2006, Energetic nitrogen ions within the inner magnetosphere of Saturn, J. Geophys. Res., 111, 9223

Sittler, E. C., Andre, N., Blanc, M., Burger, M., Johnson, R. E., Coates, A., Rymer, A., Reisenfeld, D., Thomsen, M. F., Persoon, A., Dougherty, M., Smith, H. T., Baragiola, R. A., Hartle, R. E., Chornay, D., Shappirio, M. D., Simpson, D., McComas, D. J., Young, D. T., 2008, Ion and neutral sources and sinks within Saturn's inner magnetosphere: Cassini results, Planet. Space Sci., 56, 3–18

Smith, H. T., Johnson, R. E., Perry, M. E., Mitchell, D. G., McNutt, R. L., Young, D. T., 2010, Enceladus plume variability and the neutral gas densities in Saturn's magnetosphere, J. Geophys. Res., 115, 10 252–+

Southwood, D. J., Kivelson, M. G., 1987, Magnetospheric interchange instability, J. Geophys. Res., 92, 109–116

Spencer, J. R., Pearl, J. C., Segura, M., Flasar, F. M., Mamoutkine, A., Romani, P., Buratti, B. J., Hendrix, A. R., Spilker, L. J., Lopes, R. M. C., 2006, Cassini Encounters Enceladus: Background and the Discovery of a South Polar Hot Spot, Science, 311, 1401–1405

Stanley, S., 2010, A dynamo model for axisymmetrizing Saturn's magnetic field, Geophys. Res. Lett., 37, 5201

Thorne, R. M., Armstrong, T. P., Stone, S., Williams, D. J., McEntire, R. W., Bolton, S. J., Gurnett, D. A., Kivelson, M. G., 1997, Galileo evidence for rapid interchange transport in the Io torus, Geophys. Res. Lett., 24, 2131

Tian, F., Stewart, A. I. F., Toon, O. B., Larsen, K. W., Esposito, L. W., 2007, Monte Carlo simulations of the water vapor plumes on Enceladus, Icarus, 188, 154–161

Tiscareno, M. S., Burns, J. A., Nicholson, P. D., Hedman, M. M., Porco, C. C., 2007, Cassini imaging of Saturn's rings. II. A wavelet technique for analysis of density waves and other radial structure in the rings, Icarus, 189, 14–34, arXiv:astro-ph/0610242

Tokar, R. L., Johnson, R. E., Thomsen, M. F., Delapp, D. M., Baragiola, R. A., Francis, M. F., Reisenfeld, D. B., Fish, B. A., Young, D. T., Crary, F. J., Coates, A. J., Gurnett, D. A., Kurth, W. S., 2005, Cassini observations of the thermal plasma in the vicinity of Saturn's main rings and the F and G rings, Geophys. Res. Lett., 32, 14

Waite, J. H., Cravens, T. E., Ip, W., Kasprzak, W. T., Luhmann, J. G., McNutt, R. L., Niemann, H. B., Yelle, R. V., Mueller-Wodarg, I., Ledvina, S. A., Scherer, S., 2005, Oxygen Ions Observed Near Saturn's A Ring, Science, 307, 1260–1262

Waite, J. H., Combi, M. R., Ip, W., Cravens, T. E., McNutt, R. L., Kasprzak, W., Yelle, R., Luhmann, J., Niemann, H., Gell, D., Magee, B., Fletcher, G., Lunine, J., Tseng, W., 2006, Cassini Ion and Neutral Mass Spectrometer: Enceladus Plume Composition and Structure, Science, 311, 1419–1422

Walt, M., 2005, Introduction to Geomagnetically Trapped Radiation

Wilson, R. J., Tokar, R. L., Henderson, M. G., Hill, T. W., Thomsen, M. F., Pontius, D. H., 2008, Cassini plasma spectrometer thermal ion measurements in Saturn's inner magnetosphere, J. Geophys. Res., 113, A12 218

Wilson, R. J., Tokar, R. L., Henderson, M. G., 2009, Thermal ion flow in Saturn's inner magnetosphere measured by the Cassini plasma spectrometer: A signature of the Enceladus torus?, Geophys. Res. Lett., 36, 23 104

Publications

Refereed Publications:

- **A. L. Müller**, J. Saur, N. Krupp, E. Roussos, B. H. Mauk, A. M. Rymer, D. G. Mitchell, and S. M. Krimigis, Azimuthal plasma flow in the Kronian magnetosphere, *J. Geophys. Res.*, in press, 2010.
- N. Krupp, E. Roussos, A. Lagg, J. Woch, **A. L. Müller**, S. M. Krimigis, D. G. Mitchell, E. C. Roelof, C. Paranicas, J. Carbary, G. H. Jones, D. C. Hamilton, S. Livi, T. P. Armstrong, M. K. Dougherty, N. Sergis, Energetic particles in Saturn's magnetosphere during the Cassini nominal mission (July 2004-July 2008), *Planet. and Space Sci.*, 2009.
- E. Roussos, N. Krupp, C. P. Paranicas, D. G. Mitchell, **A. L. Müller**, P. Kollmann, Z. Bebesi, S. M. Krimigis, and A. J. Coates, Energetic electron microsignatures as tracers of radial flows and dynamics in Saturn's innermost magnetosphere, *J. Geophys. Res.*, 2010.
- C. Paranicas, D. G. Mitchell, E. Roussos, P. Kollmann, N. Krupp, **A. L. Müller**, S. M. Krimigis, F. S. Turner, P. C. Brandt, A. M. Rymer, R. E. Johnson, Transport of energetic electrons into Saturn's inner magnetosphere, *J. Geophys. Res.*, 2010.

Posters and Presentations:

- **A. L. Müller**, J. Saur, N. Krupp, D. G. Mitchell, S. M. Krimigis, and B. H. Mauk, The azimuthal velocity profile of the Kronian magnetosphere, Cassini Project Science Group Meeting, JPL, Pasadena, CA, USA, January 29-31, 2008. (Oral).
- **A. L. Müller**, J. Saur, N. Krupp, D. G. Mitchell, S. M. Krimigis, and B. H. Mauk, Das azimuthale Geschwindigkeitsprofil der Saturnmagnetosphäre, DPG Frühjahrstagung, Freiburg, Germany, March 3-6, 2008. (Oral).
- **A. L. Müller**, J. Saur, N. Krupp, D. G. Mitchell, S. M. Krimigis, B. H. Mauk, and C. Paranicas, Azimuthal plasma flow determined from Injection Events, Cassini MAPS workshop, Max-Planck-Institute for Solar System Research, Katlenburg-Lindau, Germany, April 2-4, 2008. (Oral).

- **A. L. Müller**, J. Saur, N. Krupp, D. G. Mitchell, S. M. Krimigis, and B. H. Mauk, Injections at Saturn, Europlanet Workshop on Jupiter's and Saturn's aurora, Liège, Belgium, April 10-11, 2008. (Oral).

- **A. L. Müller**, J. Saur, N. Krupp, D. G. Mitchell, S. M. Krimigis, B. H. Mauk, C. Paranicas, and E. Roussos, Azimuthal plasma flow in the Kronian magnetosphere, Diplomanden- und Doktorandenseminar (Geophysik), University of Cologne, Institute for Geophysics and Meteorology, Cologne, Germany, May 29, 2008. (Oral).

- **A. L. Müller**, J. Saur, N. Krupp, D. G. Mitchell, S. M. Krimigis, B. H. Mauk, C. Paranicas, and E. Roussos, Azimuthal plasma flow in the Kronian magnetosphere - determined from injection events, MIMI-Team Meeting (Magnetospheric Imaging Instrument), Applied Physics Laboratory, Johns Hopkins University, Laurel, Maryland, USA, October 16-18, 2008. (Oral).

- **A. L. Müller**, N. Krupp, J. Saur, D. G. Mitchell, S. M. Krimigis, B. H. Mauk, C. Paranicas, and E. Roussos, Energetic particle injections in the Kronian magnetosphere, Solar System Seminar, Max Planck Institute for Solar System Research, Katlenburg-Lindau, Germany, November 12, 2008. (Oral).

- **A. L. Müller**, N. Krupp, J. Saur, D. G. Mitchell, S. M. Krimigis, B. H. Mauk, C. Paranicas, and E. Roussos, Energetic particle injections in the Kronian magnetosphere, Oberseminar Extraterrestrische Physik, University of Cologne, Institute for Geophysics and Meteorology, Cologne, Germany, November 28. (Oral).

- **A. L. Müller**, J. Saur, N. Krupp, D. G. Mitchell, S. M. Krimigis, B. H. Mauk, C. Paranicas, and E. Roussos, Particle injection events in the Kronian magnetosphere, Royal Astronomical Society Specialist Discussion Meeting, Outer planet magnetospheres: influences, interactions, and dynamics, Geological Society Lecture Theatre, Burlington House, London, UK, January 9, 2009. (Oral).

- **A. L. Müller**, J. Saur, N. Krupp, D. G. Mitchell, S. M. Krimigis, B. H. Mauk, C. Paranicas, and E. Roussos, Azimuthal plasma flow in the Kronian magnetosphere, Cassini Project Science Group Meeting, University College London, London, UK, June 22-26, 2009. (Oral).

- **A. L. Müller**, J. Saur, N. Krupp, D. G. Mitchell, S. M. Krimigis, B. H. Mauk, C. Paranicas, and E. Roussos, Dynamics of the Kronian magnetosphere, Diplomanden- und Doktorandenseminar (Geophysik), University of Cologne, Institute for Geophysics and Meteorology, Cologne, Germany, July 9, 2009. (Oral).

- **A. L. Müller**, J. Saur, N. Krupp, D. G. Mitchell, S. M. Krimigis, and E. Roussos, Azimuthal plasma flow in the Kronian magnetosphere, Magnetospheres of the Outer Planets Conference, University of Cologne, Cologne, Germany, July 27-31, 2009. (Oral).

- **A. L. Müller**, J. Saur, N. Krupp, Injection Events bei Saturn, Oberseminar Extraterrestrische Physik, University of Cologne, Institute for Geophysics and Meteorology, Cologne, Germany, November 24, 2009. (Oral).

- **A. L. Müller**, N. Krupp, J. Saur, Energetic particle injections in the Kronian magnetosphere, Max Planck Institute for Solar System Research, Katlenburg-Lindau, Germany, December 9, 2009. (Oral).

- **A. L. Müller**, J. Saur, N. Krupp, E. Roussos, B. H. Mauk, A. B. Rymer, D. G. Mitchell, and S. M. Krimigis, Azimuthal plasma flow in the Kronian magnetosphere, American Geophysical Union, Fall Meeting, San Francisco, CA, USA, December 14-18, 2009. (Poster).

- **A. L. Müller**, J. Saur, N. Krupp, and S. M. Krimigis, Energetic particle injection events in the Kronian magnetosphere, DPG Frühjahrstagung, University of Bonn, Bonn, Germany, March 15-19, 2010. (Oral).

- **A. L. Müller**, J. Saur, N. Krupp, Eigenschaften der Teilcheninjektionen in der Saturnmagnetosphäre, Diplomanden- und Doktorandenseminar (Geophysik), University of Cologne, Institute for Geophysics and Meteorology, Cologne, Germany, June 6, 2010. (Oral).

Danksagung

An dieser Stelle möchte ich all jenen danken, die mich durch fachlichen sowie persönlichen Beistand bei der Erstellung dieser Arbeit unterstützt haben.

Mein erster Dank gilt meinem Doktorvater, Herrn Prof. Dr. Saur. Ich danke ihm für seine exzellente Betreuung, in fachlicher sowie auch menschlicher Hinsicht. Er fand immer die notwendige Zeit für notwendige Diskussionen und Hilfestellungen und seine Begeisterung für die Physik konnte durchaus ansteckend sein.
Des weiteren möchte ich Herrn Dr. Norbert Krupp danken. Erst die Finanzierung durch das Max-Planck-Institut für Sonnensystemforschung machte diese Arbeit erst möglich. Für wissenschaftliche Diskussionen sowie die Möglichkeit, Ergebnisse meiner Arbeit auf Konferenzen und Treffen vor allem auch im Ausland vorzustellen, bin ich sehr dankbar. Es waren unter anderem diese Ereignisse, die oft einen Motivationsschub brachten.
An dieser Stelle sei im Besonderen erwähnt, dass ich beiden sehr dankbar bin, ein Teil ihrer jeweiligen Arbeitsgruppen sein zu können. Es ist mehr als inspirierend, wenn man die Gelegenheit hat, mit Mitarbeitern zweier solch hervorragender Arbeitsgruppen zusammenzuarbeiten. Entscheidend war dabei nicht immer nur die sachliche, sondern sehr oft auch die soziale und menschliche Komponente. An dieser Stelle sei allen Mitgliedern der Arbeitsgruppen gedankt.
Herrn Prof. Dr. B. Tezkan danke ich für die Übernahme des Zweitgutachtens.
Peter Kollman danke ich für ausgiebige fachliche Gespräche, Korrekturlesen und moralische Unterstützung, besonders im Hinblick auf die letzten Tage und Stunden dieser Arbeit.
Elias Roussos bin ich ebenfalls dankbar für fachliche Diskussionen, wertvolle Kommentare und Korrekturlesen.
Sven Simon stand jederzeit mit Rat und Tat zur Seite, egal ob es sich um physikalische oder zwischenmenschliche Angelegenheiten handelte.
Ich danke der Systemgruppe, im Speziellen Lex Wennmacher, Sven Jacobsen, Mario Seufert und Andreas Busse, die für jegliche Fragen stets ansprechbar und hilfsbereit gewesen sind.
Ich danke allen aktuellen und ehemaligen Bürokollegen für ein angenehmes Arbeitsklima, im Besonderen Emmanuel Chané, Timo Grambusch, Lorenz Roth und Rudi Eröss.
Sudha danke ich für Korrekturlesen.
Natürlich haben auch Freunde sowie meine Eltern durch moralische Unterstützung zum Gelingen dieser Arbeit beigetragen. Auch ihnen sei an dieser Stelle gedankt.
Tiefster Dank gebührt Tim, der mir besonders während der letzten Monate durch seine Liebe stets die notwendige Kraft gegeben hat.